

**LIGHT-INDUCED
ULTRAFAST TUNNELING DYNAMICS OF
A MANY-ELECTRON SYSTEM:
FROM WEAK TO STRONG FIELDS**

YI-JEN CHEN



Hamburg 2018

**LIGHT-INDUCED
ULTRAFAST TUNNELING DYNAMICS OF
A MANY-ELECTRON SYSTEM:
FROM WEAK TO STRONG FIELDS**

Dissertation
zur Erlangung des Doktorgrades (Doctor rerum naturalium)
an der Fakultät für Mathematik, Informatik und Naturwissenschaften
Fachbereich Physik
der Universität Hamburg

vorgelegt von
YI-JEN CHEN
geboren am 01.03.1987 in Taipeh

Hamburg 2018

Eidesstattliche Versicherung

Hiermit erkläre ich an Eides statt, dass ich die vorliegende Dissertationsschrift selbst verfasst und keine anderen als die angegebenen Quellen und Hilfsmittel benutzt habe.

Declaration on oath

I hereby declare, on oath, that I have written the present dissertation by my own and have not used other than the acknowledged resources and aids.

Hamburg, den 13.08.2018



Yi-Jen Chen

Gutachter der Dissertation:

Prof. Dr. Robin Santra

Dr. Michael Meyer

Dr. Alexei Grum-Grzhimailo

Gutachter der Disputation:

Prof. Dr. Robin Santra

Dr. Michael Meyer

Prof. Dr. Nina Rohringer

Prof. Dr. Jochen Küpper

Datum der Disputation:

01.02.2019

Vorsitzender des Prüfungsausschusses:

Prof. Dr. Daniela Pfannkuche

Vorsitzender des Fach-Promotionsausschusses Physik:

Prof. Dr. Michael Potthoff

Leiter des Fachbereichs Physik:

Prof. Dr. Wolfgang Hansen

Dekan der Fakultät für Mathematik, Informatik und Naturwissenschaften:

Prof. Dr. Heinrich Graener

To the serendipity along the way

Acknowledgments

Alas, the journey of my PhD has taken me from über 20 to über 30. It has finally come to a closure. Now looking back, everything would have been impossible without the people I have encountered along the way.

First of all, I would like to thank my supervisor Prof. Robin Santra. I have got inspired and learned so much from his infectious enthusiasm and broad knowledge in physics and beyond. I will always remember the aha moments and the excitement of “Hmmm... Let’s try this and that out” during our discussions. His advice on professional and personal matters has guided me through my PhD. Thank you very much for your patience, putting up with all of my idiosyncrasies.

I would also like to express my gratitude to the members of my PhD examination committee, Dr. Michael Meyer, Dr. Alexei Grum-Grzhimailo, Prof. Nina Rohringer, Prof. Jochen Küpper, and Prof. Daniela Pfannkuche. Thank you all for your kindness of reviewing my thesis and asking questions during my defense. All these feedbacks have allowed me to examine what I learned during my PhD from a fresh perspective.

Furthermore, I have benefited a lot from all the people that I have worked with. Thank you for pushing projects forward together with me and making me advance in my understanding of physics. Special thanks go to Stefan Pabst, whose mentoring, physical intuition and cheerful personality have helped me to navigate in the first years of my PhD; Zheng Li and Oriol Vendrell for teaching me how to simulate molecular dynamics and understand the physics therein; Mazyar Sabbar and Henry Timmers, who gave me the opportunity to explore their experimental data and amazed me with attosecond dynamics in real life; Antonia Karamatskou, whose collaboration with XFEL scientists inspired my works on the collective resonances.

My group members at the CFEL-Theory Division have created a wonderful working atmosphere for my PhD. Thank you all for these lovely moments of lunch talks over serious physics and superhero/Star Wars, enjoying cakes at the h-bar, and many things more. In particular, I would like to thank Sang-Kil Son for getting me to know the group and his always honest advice, my officemates Ludger Inhester and Koudai Toyota for so many nice conversations in and outside office, Malik Abdullah for taking care of me like his family in the WG, Otfried Geffert for his timely technical support and many hugs when I was down, Zoltan Zurek for listening to me (complaining) all the time late in the office, and, of course, Berit Heiser for her constant assistance and gentle smile. At this point, I would also like to thank Anna Kazakova and Steffi Killough from the DESY International Office and the IMPRS coordinator Julia Quante for their kind and continuous support.

And, thank you all my friends, for interrupting my nerdification process and getting me to enjoy other aspects of life, listening to and encouraging me, and lending me a helping hand—be it in times

when life was sweet or far away from the rosy glow. I especially appreciate the friendship with Thomas Tilp (prost!), Ivanka Grguraš (still feel touched by the PhD T-shirt and many more), Hauke Höppner and Francesca Moglia (thanks for always checking on me and offering me big hugs), Hsiang-Yu Chung (can I ask you for help in Hamburg again?), Denis Anielski (that was the craziest party I have ever been to), and Jonathan Correa (it's easier to talk after a few drinks).

Finally, I would like to thank my family; they always support my decisions and provide a haven I can turn to whenever in need. My deepest gratitude goes to my boyfriend Yannis Laplace (and the whole Laplace family), who urged me to finish the thesis and proofread it, and, at all times, shows me how to «Mordant au citron d'or de l'idéal amer».

“In the depth of winter, I finally learned that within me there lay an invincible summer. — A. Camus”.
This thesis is for you all.

Abstract

Photoionization is one of the most possible processes that can happen when light interacts with an electronic system. This seemingly simple phenomenon has expanded into a rich playground thanks to the rapid development of ultraintense and ultrashort light-source technology.

In this doctoral dissertation, we investigate photoionization dynamics that can be measured or triggered by advanced light sources. We focus on the theoretical understanding of (1) photoionization processes assisted by ultrafast electron tunneling, i.e., short-lived shape-type resonance processes, and (2) properties that emerge as the size of the electronic system increases, with the heavy atom xenon serving as a benchmark system. To this end, many-electron Schrödinger equation is solved from first principles using a combination of wave-packet propagation and non-Hermitian resonance-state techniques. Two applications are presented in two distinct regimes of light-matter coupling.

In the first application, we study the resonance dynamics of xenon induced by extreme ultraviolet (XUV) light in the perturbative regime of light-matter coupling. Here, the linear response of xenon is known to exhibit a plasma-like, collective feature, the giant dipole resonance (GDR). We find that the GDR is composed of two short-lived resonance states. Albeit hidden in XUV linear spectroscopy, this resonance substructure has been resolved lately using XUV nonlinear spectroscopy. In addition, by analyzing all types of resonance states and then their spectroscopic fingerprints, we explain the limitation of linear-response studies and reveal the existence of collective multipole resonances. Our work offers a new way to understand collective electronic behavior in and beyond the linear regime.

In the second application, we study the resonance dynamics of xenon induced by near infrared (NIR) light in the nonperturbative regime of light-matter coupling. Here, strong-field ionization (SFI), a process of both fundamental and technological importance, is examined inside each laser subcycle. In our experiment-theory collaboration, the SFI dynamics is followed by attosecond transient absorption spectroscopy and is found to show an unexpected oscillatory character. With the aid of theory, we identify polarization as the origin of this oscillation. While the role of polarization had so far been unnoticed in the strong-field regime, it comes into light due to the high polarizability of xenon and is expected to influence the strongly driven dynamics of extended electronic systems.

Zusammenfassung

Photoionisation ist einer der häufigsten Prozesse die durch Licht-Elektronen-Wechselwirkung verursacht wird. Dieses scheinbar einfache Phänomen hat im Zuge der Entwicklung ultraintensiver und ultrakurzer Licht-Technologien besondere Aufmerksamkeit gewonnen.

In dieser Arbeit wird die Photoionisierungsdynamik untersucht, die durch neuartige Lichtquellen gemessen oder erzeugt werden kann. Im Fokus steht, erstens, das theoretische Verständnis von Photoionisierungsprozessen, die ultraschnelle quantenmechanischer Tunneleffekte oder kurzlebige, Shape-Resonanz-ähnlichen Resonanzen involvieren. Zweitens, das theoretische Verständnis von Eigenschaften die mit Anwachsen der Größe der Elektronenstruktur hervortreten, aufgezeigt am Beispiel des Xenon Atoms. Basierend auf fundamentalen quantenmechanischen Grundlagen wird die Vielteilchen-Schrödinger-Gleichung gelöst und dabei eine Kombination von Wellenpaket-Propagation und nicht-hermitesche Resonanzzustand-Techniken verwendet. Zwei Anwendungen werden in dieser Arbeit beschrieben, die separate Parameterbereiche der Licht-Materie Wechselwirkung adressieren.

Im ersten Teil wird die resonante Dynamik von Xenon induziert durch Licht aus dem hohen ultravioletten Wellenlängen-Bereich (XUV) im störungstheoretischem Parameterbereich der Licht-Materie Kopplung untersucht. Es ist bekannt, dass die lineare Antwort des Xenon Atoms ein Plasma-ähnliches, kollektives Merkmal aufweist, das bekannt ist als Riesen-Dipol-Resonanz (GDR). In dieser Arbeit wird gezeigt, dass die GDR aus zwei kurzlebigen Resonanzzuständen besteht. Für lineare XUV-Spektroskopie ist diese Resonanz Substruktur verdeckt, sie ist aber kürzlich mit nicht-lineare XUV-Spektroskopie gemessen worden. Durch Analysieren der spektroskopischen Fingerabdrücke einzelner Resonanzen zeigen wir darüber hinaus die Grenzen von Lineare-Antwort-Untersuchungen auf und beschreiben die Existenz kollektiver Multipol-Resonanzen. Diese Arbeit bietet ein neuartiges Verständnis des kollektiven Elektronen-Verhaltens im linearen wie im nicht-linearen Parameterbereich.

Im zweiten Teil wird die resonante Dynamik bei Photoionisation eines Xenon Atoms durch Nah-Infrarot-Licht (NIR) im nicht-störungstheoretischem Bereich der Licht-Materie Kopplung untersucht. Die Ionisation durch starke Felder (SFI), ein Phänomen, das sowohl Bedeutung für grundlegende Physik also auch für technologische Anwendungen hat, wird hier innerhalb der einzelnen Laserzyklen untersucht. Unterstützt durch die Kooperation mit einer experimentellen Arbeitsgruppe wird in dieser Arbeit die SFI-Dynamik mittels transientser Absorptionsspektroskopie untersucht und dabei ein unerwartetes oszillatorisches Verhalten beobachtet. Theoretische Berechnungen identifizieren Polarisierung als Ursache dieser Oszillationen. Im Zusammenhang mit starken Laserfeldern sind diese Polarisierungseffekte bisher unbemerkt geblieben; durch die hohe Polarisierbarkeit des Xenon Atoms kommen sie zum Vorschein und sollten auch für das Verhalten von größeren elektronischen Systemen von Bedeutung sein.

List of publications

My doctoral research has resulted in the following publications. The topics encompass light-induced electronic [1, 3-5] and rotational [2] dynamics. The content of this dissertation is largely based on Refs. [3-5].

Journal articles

1. A. Karamatskou, S. Pabst, Y.-J. Chen, and R. Santra
Calculation of photoelectron spectra within the time-dependent configuration-interaction singles scheme
Physical Review A **89**, 033415 (2014) → [DOI](#)
Erratum
Physical Review A **91**, 069907(E) (2015) → [DOI](#)
2. Y.-J. Chen, S. Pabst, Z. Li, O. Vendrell, and R. Santra
Dynamics of fluctuations in a quantum system
Physical Review A **89**, 052113 (2014) → [DOI](#)
3. Y.-J. Chen, S. Pabst, A. Karamatskou, and R. Santra
Theoretical characterization of the collective resonance states underlying the xenon giant dipole resonance
Physical Review A **91**, 032503 (2015) → [DOI](#)
4. M. Sabbar*, H. Timmers*, Y.-J. Chen*, A. K. Pymer, Z.-H. Loh, S. G. Sayres, S. Pabst, R. Santra, and S. R. Leone (*These authors contributed equally to this work)
State-resolved attosecond reversible and irreversible dynamics in strong optical fields
Nature Physics **13**, 472 (2017) → [DOI](#)
• Selected science highlight in *DESY Photon Science Annual Report 2017* → [URL](#)
5. Y.-J. Chen, S. Pabst, and R. Santra
Collective resonances of atomic xenon from the linear to the nonlinear regime
Journal of Physics Communications **2**, 045024 (2018) → [DOI](#)

Conference papers

- i. Y.-J. Chen, S. Pabst, A. Karamatskou, and R. Santra
Theoretical characterization of the collective resonance states underlying the xenon giant dipole resonance
Journal of Physics: Conference Series **635**, 092046 (2015) → [DOI](#)

- ii. H. Timmers, M. Sabbar, [Y.-J. Chen](#), R. Santra, D. M. Neumark, and S. R. Leone
Probing ionization dynamics with attosecond transient absorption spectroscopy
OSA Technical Digest, UTh4A.39 (2016) → [DOI](#)

List of presentations

I have given the following presentations on my doctoral work.

Invited talks

1. **Ultrafast tunneling states of a many-electron atom: from weak to strong fields**
International Workshop on Atomic Physics
Dresden, Germany, Dec. 2016 → [URL](#)
2. **Ultrafast tunneling states of a many-electron system: from weak to strong fields**
Photon Science Meeting, German Electron Synchrotron (DESY)
Hamburg, Germany, Mar. 2017 → [URL](#)
3. **Ultrafast dynamics of atoms and molecules in strong light fields**
Seminar of Laboratory of Computational Science and Modeling, Swiss Federal Institute of Technology in Lausanne (EPFL)
Lausanne, Switzerland, Jun. 2017 → [URL](#)
4. **Light-induced ultrafast tunneling dynamics of a many-electron system: from weak to strong fields**
Quantum Dynamics Seminar, Max Planck Institute for the Physics of Complex Systems (MPIPKS)
Dresden, Germany, Aug. 2017 → [URL](#)
5. **Attosecond reversible and irreversible electron dynamics in strong optical fields**
QUTIF Annual Meeting, German Research Foundation (DFG)
Hamburg, Germany, Feb. 2018 → [URL](#)

Contributed talks

- i. **Fluctuations in laser-aligned molecules**
SAMOP Spring Meeting, German Physical Society (DPG)
Hannover, Germany, Mar. 2013 → [URL](#)
- ii. **Fluctuations in laser-induced molecular alignment**
Joint Workshop on Quantum Dynamics and Photon-Matter-Interaction, International Max Planck Research School (IMPRS)
Dresden, Germany, May 2013 → [URL](#)

- iii. **Non-equilibrium dynamics manifested by fluctuations in a quantum many-body system: giant dipole resonance of atomic xenon**
SAMOP Spring Meeting, German Physical Society (DPG)
Berlin, Germany, Mar. 2014 → [URL](#)
- iv. **Theoretical characterization of the collective resonance states underlying the xenon giant dipole resonance**
SAMOP Spring Meeting, German Physical Society (DPG)
Heidelberg, Germany, Mar. 2015 → [URL](#)
- v. **Collective resonances of atomic xenon from the linear to the nonlinear regime**
DAMOP Annual Meeting, American Physical Society (APS)
Providence, U.S.A., May 2016 → [URL](#)

Poster presentations

- a. **Dynamics of quantum fluctuations in laser-aligned molecules**
Symposium of Center for Free-Electron Laser Science, German Electron Synchrotron (DESY)
Timmendorfer Strand, Germany, Oct. 2013 → [URL](#)
- b. **Time-resolved collective electron dynamics in xenon**
Gordon Research Conference on Multiphoton Processes
Waltham, U.S.A., Jun. 2014 → [URL](#)
- c. **Theoretical characterization of the collective resonance states underlying the xenon giant dipole resonance**
International Conference on Photonic, Electronic and Atomic Collisions
Toledo, Spain, Jul. 2015 → [URL](#)

Contents

Acknowledgments	v
Abstract & Zusammenfassung	vii
List of publications & List of presentations	ix
Glossary of abbreviations	xvi
Units and constants	xvii
1 Introduction	1
1.1 New perspectives on photoionization dynamics	2
1.2 Pictures of photoionization in two light-matter–interaction regimes	5
1.3 Dichotomy between perturbative and nonperturbative photoionization theories	7
1.4 Attosecond tunneling dynamics in perturbative to nonperturbative photoionization of Xe	11
1.4.1 Collective resonance behavior of Xe	14
1.4.2 Subcycle strong-field–ionization dynamics of Xe	15
1.4.3 Outline of the thesis	17
2 Theory of light-matter interaction	19
2.1 Theoretical description of light-matter interaction	20
2.1.1 The N-electron Schrödinger equation	20
2.1.2 Different frames of light-matter interaction	24
2.2 Ab initio solution of light-matter interaction	26
2.2.1 Concept of configuration interaction	26
2.2.2 Theory of time-dependent configuration-interaction singles	29
2.2.3 Multichannel physics and electronic correlation effects	31
2.3 Implementation aspects	35
2.4 Summary	36
3 Theory of resonances	39
3.1 Theoretical description of resonances	40

3.1.1	Wave-packet view of resonances	40
3.1.2	Eigenstate view of resonances	44
3.2	Direct calculation of resonance states	49
3.2.1	Method of complex scaling	50
3.2.2	Method of complex absorbing potentials	54
3.2.3	Fundamentals of nonhermitian quantum mechanics	56
3.3	Implementation aspects	59
3.4	Summary	61
4	Application I: Collective resonance behavior of Xe	63
4.1	Introduction	64
4.2	Exposing the hidden substructure of the giant dipole resonance	66
4.2.1	Time-dependent approach to overlapping resonances	69
4.2.2	GDR substructure revealed: time-dependent method	71
4.2.3	GDR substructure revealed: time-independent method	78
4.2.4	Consequence of the approximation to the zeros of a dielectric function	81
4.2.5	Evidence from a recent experiment at FLASH	84
4.3	Collective resonances in and beyond the linear-response regime	87
4.3.1	Characterization of the resonance states	89
4.3.2	Many-body effects on the emergence of the correlated electronic structure	90
4.3.3	Properties of the double-pole structure in the noninteracting limit	93
4.3.4	State-by-state analysis of the one-photon absorption spectrum	96
4.3.5	Three-photon–two-color scheme for probing the collective octupole resonance	100
4.4	Summary	102
5	Application II: Subcycle strong-field–ionization dynamics of Xe	105
5.1	Introduction	106
5.2	Taking attosecond snapshots of strong-field ionization	109
5.2.1	Concept of the experiment and the theoretical modeling	111
5.2.2	ATAS spectrograms	114
5.2.3	Reconstruction of the effective SFI dynamics	117
5.2.4	Comparison between the effective and the instantaneous SFI dynamics	121
5.3	Reversible and irreversible electron dynamics in strong optical fields	124
5.3.1	Electronic correlation and long-range Coulomb effects on the SFI dynamics	126
5.3.2	Decomposition of the SFI dynamics	129

5.3.3	Visualization of wave-packet motion in the weak- and strong-field limits . .	133
5.4	Summary	137
6	Conclusion and outlook	139
6.1	Conclusion	139
6.2	Outlook	143
	Bibliography	147

Glossary of abbreviations

ADK	Ammosov-Delone-Krainov
ARPACK	the Arnoldi Package
ATAS	attosecond transient absorption spectroscopy
ATI	above-threshold ionization
CAP	complex absorbing potential
CIS	configuration-interaction singles
CS	complex scaling
ECS	exterior complex scaling
FEL	free-electron laser
FERMI	the Free-Electron Laser for Multidisciplinary Investigations
FLASH	the Free-Electron Laser in Hamburg
GDR	giant dipole resonance
HF	Hartree-Fock
HFS	Hartree-Fock-Slater
HHG	high-harmonic generation
IDM	ion density matrix
MF	mean-field
MIR	mid infrared
MPI	multiphoton ionization
NHQM	non-Hermitian quantum mechanics
NIR	near infrared
OD	optical density
OTBI	over-the-barrier ionization
RPAE	random-phase approximation with exchange
SAE	single active electron
SCF	self-consistent field
SES	smooth exterior complex scaling
SFA	strong-field approximation
SFI	strong-field ionization
TDCIS	time-dependent configuration-interaction singles
TDDFT	time-dependent density functional theory
VUV	vacuum ultraviolet
XCID	the Configuration-Interaction Dynamics Package
XUV	extreme ultraviolet

Units and constants

Atomic units (a.u.) are a system of natural units that is particularly convenient for describing the physics in electrons' world. They will be used throughout this dissertation unless otherwise stated.

Fundamental constants			
Name	Symbol	Value in a.u.	Approx. value in SI units
elementary charge	e	1	1.60×10^{-19} C
electron rest mass	m_e	1	9.11×10^{-31} kg
reduced Planck constant	\hbar	1	1.05×10^{-34} J · s
Coulomb's constant	$1/(4\pi\epsilon_0)$	1	8.99×10^9 kg · m ³ · s ⁻² · C ⁻²
fine-structure constant	α	$\approx 7.30 \times 10^{-3}$	7.30×10^{-3}
speed of light in vacuum	c	$1/\alpha \approx 137$	3.00×10^8 m · s ⁻¹

Derived atomic units			
Quantity	Name	Definition	Approx. value in SI units
length	bohr	$a_0 = 4\pi\epsilon_0\hbar^2/(m_e e^2)$	5.30×10^{-11} m
energy	hartree	$E_h = m_e e^4/(4\pi\epsilon_0\hbar)^2$	4.36×10^{-18} J \approx 27.2 eV
time		\hbar/E_h	2.42×10^{-17} s
electric field strength		$E_{\text{a.u.}} = E_h/(ea_0)$	5.14×10^{11} V · m ⁻¹
electric field intensity		$\epsilon_0 c E_{\text{a.u.}}^2/2$	3.51×10^{20} W · m ⁻²

Chapter 1

Introduction

Electrons have played a central part in our science and technology since its discovery at the turn of the 20th century. They decide the structure of atoms and molecules, the formation and the breaking of chemical bonds, the function of biomolecules, and the character of materials. Indeed, in the microscopic world of electrons, the apparently so disparate fields of physics, chemistry, biology, and engineering seem to converge and become closely tied to one another.

Much of what we know about this microcosm comes from observing how it interacts with electromagnetic radiation. Light-source technology has achieved immense progress over the past decades. In particular, free-electron lasers (FELs), femtosecond lasers, and high-harmonic generation (HHG) sources produce coherent radiation with an ever increasing intensity and an ever shortening duration. These new capabilities enable us to interrogate matter in ways that are previously impossible, thus initiating new lines of research.

This doctoral dissertation presents a theoretical investigation on electron dynamics that can be measured or triggered by these advanced light sources. In the weak- to strong-field regime of light-matter coupling, photoionization dynamics are studied. Special attention is paid to ionization processes accompanied by ultrafast electron tunneling, namely transient shape-type resonance processes. Xenon, a heavy atom with 54 electrons, is chosen as a benchmark system in order to exploit and explore features absent in few-electron systems.

Ready for the journey? This chapter proceeds as follows. Section 1.1 gives an overview of the modern light sources and the new research directions opened in the context of photoionization. Section 1.2 introduces the pictures of photoionization in different regimes of light-matter interaction. Section 1.3 explains a dichotomy among photoionization theories, which can be bridged by the many-body theory used in this thesis. Section 1.4 presents the major topic, the contributions, and the outline of this thesis.

1.1 New perspectives on photoionization dynamics

Photoionization is one of the most probable processes that can happen when light strikes an electronic system. The classic photoelectric effect [1] involves the absorption of one photon and explores the linear response of matter. Since the early days of quantum mechanics, this effect has provided a vital tool for understanding the nature of electronic [2, 3] and atomic [4] structure. Today, the research on photoionization continues to expand thanks to the bettered experimental instruments at hand.

The light pulses generated by large-scale FEL facilities as well as table-top femtosecond lasers and HHG sources offer a complementary set of new tools to investigate electrons. On the one hand, the photon energy of FEL and HHG pulses covers the hard-x-ray to the extreme-ultraviolet (XUV) region ($10^4 - 10^1$ eV), which grants access down to core electrons [5]. On the other hand, the wavelength of femtosecond lasers spans from the visible to the midinfrared (MIR) end ($10^0 - 10^{-2}$ eV), which mostly interacts with valence electrons [6]. Apart from the frequency, the peak intensity and the pulse duration offered by these sources are also quite different. The uniqueness of each of these two properties has led to the appearance of a new research area that transforms the study on photoionization, which is briefly reviewed below.

Ultra-high intensity: birth of strong-field physics. While HHG sources are relatively weak and mainly cause one-photon transitions, FELs and femtosecond lasers deliver pulsed radiation at an extreme brilliance, up to 10^{34} photons/s/mrad²/mm²/0.1% bandwidth [7]. A comparison of the peak brilliance, which is an indicator of the peak intensity, is shown in Fig. 1.1. Such an ultra-high intensity opens the door to a true variety of photoionization pathways, giving birth to *strong-field physics* [8, 9]. For instance, a system can be multiply ionized through a sequence of one-photon ionization steps [10], can simultaneously absorb several photons to overcome an ionization threshold (multiphoton ionization, MPI), or can absorb more photons from there and go further up into the continuum (above-threshold ionization, ATI) [8]. If the field strength keeps on increasing such that the effect of the light field becomes comparable or greater than that of the binding potential, a photoelectron can be liberated by tunneling through (strong-field ionization, SFI) or by directly escaping from (over-the-barrier ionization, OTBI) a modified potential [8].

As an impressive example, a recent experiment at an x-ray FEL (XFEL) facility has reported Xe atoms being charged up to Xe^{36+} by a single light pulse [11]. This is the result

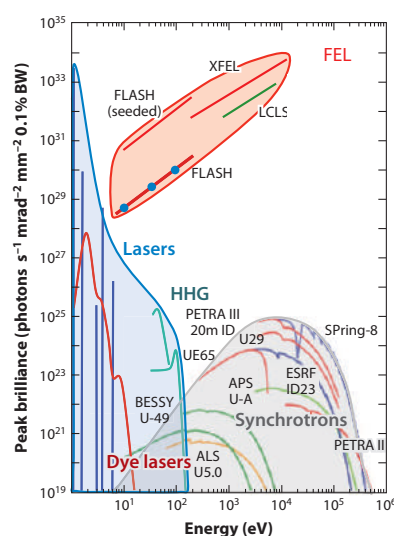


Figure 1.1. Comparison of the peak brilliance of various modern light sources. Peak brilliance is measured in photons/s/mrad²/mm²/0.1% bandwidth and is plotted as a function of photon energy. The sources discussed in this thesis include: FELs (labeled by “FEL”), HHG sources (labeled by “HHG”), and femtosecond lasers (sitting at the low-energy end of the label “Lasers”). The figure is adapted from Ref. [7]. Copyright ©2012 Annual Reviews.

of an intricate interplay of sequential one-photon ionization steps, resonant excitations, and relaxation cascades [12]. A key application of SFI brought by femtosecond lasers is HHG: a highly nonlinear light emission process that yields a wide radiation spectrum at multiples of the fundamental driver frequency [6]. Lately, it has been demonstrated that an MIR laser with a central photon energy below 1 eV is able to create an HHG spectrum extending into the water window in the keV range [13].

Ultrashort duration: birth of attosecond physics. The pulse duration of FELs and femtosecond lasers can be as short as a few femtoseconds ($1 \text{ fs} = 10^{-15} \text{ s}$) [5, 6]. HHG pulses, which are produced by synthesizing a broadband HHG spectrum, has an even shorter duration reaching down to a few tens of attoseconds ($1 \text{ as} = 10^{-18} \text{ s}$). As of today, the shortest burst of light ever recorded is HHG-based and lasts for only 43 as [14]. As illustrated in Fig. 1.2, electron motion in the microscopic world generally unfolds on a time scale between 10 as and 10 fs [5]. The ultrashort duration of HHG sources makes it feasible to resolve, monitor, or even steer electrons directly in the time domain, giving rise to *attosecond physics* [15, 16]. For real-time observation of electron dynamics, attosecond metrology typically employs a femtosecond nearinfrared (NIR) pulse synchronized with an attosecond XUV pulse

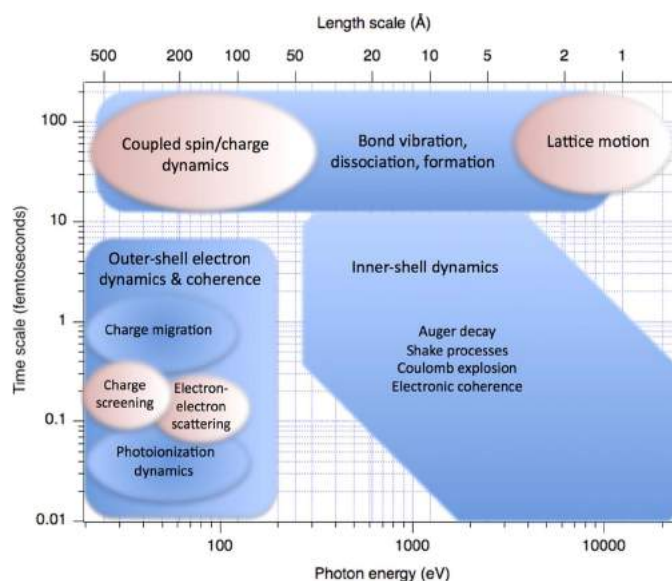


Figure 1.2. Comparison of the time scale of various ultrafast processes in the microscopic world. The upper horizontal axis represents the length scale associated with each process. The time scale of electronic motion has an upper bound of 10 fs, above which is the time scale of atomic motion in molecules and solids. The figure is adapted from Ref. [5]. Copyright ©2018 IOP Publishing.

(or pulse train).^a Either pulse can be used as a pump, which launches the dynamics, or a probe, which measures the sample after a certain time period. By adjusting the time delay between the two pulses, one obtains a series of snapshots, i.e., a movie, of the ultrafast process [15, 16].

Attosecond science adds a new dimension to the research on photoionization—the dimension of time. For instance, it has been applied to track charge migration in biologically relevant molecules [17], where the rapid removal of an electron results in positive charge traveling along the molecular skeleton within a few fs, preceding any nuclear rearrangement [18]. As another example, attosecond spectroscopy has answered the fundamental question as to how much time it takes for a photoelectron to appear in the continuum. A photoemission time delay below 100 as has been found for electrons freed from different electronic shells [19, 20] or spin orbitals [21] in atomic to solid-state systems.

^aUp to now, attosecond-pump–attosecond-probe experiment still remains as a fundamental challenge [16]. This is because the signal resulting from two weak, HHG-based pulses suffers from low statistics.

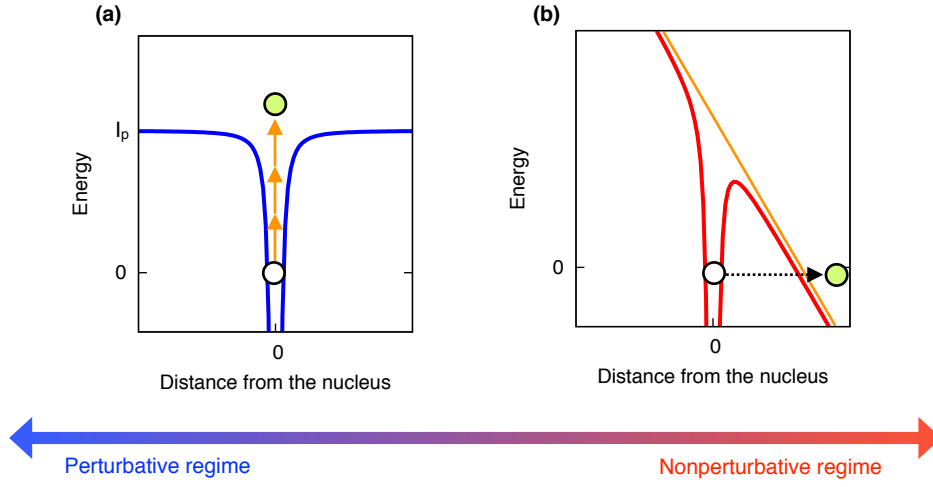


Figure 1.3. Schematic views of photoionization in two regimes of light-matter interaction. The energy of the electronic ground state is assumed zero; the ionization potential is indicated by I_p . **(a)** In the perturbative regime, the electron sees the field-free potential (blue curve); it is excited from the ground state to the continuum by absorbing n photons (yellow arrows). **(b)** In the nonperturbative regime, the electron sees a deformed potential (red curve) due to an extra potential imposed by the light field (yellow line); it can get ionized by tunneling through the barrier of the dressed potential.

1.2 Pictures of photoionization in two light-matter–interaction regimes

The nature of all the possible ionization pathways that can take place in the extended light-field parameter space is commonly classified by the *Keldysh parameter* [22, 23]

$$\gamma = \sqrt{\frac{I_p}{2U_p}}. \quad (1.1)$$

In above, I_p is the ionization potential of an accessible electron; $U_p = E_0^2/(4\omega_0^2)$ is the ponderomotive energy, the cycle-averaged kinetic energy of an electron freely quivering in a light field with an amplitude E_0 and a frequency ω_0 . In essence, the Keldysh parameter is a measure of the relevance of two energy scales: the intrinsic energy scale of the bound electron and the energy scale imparted by the external radiation. Depending on the value of γ , one distinguishes between two regimes of light-matter coupling as follows.

$\gamma \gg 1$: **weak-field or perturbative regime of light-matter coupling.** In the case of $\gamma \gg 1$, light-matter interaction can be viewed as a correction to the field-free system, and ionization

is governed by *perturbative photoionization*. The physical picture of this type of ionization is depicted in Fig. 1.3(a). Here, the electron in the field-free potential simultaneously absorbs a well-defined number of photons, say n photons, and is promoted from the electronic ground state to the continuum, as captured exactly by the corresponding n th-order perturbation theory. This is the mechanism behind one-photon ionization and few-photon MPI and ATI [8, 24]. Because of the scaling relation $\gamma \propto \omega_0/E_0$, ionization driven by former generations of light sources and HHG sources (due to the low intensity) as well as FELs (due to the high frequency) falls in this regime.

$\gamma \ll 1$: **strong-field or nonperturbative regime of light-matter coupling.** In the case of $\gamma \ll 1$, light-matter interaction can no longer be seen as a perturbation to the field-free system, and ionization is ruled by *nonperturbative photoionization*. The physical picture of this kind of ionization is portrayed in Fig. 1.3(b). Here, at a specific time, the instantaneous light field distorts the binding potential and creates a potential barrier with a finite width, which allows the bound electron to tunnel through and, hence, to become ionized. If the field magnitude further increases, the barrier gets thinner and lower until eventually the electron can flow over rather than tunnel through it. These two explanations underlie the origins of SFI and OTBI, respectively [8, 23]. Since $\gamma \propto \omega_0/E_0$, ionization induced by femtosecond lasers (due to the low frequency and the high intensity) belongs to this regime.

Two remarks are in place. First, owing to the breakdown of perturbation theory, the number of photons absorbed by the system becomes an ill-defined quantity when $\gamma \ll 1$. This inability to count photons is reflected by a nearly continuous distribution in the non-perturbative photoelectron energy spectrum, which is in sharp contrast to a set of discrete peaks spaced by ω_0 in the perturbative spectrum [25].^b Second, the notion of ionization out of the instantaneous deformed potential only makes sense provided the duration of the electron traversing the barrier is much shorter than the period of the oscillating field. The ratio between these two time scales is approximately given by the Keldysh parameter as well. Consequently, the condition of $\gamma \ll 1$ is also called the quasistatic limit of photoionization and automatically guarantees the validity of the tilted-potential picture [23].

At an intermediate value $\gamma \approx 1$, ionization occurs, in principle, as a mixture of the pertur-

^bWhen $\gamma \ll 1$, the photoelectron spectrum shows a smooth feature, whereas the light emission spectrum can have a discrete character. There is no contradiction between the two. In a monochromatic field, an ionized wave packet is released every laser half-cycle. Although each wave packet carries no characteristic energy, the HHG spectrum, which is the Fourier transform of a signal with temporal periodicity, consists of discrete peaks with a spacing of ω_0 [26].

bative and the nonperturbative processes. However, experiments performed under this condition have shown that nonperturbative photoionization tends to be the dominating mechanism [27].

1.3 Dichotomy between perturbative and nonperturbative photoionization theories

The two pictures presented in the last section are, of course, a simplified one: they reduce the complexity of a many-electron system to an independent-particle model, neglecting the effects of interelectron Coulomb coupling. In order to describe light-matter interaction, one must simultaneously treat light-electron interaction as well as electron-electron interaction.

For a general electronic system, a most rigorous description of photoionization is provided by the N -electron time-dependent Schrödinger equation (TDSE) [28, 29]. The solution of this equation is a formidable challenge. Even with the help of advanced computational tools, exact solution of the N -electron TDSE has so far been found for systems with no more than three electrons [30, 31].

In pace with the progress of light-source technology, continuous development has been made on the theory side so as to formulate the best approximate description of photoionization. However, theories available in the two ionization regimes appear to have their own merit, and thus shortcoming, in the treatment of the aforementioned two types of interaction.

Perturbative regime: accurate many-electron theories. In the perturbative regime of photoionization, there are photoionization theories that can take into account electronic correlation effects to great accuracy [29]. Notably, random-phase approximation with exchange (RPAE) and its extensions [33, 34] as well as many-body perturbation theory (MBPT) [35] have achieved remarkable success in reproducing experimental (generalized) photoabsorption cross sections, a measure of photoionization probability in the weak-field limit. These highly correlated methods typically rely on diagrammatic perturbative expansion of the N -electron TDSE (see, e.g., the left panel of Fig. 1.4). While electron-electron interaction can be included to very high order (or, in the case of RPAE, to an infinite order for a certain kind of electronic interaction), light-electron interaction cannot be calculated to high order due to the growing intricacy of summing over all the possible diagrams. This difficulty limits the practical applicability of such many-body techniques to rather-few-photon ionization

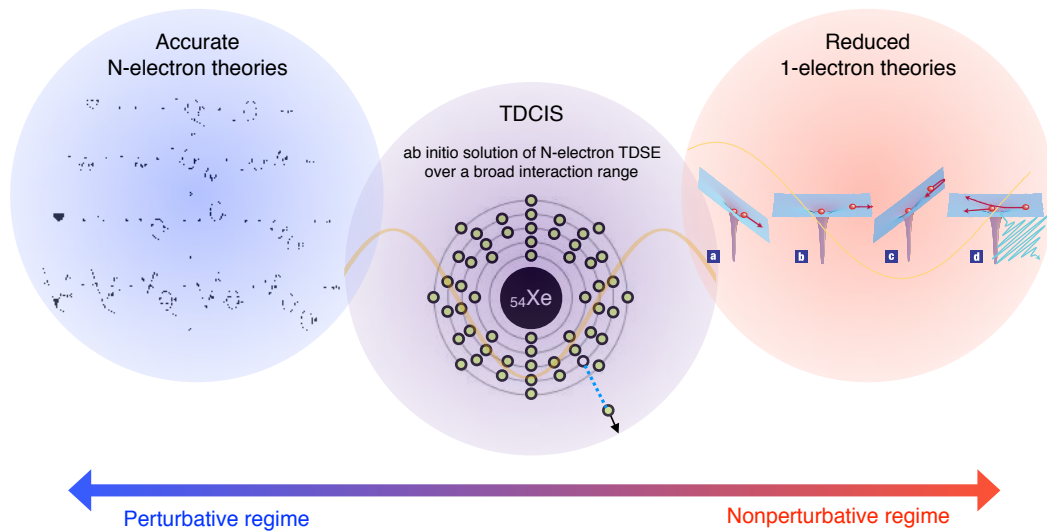


Figure 1.4. Illustration of the dichotomy of photoionization theories between two different regimes of light-matter interactions. The TDCIS theory may be used to fill in this gap. It not only provides *ab initio* solution to N -electron TDSE over a broad range of light-matter-coupling strength, but also includes multichannel physics and essential electronic correlation effects. Its relatively high computational efficiency makes it currently the only wave-function-based approach that is able to tackle the strong-field single ionization dynamics of a heavy Xe atom. Parts of the figure are reproduced from Refs. [26, 32]. Copyright ©1987 American Physical Society, 2007 Nature Publishing Group.

processes [32, 36].^c

Nonperturbative regime: reduced one-electron theories. As one enters the nonperturbative regime of photoionization, although light-matter interaction is treated up to an infinite order, electronic correlation effects are mostly discarded and standard theories are highly reduced one-body theories. The widely used single-active-electron (SAE) approximation allows only the outermost valence electron to be ionized [8, 38], which then moves in an effective, frozen ionic potential [39, 40]. Two main reasons lead to this simplification. First, direct numerical solution of TDSE is computationally demanding, due to a large number of highly excited and delocalized continuum states required to describe the photoionized wave packet. Second, based on physical intuition, the photoelectron is accelerated by the light field and is moving at a very high speed away from the ion. Hence, it seems that there is no

^cFor the treatment of XFEL-driven perturbative, multiple ionization, one has to employ an independent-particle model because of the sheer amount of electronic configurations involved in the production of highly charged ions [37].

time window that allows the photoelectron to stay nearby the photoion to trigger electronic correlation.

At this stage, there appears to be a dichotomy between perturbative and nonperturbative photoionization theories. On the one hand, perturbative theories treat the electronic correlation to very high order but have difficulty increasing the order of light-matter interaction included. On the other hand, nonperturbative theories describe light-matter interaction to very high order but discard electron correlation effects. Can one find a theory that allows solution of the N -electron TDSE without making any assumption on the strength of light-matter coupling and, at the same time, takes into account a moderate amount of multielectron effects? Development of such a theory is timely in order to assess many-electron aspects during nonperturbative photoionization. Furthermore, in light of the emergence of attosecond metrology, such a theory could offer one single theoretical framework for the description of attosecond pump-probe experiments, treating a pair of weak and strong pulses on equal footing.

TDCIS: simulating photoionization dynamics of an N -electron system over a broad interaction range. In this thesis, we take on the time-dependent configuration-interaction–singles (TDCIS) theory, a wave-function–based many-body theory that solves N -electron TDSE from first principles [41, 42]. TDCIS, first proposed by Rohringer and Santra in Ref. [43], has been developed in Refs. [44–48] and implemented in our XCID package [49]. This method has been successfully applied to a broad spectrum of perturbative [50–55] and nonperturbative [45, 56–60] ionization scenarios, with photon energies spanning from x-rays down to NIR. It contains essential many-electron effects during photoionization processes and lifts two restrictions of the SAE-type theories: TDCIS not only permits the photoelectron to emerge from various electronic shells with a multichannel character, but also captures the major correlation effects between the photoelectron and the photoion [41].

Lately, there is a surge of many-electron theories that borrows tools from ab initio quantum chemistry and adapts them for the time-dependent N -electron problem [30, 31]. Such methods can roughly be divided into two categories; each follows their own strategy to bypass the curse of dimensionality. The first category uses the N -electron wave function to describe the system but constrains the volume of the N -electron Hilbert space. This includes TDCIS, time-dependent multiconfigurational self-consistent-field (TD-MCSCF) and its variants [31, 61–63], TDHF [64], and time-dependent R-matrix (TDRM) theory [65–67].^d The sec-

^dIt is interesting to point out that such wave-function–based methods have recently been applied to the studies

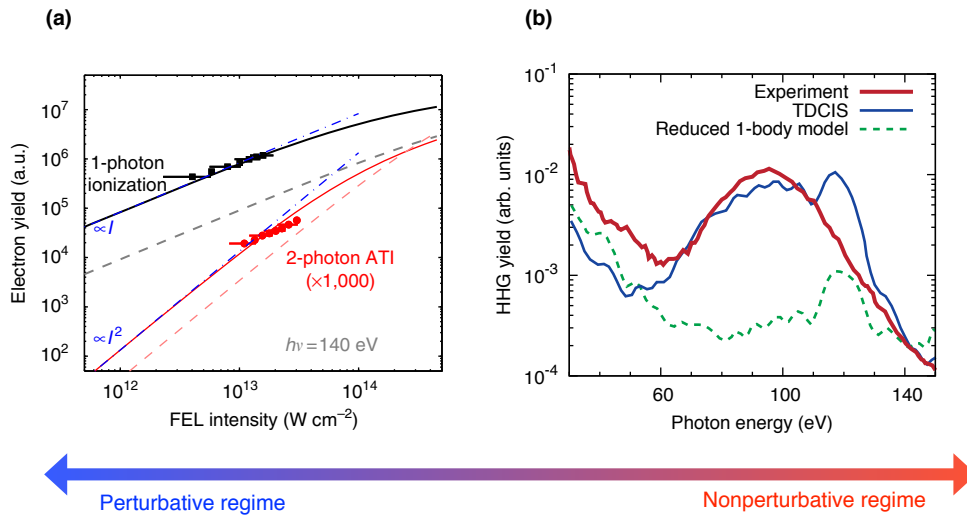


Figure 1.5. Two applications of TDCIS to the photoionization dynamics of Xe in two different regimes of light-matter interaction. **(a)** Two-photon ATI process in the perturbative regime. The photoelectron yields at an XUV photon energy of 140 eV are plotted as a function of the FEL intensity. The experimental data measured at FLASH (red filled circles) are compared with the calculations using TDCIS (red solid line) and those using a reduced one-electron model (red dashed line). The figure is adapted from Ref. [53]. Copyright ©2015 Macmillan Publishers Limited. **(b)** HHG process in the nonperturbative regime. The peak intensity of the few-cycle NIR laser is about $1.7 \times 10^{14} \text{W/cm}^2$. The experimental data (red solid line) are compared to the calculations using TDCIS (blue solid line) and those using a reduced one-electron model (red dashed line). The data are taken from Refs. [58, 76].

ond category abandons the use of the N -electron wave function and adopts a reduced, lower dimensional entity to describe the physical state of the system, e.g., one-particle density and one-body reduced density matrix. This includes time-dependent density functional theory (TDDFT) [70], time-dependent two-particle reduced-density-matrix (TD 2-RDM) method [71], and time-dependent renormalized natural orbital (TDRNOT) theory [72].

The wave-function-based many-electron theories have the particular advantage that they can be improved in a well-controlled, systematic manner (cf. TDDFT) [30]. The TDCIS approach is the first of this kind that is used to solve nonperturbative ionization problems. Its relatively high numerical efficiency makes it currently the only one that can handle the strong-field dynamics for systems as complex as Xe [31, 66, 67, 73–75].

In order to demonstrate the quantitative capacity of TDCIS, two examples are given here; both of them are closely related to the content of this thesis. The first example involves the

of physical systems beyond atoms and molecules, such as solid-state [68] and many-boson [69] systems.

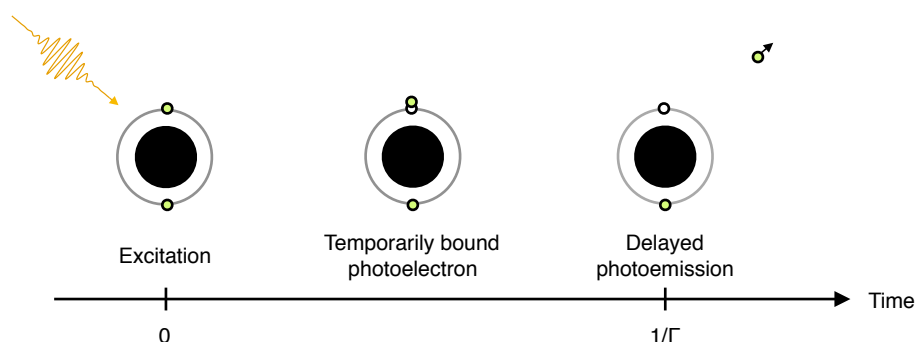


Figure 1.6. Schematic view of resonance dynamics. After photoexcitation, the electron is bound to the ion for a while, and then gets emitted. The lifetime of this transient state is characterized by $1/\Gamma$. In the case of shape resonances, the electron is temporarily trapped due to the presence of a potential barrier.

perturbative 2-photon ATI of Xe under the irradiance of XUV FELs [53]. The photoelectron yields as a function of the FEL intensity at a photon energy of 140 eV are shown in Fig. 1.5(a). The results of TDCIS are in quantitative agreement with the experimental data taken at the Free-Electron LASer in Hamburg (FLASH). The second example is the nonperturbative HHG of Xe driven by an intense NIR laser [76]. The spectrum of the HHG emission is shown in Fig. 1.5(b). There, a giant enhancement centered around 100 eV is observed experimentally and deviates from the typical flat plateau structure, which can be explained and reproduced by TDCIS [58]. In Figs. 1.5(a) and (b), the numerical results based on a reduced one-electron model are also shown. The discrepancy between the TDCIS and one-particle calculations exemplifies the importance of electronic correlation effects during photoionization, in both of the two regimes of light-matter interaction.

1.4 Attosecond tunneling dynamics in perturbative to nonperturbative photoionization of Xe

The central theme of this thesis deals with a particular type of photoionization dynamics that entails electron tunneling, or electronic shape-type resonances at the one-particle level. A shape resonance is a purely quantum phenomenon, where a photoelectron is trapped by a potential barrier for a while, tunnels through the barrier, and gets emitted, resulting in delayed photoemission (see Fig. 1.6) [77, 78]. Each possible resonance process is typified by the formation and the decay of a metastable state, or a resonance state, with a discrete and

complex energy, often called the Siegert energy:

$$E = \Xi - i\frac{\Gamma}{2}, \quad (1.2)$$

where the real part of the energy specifies the excitation energy of the resonance, and the imaginary part tells the tunneling rate, or the inverse lifetime of the quasibound electron before it escapes to the asymptotes. Such a fundamental quantum state can manifest itself, e.g., as a resonance-like feature centered at a position of Ξ and with a width of Γ in the linear photoabsorption cross section [79].

Two case studies on light-induced resonance phenomena are included in this thesis [see Figs. 1.7(a) and (b)]: one in the perturbative and another in the nonperturbative photoionization regime. There are two common features shared by these studies. First, the resonance dynamics investigated can be accessed or detected using modern light sources and spectroscopy techniques. In particular, both studies involve resonances that decay or even evolve on the attosecond time scale. As such, these subjects are particularly suited for the experiments based on attosecond technology. Second, both studies select Xe as the target species. In addition to the ease for sample preparation, Xe serves as an ideal candidate for learning the properties that emerge as the complexity of the electronic system increases.

TDCIS forms the theoretical backbone of our studies for its efficiency to handle multi-electron systems over a broad interaction range. Resonance dynamics are contained in the wave-packet propagation [78]. However, they can also be described by an eigenstate approach based on non-Hermitian quantum mechanics (NHQM) [77, 80]. NHQM transforms a resonance, which is represented by a collection of continuum states in standard Hermitian quantum mechanics, into one single bound-state-like eigenstate of a modified non-Hermitian Hamiltonian. In addition to providing a very simple description of resonances, NHQM gives complete information on the resonance states, including the Siegert energies and the resonance wave functions. NHQM can be combined with TDCIS to solve N -electron time-independent Schrödinger equation (TISE) with the modified Hamiltonian [48, 56]. This thesis takes both the dynamic and eigenstate approaches in order to gain complementary insights into the resonance dynamics.

In below, we briefly introduce the topics of the two case studies and explain the contributions presented by this thesis. In-depth introduction to each topic will be given in later chapters. Each study makes two main contributions to the research topic.

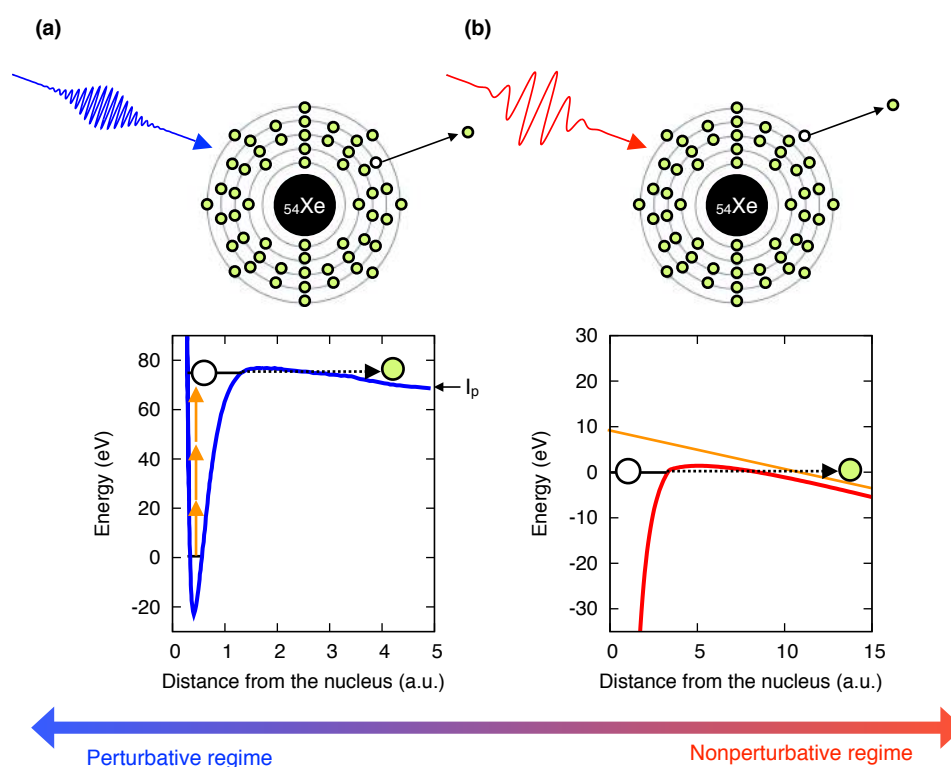


Figure 1.7. Two case studies of resonance dynamics in Xe in two different regimes of light-matter coupling presented in this thesis. For notations see Figs. 1.3(a) and (b). **(a)** In the perturbative regime, resonance dynamics is induced by XUV light and happens in the $4d$ inner shell. The excited f -wave photoelectron sees a field-free potential with a centrifugal barrier associated with its high angular momentum (blue curve), and is temporarily trapped before tunneling out. **(b)** In the nonperturbative regime, resonance dynamics is induced by NIR light and happens in the $5p$ valence shell. The ground-state electron sees the tilted potential (red curve), and is temporarily trapped before tunneling out. The potential is calculated using the Hartree-Fock-Slate method with the latter-tail correction [81].

1.4.1 Collective resonance behavior of Xe

The first case study in this dissertation concerns the XUV perturbative photoionization of Xe. Here, one to few-photon MPI processes excite an electron to a short-lived resonance state of the field-free potential, leading to ionization from the inner $4d$ subshell of Xe [see Fig. 1.7(a)].

This case is chosen precisely because the one-particle picture of shape resonances fails conspicuously: the transient trapping of the energetic electron in a short-range centrifugal potential barrier provides excellent conditions that incubate strong particle-hole interaction [29]. The collective electronic behavior of Xe has been studied extensively in the linear-response regime, where it is known as the giant dipole resonance (GDR) and was first observed in 1964 [82, 83]. Thanks to meticulous many-body theoretical studies in the next two decades, it is now well established that the broad, powerful spectroscopic feature of the GDR in XUV linear spectroscopy stems from the cooperative, plasma-like motion of at least all the $4d$ electrons [84, 85]. The GDR of Xe can also be found in other heavy elements in atomic, molecular, and solid environments [86], and is closely connected to the collective behavior of atomic nuclei, metallic clusters, and fullerenes [84].^e

The GDR continues to play a key role in today's science, because it strongly modifies the nonlinear response of Xe to advanced light sources. In fact, the peculiar enhancement of the HHG of Xe shown in Fig. 1.5(b) is a mirror of the GDR one-photon spectrum [58, 76]. Currently, what we know about the collective behavior of Xe is entirely drawn from linear-response studies. In the first application presented in this thesis, we overcome this limitation and make the following two contributions:

- *Contribution 1:* We start with the GDR in the linear regime. While the one-photon ionization spectrum has been accurately calculated by various advanced many-body theories, an interesting question that has been largely overlooked is that what exactly are the resonance states that give rise to the spectroscopic feature.

Using a TDCIS wave-packet technique that is designed for handling overlapping resonances and an NHQM eigenstate technique, we find that the GDR is composed of two short-lived collective dipole resonances and achieve the first characterization of the resonance parameters. Although this resonance substructure cannot be resolved

^eIn fact, the term “GDR” is borrowed from nuclear physics. The nuclear GDR had been observed and understood much earlier than the atomic GDR. Since nucleons are bound together by short-range forces, it is more natural to develop collective behavior in this circumstance.

by XUV linear spectroscopy, it has been substantiated by the XUV ATI experiment described in Fig. 1.5(a) [53]. Additionally, this substructure may well be measured by directly adopting the attosecond technique described in Ref. [19, 87], which detects a photoemission time delay due to molecular shape resonances.

- *Contribution 2:* Since NHQM solves all the fundamental resonance states within the available Hilbert space, we use it to investigate various types of correlated resonances—be them dipole or multipole modes—all at once. We then connect these correlated resonances to their spectroscopic fingerprints.

We find that linear-response studies can only reveal partial information on the GDR substructure owing to quantum interferences and thus cannot be used to explain the collective nature of the GDR. Furthermore, we predict the existence of hitherto unknown collective multipole resonances (with $1/\Gamma > 100$ as), which live far longer than the dipole modes. As a first step, we propose how to measure them with a combination of XUV-FELs and lower-order HHG sources. Our showcase study on Xe provides a fresh way to understand spectroscopic data of collective excitations in and beyond the linear regime.

1.4.2 Subcycle strong-field–ionization dynamics of Xe

The second case study in this dissertation concerns the NIR nonperturbative photoionization of Xe. Because of SFI, the light-induced ground state itself is a resonance state in the laser-tilted potential, resulting in ionization from the valence $5p$ subshell [see Fig. 1.7(b)]. Here, the resonance state not only decays but also evolves on the attosecond time scale.

The SFI mechanism was first proposed by Keldysh in 1964 [88]. It is not only the very first step to understand the nonperturbative behavior of electronic systems in the presence of intense electromagnetic fields, but also leads to several technological applications (e.g., HHG, the synthesis of attosecond pulses). Around 1990's, SFI had been already studied very well in a time-integrated manner, both experimentally (by measuring the yields of charged particles) and theoretically (by calculating the cycle-averaged ionization rates) [8, 23]. The high-power laser fields that trigger SFI typically oscillate with a period of a few femtoseconds. With the birth of attosecond spectroscopy, the SFI process can now be examined in greater detail—by directly looking into each laser cycle.

The first subcycle-resolved observation of SFI was performed on Ne in 2007 using attosecond streaking photoelectron spectroscopy [89], and the second was performed on Kr in

2011 by means of attosecond transient absorption spectroscopy (ATAS) [90]. In the second application presented in this thesis, we report the results of our experiment-theory collaboration, where we employ ATAS to follow the real-time SFI dynamics of a heavy, ‘fuzzy’ Xe atom beyond lighter elements.

- *Contribution 1:* Although the principle behind ATAS is conceptually very intuitive, it is a spectroscopy lacking sound theoretical foundation: there is no analytical theory that rigorously maps the ATAS signal to the ion population at the arrival time of the probe when the pump and probe pulses overlap temporally, a prerequisite to tracking the strong-field ion-creation process.

Through a detailed comparison between experimental data and TDCIS simulations, we investigate to which extent ATAS can be used to take ultrafast movies of SFI for two spin-orbit-split states of Xe^+ . We verify that ATAS is able to capture important features of the SFI dynamics of Xe, including the ionization steps and a previously unobserved oscillating feature. The deviation of the reconstructed SFI dynamics from the actual SFI dynamics reflects an intrinsic limitation of the ATAS technique. This pump-induced artifact is expected to be system-dependent and needs to be taken into account for the interpretation of minute features of ATAS data.

- *Contribution 2:* Within the confidential level of the experimental and calculated ATAS signals, we observe the SFI dynamics of Xe exhibit pronounced oscillations occurring at twice of the pump-pulse frequency. This oscillatory behavior cannot be explained by standard SFI models, which predict a monotonic growth of ion populations over time. By comparing TDCIS to NHQM-based tunneling-rate calculations, we pinpoint the physical origin of the half-cycle oscillations. They arise from strong-field-induced polarization of Xe, which periodically displaces the electron cloud without ionizing it. Albeit well known in the weak-field regime, the role polarization had so far been largely unnoticed in the strong-field regime. Because of the high polarizability of Xe, the dual nature of the electron motion in strong optical fields comes into light: it contains both a reversible facet (due to polarization) and an irreversible one (due to SFI)—they are in fact two sides of the tunneling resonance state. Our results suggest that the standard tunneling picture requires further refinement: in the presence of a strong optical field, it is no longer sufficient to think of an electron tunneling out from the field-free ground state; instead, the effects of field-induced bound electronic structure shall be incorporated. This aspect is anticipated to be of particular importance for understanding the time-resolved strongly driven behavior of complex, extended electronic systems.

1.4.3 Outline of the thesis

The outline of the thesis is as follows.

First, I review the fundamentals of the theories employed in this dissertation.

- Chapter 2 explains how to theoretically describe photoionization dynamics of an N -electron atom consistently in weak to strong fields and how to numerically solve the resulting N -electron TDSE using TDCIS.

During my doctoral study, I have co-developed the XCID package [49], a practical implementation of TDCIS in the group of Prof. Robin Santra (CFEL, DESY). Apart from new software modules for data analysis, the capacity to compute photoelectron spectra has also been added, which leads to the publication of Ref. [47]. For the sake of coherence, this paper is excluded from the thesis.

- Chapter 3 discusses how to theoretically describe resonances and how to numerically calculate the resonance eigenstates using NHQM.

Whereas NHQM, or more specifically the complex scaling method, is usually used to address resonance phenomena in few-electron systems including atoms and molecules, it had not been used before for a system with as many electrons as Xe. In particular, this thesis presents the first application of such a method for the study of collective electronic resonances.

Next, I present the original physical insights offered by this dissertation. The above two theories are applied to the investigation of photoionization processes that involve resonance states decay or even evolve on the subfemtosecond time scale. The heavy element Xe is chosen as the subject of study in order to exploit and explore features absent in few-electron systems.

- Chapter 4 starts with the ultrafast tunneling dynamics, i.e., the collective resonance behavior, in the perturbative XUV inner-shell photoionization of Xe. By means of an enhanced wave-packet analysis and an NHQM technique, I demonstrate how to expose the hidden substructure of the GDR. Continuing with the NHQM method, I show what are the many-body nature and the spectroscopic fingerprints of different types of collective resonances accessible in and beyond the linear-response regime.

These results have been published in Ref. [52] and Ref. [91]; in both of them I am the first author.

- Chapter 5 moves into the ultrafast tunneling dynamics, i.e., the subcycle SFI dynamics, in the nonperturbative NIR valence-shell photoionization of Xe. I show how ATAS can be utilized to take ultrafast snapshots of the SFI and validate the quantitative ability of TDCIS. By comparing full TDCIS to NHQM-based tunneling-rate simulations, I illustrate how to identify the mechanism behind the unexpected oscillatory character of the observed SFI dynamics.

These results have been published in Ref. [60], where I am a co-first author.

Finally, I conclude this dissertation.

- Chapter 6 summarizes the contributions of the thesis and provides outlook for future research opportunities.

Chapter 2

Theory of light-matter interaction

A central theme running throughout this thesis is the interaction between light and matter's electronic degrees of freedom. In this chapter, we introduce the theoretical foundations that are suitable for the description and the numerical solution of such interaction over a broad coupling range.

Section 2.1 is a pedagogical guide towards the N -electron Schrödinger equation solved in this thesis. First-principles simulation of the multielectron dynamics in the nonperturbative limit involves enormous complexity. Hence, one needs to resort to an approximation scheme that can efficiently represent the N -body Hilbert space and, at the same time, retain the essential many-body physics. This thesis takes on the TDCIS approach, which currently stands as the only approach capable of tackling the strong-field-driven dynamics of Xe in

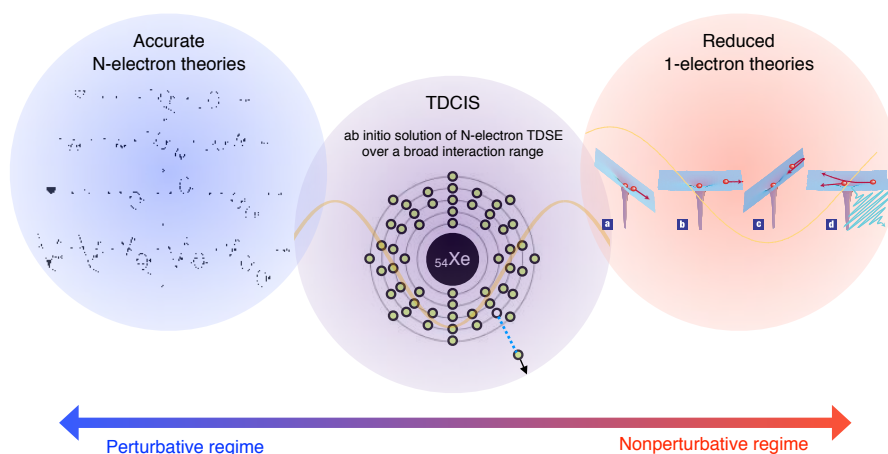


Figure 2.1. Topic of this chapter: theoretical description and numerical solution of photoionization dynamics of an N -electron system. For detailed description of the figure see the caption of Fig. 1.4.

full dimensionality. Section 2.2 presents the major concepts of TDCIS. Section 2.3 briefly goes into the implementation of TDCIS on a numerical grid. Section 2.4 provides a chapter summary.

2.1 Theoretical description of light-matter interaction

In this section, we go through the steps that give us the expression for the N -electron Hamiltonian and the Schrödinger equation.

2.1.1 The N -electron Schrödinger equation

Minimal-coupling principle. Let us first consider a classical system of an N -electron atom and a light field. The atom is made of particles, i.e., electrons and a nucleus. Assume the i -th particle carries a charge q_i , a mass m_i , and a canonical momentum \mathbf{p}_i at a position \mathbf{r}_i . The charged particles are immersed in an electromagnetic (EM) field, described by a vector potential \mathbf{A} and a scalar potential Φ , that is established together by the particles themselves and the radiation. According to the *principle of minimal coupling* [28, 92], the Hamiltonian in the presence of EM interaction can be obtained from the interaction-free Hamiltonian by making the substitutions for each free particle:

$$\mathbf{p}_i \rightarrow \mathbf{p}_i - q_i \mathbf{A}(\mathbf{r}_i, t), \quad h_i \rightarrow h_i + q_i \Phi(\mathbf{r}_i, t), \quad (2.1)$$

namely, replacing the canonical momentum with the kinematical momentum, which decides the velocity \mathbf{v}_i [92, 93],

$$\mathbf{p}_i - q_i \mathbf{A} = m_i \mathbf{v}_i, \quad (2.2)$$

and adding the scalar potential to the individual free-particle Hamiltonian h_i . The Hamiltonian resulting from Eq. (2.1) is able to reproduce the relevant classical equations of motion. The coupling between each particle and the electromagnetic field is “minimal” in the sense that it relies entirely on particle’s electric charge but not higher multipole moments [94, 95].

Coulomb gauge and the EM potentials. Before writing down the actual Hamiltonian, let us take a deeper look into the electromagnetic potentials. The potentials \mathbf{A} and Φ are connected

to the electric component \mathbf{E} and the magnetic component \mathbf{B} of the EM field via [96]

$$\mathbf{E}(\mathbf{r}, t) = -\partial_t \mathbf{A} - \nabla \Phi, \quad (2.3)$$

$$\mathbf{B}(\mathbf{r}, t) = \nabla \times \mathbf{A}. \quad (2.4)$$

The derivative relations provide an arbitrariness in choosing the potentials without modifying the physically measurable fields \mathbf{E} and \mathbf{B} . We thus have the freedom to perform gauge transformations^a

$$\mathbf{A} \rightarrow \mathbf{A} + \nabla \chi(\mathbf{r}, t), \quad \Phi \rightarrow \Phi - \partial_t \chi(\mathbf{r}, t). \quad (2.5)$$

Since we do not require a relativistically covariant theory, it is convenient to adopt the *Coulomb gauge* [92, 96]

$$\nabla \cdot \mathbf{A} = 0, \quad (2.6)$$

where the Maxwell's equations in terms of the potentials read

$$\nabla^2 \Phi = -4\pi \sum q_i \delta(\mathbf{r} - \mathbf{r}_i), \quad (2.7)$$

$$(\nabla^2 - c^{-2} \partial_t^2) \mathbf{A} = -4\pi c^{-2} \sum \mathbf{j}_i^\perp(\mathbf{r}, t), \quad (2.8)$$

with \mathbf{j}_i^\perp the transverse current due to the i -th particle.^b Eq. (2.7) is simply Poisson's equation with the solution

$$\Phi = \sum \frac{q_i}{|\mathbf{r} - \mathbf{r}_i|}, \quad (2.9)$$

that is, the Coulomb potential generated by the instantaneous charge distribution. On the other hand, Eq. (2.8) shows that the purely transverse \mathbf{A} satisfies the wave equation with an implied propagation speed c [98]. By virtue of the Coulomb gauge, Φ splits out as the familiar electrostatic Coulomb potential, and \mathbf{A} bears all the dynamical aspects of the EM field. In addition, \mathbf{A} and Φ contribute separately to the transverse \mathbf{E}^\perp and longitudinal \mathbf{E}^\parallel parts of the electric field $\mathbf{E} = \mathbf{E}^\perp + \mathbf{E}^\parallel$ [92]:

$$\mathbf{E}^\perp = -\partial_t \mathbf{A} \quad (\nabla \cdot \mathbf{E}^\perp = 0), \quad (2.10)$$

$$\mathbf{E}^\parallel = -\nabla \Phi \quad (\nabla \times \mathbf{E}^\parallel = \mathbf{0}). \quad (2.11)$$

^aFor a quantized atom, as soon as a new pair of \mathbf{A} and Φ is chosen, the atomic wave function must simultaneously undergo a unitary transformation, $|\Psi(t)\rangle \rightarrow \exp[i \sum q_i \chi(\mathbf{r}_i, t)] |\Psi(t)\rangle$, such that the form of TDSE remains unchanged [28]. This gauge-invariant requirement can also be used in reverse to derive the minimal-coupling Hamiltonian: the substitutions in Eq. (2.1) amount to the simplest prescription demanded by local gauge symmetry in electromagnetism [94, 97].

^bThe α -th spatial component of the transverse current is $j_{i,\alpha}^\perp(\mathbf{r}, t) = \sum_\beta \delta_{\alpha\beta}^\perp(\mathbf{r} - \mathbf{r}_i) q_i v_{i,\beta}$ [92]. The transverse delta dyadic $\delta_{\alpha\beta}^\perp(\mathbf{r}) = 2/3 \delta_{\alpha\beta} \delta(\mathbf{r}) - (4\pi r^3)^{-1} (\delta_{\alpha\beta} - 3\hat{r}_\alpha \hat{r}_\beta)$, with \hat{r} the unit vector of \mathbf{r} .

Heading towards the N-electron Schrödinger equation. Applying what we have learned so far and canonical quantization to the atom-radiation system, one can arrive at the most rigorous theory of atom-photon interaction [92, 99]. However, solving such a theory of everything is generally impossible, and approximations have to be made depending on the nature of the problems at hand. In what follows, we quickly walk through the steps that lead us to the N -electron Schrödinger equation, a theoretical framework suitable for the description of photoionization in a wide range of experimental conditions [28].

In the first step, the \mathbf{A} field is taken as an *external driver* [28, 99]—it is like a predefined input parameter, whose evolution obeys the homogeneous wave equation with no source term [cf. Eq. (2.8)]. This assumption is reasonable when incident radiation interacts with one single atom in such a way that any influence on \mathbf{A} by the matter present is negligibly small. As a result, our focus is zoomed in from the closed atom-radiation system into the open atomic (sub)system.

In the second step, we employ the *semiclassical theory of light-matter interaction* [28, 100]. Even a comparatively weak, single-mode radiation field used in linear spectroscopy contains a macroscopic number of photons, which can essentially be seen as a continuous variable ($n + 1 \approx n$). Therefore, the light field \mathbf{A} is kept as a classical entity, and only the atom, including Φ , needs to be quantized.

In the third step, we refrain from going into the relativistic domain and stay in the realm of *nonrelativistic electrodynamics* [28, 92]. This constraint holds as long as the relevant energy scales lie well below the electron rest energy $m_e c^2 \approx 0.5$ MeV [101]. Accordingly, the individual free-particle Hamiltonian $h_i = \mathbf{p}_i^2 / (2m_i)$ is utilized for the minimal substitutions in Eq. (2.1).

Combining the above three steps with Eqs. (2.6) and (2.9), we acquire the standard non-relativistic, semiclassical Hamiltonian for a many-particle system driven by external radiation [28, 92]

$$H(t) = \sum_i \left[\frac{(\mathbf{p}_i - q_i \mathbf{A})^2}{2m_i} + q_i \Phi \right] \quad (2.12)$$

$$= \sum_i \frac{\mathbf{p}_i^2}{2m_i} + \sum_{i < j} \frac{q_i q_j}{|\mathbf{r}_i - \mathbf{r}_j|} - \sum_i \frac{q_i \mathbf{A} \cdot \mathbf{p}_i}{m_i} + \sum_i \frac{q_i^2 \mathbf{A}^2}{2m_i}. \quad (2.13)$$

Here, \mathbf{r}_i 's and \mathbf{p}_i 's have been elevated into operators in Schrödinger's picture using first quantization, whereas \mathbf{A} is a c -number field. The first two terms in the total Hamiltonian H in Eq. (2.13) constitute the radiation-free Hamiltonian of the matter. The last two terms repre-

sent two types of light-matter coupling; both of them enter H in a nonperturbative manner. Note that the Hamiltonian for the EM wave is absent.

The radiation wavelength considered in this thesis ($\lambda_{\text{XUV}} \sim 10^1$ nm, $\lambda_{\text{NIR}} \sim 10^3$ nm) is much larger than the atomic dimension ($\sim 10^{-1}$ nm). This enables us to introduce the *dipole approximation* [28], under which the vector potential \mathbf{A} is spatially uniform across the atom and is a function of time alone.

By exploiting the high proton-electron mass ratio $m_p/m_e \approx 1.8 \times 10^3$ [101], we further make the *clamped-nuclei approximation* [28]. This means that the atomic nucleus is presumed infinitely heavy and fixed in space, say, at the origin.

Finally, by setting $q_e = m_e = 1$ and the nuclear charge to Z in Eq. (2.13), the *time-dependent N -electron Hamiltonian* takes on the form [28]

$$H(t) = \left\{ \sum_{n=1}^N \frac{\mathbf{p}_n^2}{2} - \sum_{n=1}^N \frac{Z}{|\mathbf{r}_n|} + \sum_{\substack{n,n'=1 \\ n < n'}}^N \frac{1}{|\mathbf{r}_n - \mathbf{r}_{n'}|} \right\} + \left\{ \mathbf{A}(t) \cdot \sum_{n=1}^N \mathbf{p}_n + \frac{N}{2} \mathbf{A}^2(t) \right\} \quad (2.14)$$

$$=: H_{\text{atom}} + H_{\text{int}}(t). \quad (2.15)$$

The free atomic Hamiltonian H_{atom} contains the electron kinetic energy, the electron-nucleus attraction, and the electron-electron repulsion. As a legacy of the dipole approximation, the $\mathbf{A} \cdot \sum \mathbf{p}_n$ term in the atom-radiation interaction H_{int} only induces electric dipole E1 transitions; the \mathbf{A}^2 term is merely a global energy shift and has no physical significance.

The atomic quantum state is specified by an *N -electron wave function* $|\Psi\rangle$, whose dynamics is given by the *time-dependent Schrödinger equation (TDSE)* [28]

$$i\partial_t |\Psi(t)\rangle = H(t) |\Psi(t)\rangle. \quad (2.16)$$

Unless otherwise stated, the atom is supposed to be in a pure state of the electronic ground state before the radiation arrives, implying the *zero-temperature restriction*. For noble gases, the product of the Boltzmann constant and room temperature ($\sim 10^{-2}$ eV) is much bigger than the energy gap between the ground state and the first excited state ($\sim 10^1$ eV) [102]. It is hence unnecessary to perform thermal statistical averaging over the initial-state distribution.

It is often informative to know the field-free (e.g., in Chapter 4) or instantaneous field-dressed (e.g., in Chapter 5) electronic structure by seeking the eigensolutions of the *time-independent Schrödinger equation (TISE)* [28]

$$H_{\text{atom}} |\Psi\rangle = E |\Psi\rangle \quad \text{or} \quad H(t) |\Psi\rangle = E |\Psi\rangle. \quad (2.17)$$

Limitations of the theoretical formalism.

- By treating the incoming light as a fixed agent, our theory can only be used to extrapolate the behavior of a dilute gas sample (with a pressure $\sim 10^1$ Torr) [103]. This “microscopic” theory is in contrast to the “macroscopic” theory based on solving the coupled Maxwell-Schrödinger equations, which allows an *ab initio* treatment of propagation effects of the incident light field due to, e.g., photoabsorption and ion-induced dispersion [100, 103].
- Without explicitly discretizing the light field, our theory does not contain the physical processes triggered by vacuum fluctuations, e.g., fluorescence decay [28]. Such decay processes generally happen on the femtosecond time scale (i.e., slower than the processes we are interested in) and are beyond the scope of this thesis.
- H is spin-free, which may be regarded as a by-product of the nonrelativistic treatment since spin interaction appears in lowest-order expansion of the Dirac equation [28, 95]. Our theory neglects fine-structure splitting (which typically grows as one goes to a higher atomic number and into deeper shells) [28, 104] as well as relativistic aspects of the photoelectron motion in an ultraintense field ($I \gtrsim 10^{18}$ W/cm²) [28, 105]. If needed, spin-orbit coupling may be accommodated *ad hoc* utilizing perturbation theory (see Chapter 5) [28, 46].
- The dipole approximation gives $\mathbf{E}(t) = -\partial_t \mathbf{A}$, $\mathbf{B} = \mathbf{0}$ [see Eqs. (2.3) and (2.4)]. That is, we neglect the effects associated with the magnetic component of the light field. This assumption may breakdown when using an ultraintense laser ($I \gtrsim 10^{16}$ W/cm²), particularly because of magnetic effects comes into play, which cause the electron to drift along longitudinal propagation direction [28, 105].

2.1.2 Different frames of light-matter interaction

There is more than one way to describe light-matter coupling semiclassically. Suppose $|\Psi\rangle$ is a solution of the N -electron TDSE with H specified by Eq. (2.14). Then, conducting a unitary transformation of the wave function and an accompanying transformation of the Hamiltonian

$$|\Psi\rangle \rightarrow U(\mathbf{r}_n, \mathbf{p}_n, t)|\Psi\rangle, \quad H \rightarrow UHU^\dagger - iU\partial_t U^\dagger, \quad (2.18)$$

takes us to other equivalent *frames* of light-matter interaction, where TDSE will be equally satisfied with the new ket and the new Hamiltonian.

Velocity frame. As discussed before, the $\sum \mathbf{A}^2(t)$ term in H_{int} in Eq. (2.14) under the dipole approximation has no physical role. It can be directly eliminated using the unitary transformation

$$U^V(t) = \exp \left[i \frac{N}{2} \int^t dt' \mathbf{A}^2(t') \right]. \quad (2.19)$$

This brings us to the so-called *velocity frame* of light-matter interaction

$$|\Psi\rangle^V = U^V |\Psi\rangle, \quad (2.20)$$

$$H^V = H_{\text{atom}} + H_{\text{int}}^V, \quad H_{\text{int}}^V := \mathbf{A}(t) \cdot \mathbf{P}, \quad (2.21)$$

since H_{int}^V couples the vector potential \mathbf{A} to the N -electron momentum operator $\mathbf{P} = \sum \mathbf{p}_n$. But be careful: the velocity of each electron is actually given by the kinematical momentum $\mathbf{p}_n + \mathbf{A}$, i.e., the quantity appearing in the minimal substitutions in Eq. (2.1), rather than by the canonical momentum \mathbf{p}_n .

Length frame. Another popular choice is the Göppert-Mayer transformation

$$U^L(\mathbf{r}_n, t) = \exp[-i \mathbf{A} \cdot \mathbf{R}]. \quad (2.22)$$

This leads us to the *length frame* of light-matter interaction

$$|\Psi\rangle^L = U^L |\Psi\rangle, \quad (2.23)$$

$$H^L = H_{\text{atom}} + H_{\text{int}}^L, \quad H_{\text{int}}^L := -\mathbf{E}^\perp(t) \cdot \mathbf{R}, \quad (2.24)$$

where H_{int}^L depends on the transverse electric field \mathbf{E}^\perp owing to the external radiation and the total position operator $\mathbf{R} = \sum \mathbf{r}_n$. This frame is particularly useful to picture photoionization in the strong-field regime: the light-induced tilted potential introduced in Chapter 1 comes precisely from the H_{int}^L in the one-particle limit (see Fig. 1.3).

It is worthwhile to point out that U^V and U^L correspond to gauge transformations in electromagnetism as defined in Eq. (2.5). Thus, the two frames are also said to be the *velocity gauge* and the *length gauge* of TDSE, respectively. By comparing Eqs. (2.19) and (2.20) to Fn. (a), U^V is a global gauge transformation with $\chi^V(t) = -1/2 \int^t dt' \mathbf{A}^2$. It follows that $\mathbf{A} = \mathbf{A}^V$ in Eq. (2.21). On the other hand, U^L is a local gauge transformation with $\chi^L(\mathbf{r}, t) = -\mathbf{A} \cdot \mathbf{r}$. Note that \mathbf{E}^\perp in Eq. (2.24) is itself a gauge-independent quantity, but $\mathbf{E}^\perp \neq -\partial_t \mathbf{A}^L$ [cf. Eq. (2.11)].

Apart from the velocity and length frames, there are of course an infinite number of other possibilities, such as the *acceleration* or *Kramers-Henneberger frame*. The unitary operator $U^A(\mathbf{p}_n, t)$ is a coordinate transformation into the rest frame of a classical electron quivering in \mathbf{E}^\perp , where the radiation effect is recast into a time-dependent nuclear potential [28].

Even though various frames defined in Eq. 2.18 are said to be equivalent, particular attention has to be paid to the calculation of the expectation value of an observable $\langle O \rangle$, which is the same as what calculated in the old Coulomb gauge if the operator remains unchanged under the transformation $UOU^\dagger = O$. Such observables, in the case of velocity and length gauges, are the coordinate operator and the kinematic momentum.

Even for gauge-invariant quantities, different frames may yield different numerical results as a consequence of the incomplete basis set used [106]. This can actually give a positive twist: the results of different gauges may be used to cross-check the quality of the basis set [107].

2.2 Ab initio solution of light-matter interaction

The N -electron TDSE in Eq. (2.16) with the velocity-gauge Hamiltonian (2.21) or the length-gauge Hamiltonian (2.24) forms the theoretical foundation of photoionization dynamics.

Despite of the seeming straightforwardness, the presence of two-electron interaction renders direct numerical solution of TDSE impossible except for systems with up to three electrons, such as He, H₂, and Li [30, 31]. As the number of electrons increases, the wavefunction representation becomes too complex to be computationally tractable, hitting “the curse of dimensionality” [108]. Apparently, one has to resort to an approximate description of the multielectron wave function, using, e.g., the TDCIS approach taken by this thesis.

This section presents the basics of TDCIS, a first-principles wave-function-based theory that enables the simulation of N -electron TDSE and the inclusion of essential many-body physics, in and between the two ionization limits.

2.2.1 Concept of configuration interaction

Our major task is to look for an efficient and accurate enough representation for the correlated N -electron problem. This kind of topics lies right at the heart of *ab initio* quantum chemistry,

whose tools we can borrow. Traditionally, its focus is on solving the field-free electronic structure, namely on solving TISE with $\hat{H} = \hat{H}_{\text{atom}}$ in Eq. (2.17), so let us start from there.

Configuration interaction (CI) is a widely used many-body theory that provides a simple and systematic strategy to go beyond the independent-particle mean-field (MF) theory [109, 110]. We first rearrange \hat{H}_{atom} in Eq. (2.13) into two parts,

$$\hat{H}_{\text{atom}} = \underbrace{\sum_{n=1}^N \left(\frac{\hat{p}_n^2}{2} - \frac{Z}{|\hat{r}_n|} + v_{\text{MF}} \right)}_{\hat{H}_0} + \underbrace{\frac{1}{2} \sum_{\substack{n,n'=1 \\ n \neq n'}}^N \frac{1}{|\hat{r}_n - \hat{r}_{n'}|} - \sum_{n=1}^N v_{\text{MF}}}_{\hat{H}_1} - E_0, \quad (2.25)$$

by introducing the nonlocal Hartree-Fock (HF) potential v_{MF} ; if the exchange potential is simplified by the local density approximation, v_{MF} reduces to the local Hartree-Fock-Slater (HFS) potential [110]. In Eq. (2.25), \hat{H}_0 is just the MF Hamiltonian summing over the one-body Fock operators [109], while \hat{H}_1 captures the residual electron-electron interaction beyond what can be described on the MF level. The subtraction of the HF ground-state energy E_0 is done for cosmetic purposes.

MF reference state. As one of the post-HF methods, CI tackles an exact multielectron eigenfunction by taking an MF state, typically the ground state, as a *reference* [109, 110]. For convenience, we adopt the language of second quantization and treat electrons as excitations of a quantum field [109]. The HF ground state $|\Phi_0\rangle$, which is presumed a closed-shell Slater determinant of N spin orbitals $|\phi_i\rangle$, now takes on the form

$$|\Phi_0\rangle = \prod_{i=1}^N \hat{c}_i^\dagger |0\rangle, \quad (2.26)$$

where $|0\rangle$ denotes the vacuum state, and the operator \hat{c}_i^\dagger adds an electron into the i -th spin orbital.

Building up the N-body Hilbert space. The HF ground state is made up of the N energetically lowest orbitals $|\phi_i\rangle$ of all the MF spin orbitals. Hence, in addition to $|\Phi_0\rangle$, there is a large set of other N -electron Slater determinants to be explored. They can be obtained from $|\Phi_0\rangle$ by systematically moving electrons out of *occupied orbitals* in $|\Phi_0\rangle$ (labeled by i, j, \dots) and putting them back into *unoccupied or virtual orbitals* in $|\Phi_0\rangle$ (labeled by a, b, \dots) [109, 110].

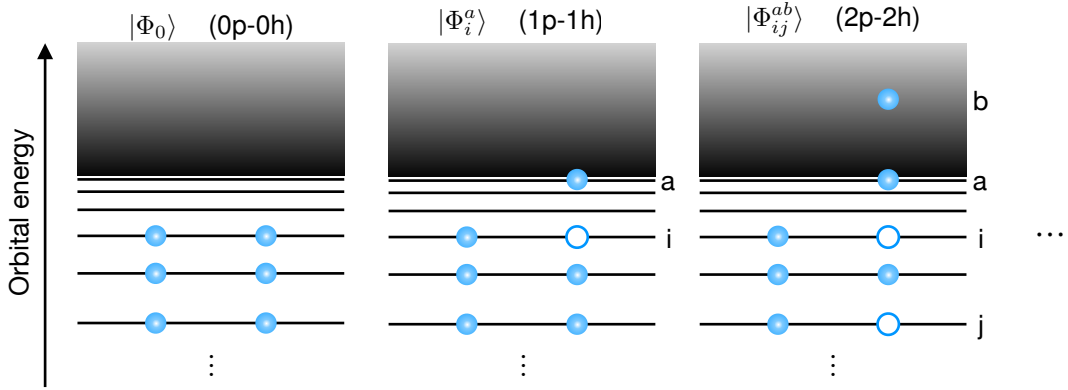


Figure 2.2. Schematic view of the construction of \mathbb{V}_{FCI} from the closed-shell MF reference state $|\Phi_0\rangle$. Each filled circle symbolizes an electron, and each open circle a hole. In restricted HF, two spin orbitals with the same spatial orbital but opposite spins are degenerate.

This procedure is illustrated in Fig. 2.2 and can be expressed as

$$\begin{aligned}
 |\Phi_0\rangle & & (0\text{p-}0\text{h}) & & (2.27) \\
 |\Phi_i^a\rangle = \hat{c}_a^\dagger \hat{c}_i |\Phi_0\rangle & & (1\text{p-}1\text{h}) & & \\
 |\Phi_{ij}^{ab}\rangle = \hat{c}_a^\dagger \hat{c}_b^\dagger \hat{c}_j \hat{c}_i |\Phi_0\rangle & & (2\text{p-}2\text{h}) & & \\
 \vdots & & \vdots & &
 \end{aligned}$$

For instance, the singly excited configuration $|\Phi_i^a\rangle$ can be formed by promoting an electron from orbital i to orbital a through the annihilation and creation operators \hat{c}_i and \hat{c}_a^\dagger [109]. The electron vacancy and the excited electron in $|\Phi_i^a\rangle$ are called a *hole* and a *particle*, respectively. The collection of $|\Phi_i^a\rangle$ comprises the one-particle–one-hole (1p-1h) excitation class in reference to $|\Phi_0\rangle$ (0p-0h). Similarly, doubly excited $|\Phi_{ij}^{ab}\rangle$ (2p-2h), ..., up to N -tuply excited ($N\text{p-}N\text{h}$) configurations can be built. Each determinant constructed in this way is an eigenvector of \hat{H}_0 [109]. The full configuration space $\mathbb{V}_{\text{FCI}} = \{|\Phi_0\rangle, |\Phi_i^a\rangle, |\Phi_{ij}^{ab}\rangle, \dots\}$ thereby represents a complete and orthonormal N -electron Hilbert space.

Mixing of the configurations. The basic idea of CI is to simply expand a true multielectron eigenstate of \hat{H}_{atom} using the eigenbasis of \hat{H}_0 [109, 110]. In general, a CI wave function is a linear combination of various Slater determinants. Such configuration mixing gives rise to a correlated or entangled many-body state beyond the MF picture [28].

Going back to our original task, we can utilize CI to generate a representation of our N -electron wave function. However, this representation is accurate but not efficient. The

full CI method performs the CI expansion using the entire \mathbb{V}_{FCI} , and, in principle, delivers an exact solution. Unfortunately, its practical application is rather limited even in the study of field-free static problems [109, 110], again, due to the curse of dimensionality.

In order to handle a system with many electrons, one has to employ a subspace of \mathbb{V}_{FCI} that is cut off at some excitation level. This leads to a family of truncated CI approaches, e.g., *configuration-interaction singles (CIS)* [109, 110]. Of course, the very notion of truncated CI offers the possibility to systematically improve the quality of the basis set and the degree of electronic correlation included.

2.2.2 Theory of time-dependent configuration-interaction singles

Now it is the time to transpose the idea of truncated CI from a static into a dynamical setting. In electronic-structure calculations, the ground and low-lying excited states, i.e., the states localized to the nucleus, are usually the center of attention [109, 110]. This is in sharp contrast to the situation when dealing with photoionization dynamics. Particularly in the strong-field regime, the wave packet is characterized by a huge portion of highly excited and delocalized continuum states. Because of that, one has to compromise on a truncated CI space with a relatively stringent restriction to make TDSE calculations numerically feasible.

Here, we apply the *time-dependent configuration-interaction–singles (TDCIS)* theory to simulate atomic photoionization dynamics over a broad interaction range [41–45]. Even though this is a first step beyond the MF treatment, as shown in Chapter 1, TDCIS already offers considerable predictive power and gives access to many-electron physics not attainable using one-electron theories.

Configuration space and wave-function ansatz. In TDCIS, the truncated CI space is directly taken from the *CIS configuration space*

$$\mathbb{V}_{\text{CIS}} = \{|\Phi_0\rangle, |\Phi_i^a\rangle\}, \quad (2.28)$$

which is limited up to the 1p-1h excitation class of \mathbb{V}_{FCI} [43, 45]. In strong-field calculations, the dimension of \mathbb{V}_{CIS} can easily reach the order of 10^6 [42]. Inclusion of 2p-2h or even higher excitation classes quickly turns the Hilbert space computationally unmanageable. We thus opt for \mathbb{V}_{CIS} and focus on the light- and correlation-induced electron dynamics therein.

The configurations $|\Phi_0\rangle$ and $|\Phi_i^a\rangle$ span an orthonormal basis, in which the N -electron wave function can be expanded. Since the basis functions are kept time-independent, the

CIS expansion coefficients are elevated into time-dependent variables to carry the dynamical information [43, 45]. The *TDCIS wave-function ansatz* is written as

$$|\Psi(t)\rangle = \alpha_0(t) |\Phi_0\rangle + \sum_{i,a} \alpha_i^a(t) |\Phi_i^a\rangle. \quad (2.29)$$

Diagonalization of the Hamiltonian. The time-dependent N -electron Hamiltonian $\hat{H}(t) = \hat{H}_0 + \hat{H}_1 + \hat{H}_{\text{int}}(t)$, among other operators, is also represented using $|\Phi_0\rangle$ and $|\Phi_i^a\rangle$. The solution of TISE in Eq. (2.17) can then be found by diagonalizing the Hamiltonian matrix [56]. This provides complete knowledge of the field-free or field-dressed electronic structure, including the eigenenergies as well as the eigenfunctions. Each eigenstate obeys the form of Eq. (2.29), with implicit time dependence through the field strength $\mathbf{A}(t)$ or $\mathbf{E}(t)$. When the ionization process is adequately modeled by the perturbation theory, these stationary solutions can be directly used to construct measurable quantities, e.g., (generalized) cross sections [24, 111].

Propagation of the wave function. Plugging the ansatz (2.29) into TDSE in Eq. (2.16) and making projections onto $|\Phi_0\rangle$ and $|\Phi_i^a\rangle$, the equation of motion (EOM) of $|\Psi\rangle$ is recast to a set of coupled EOMs for α_0 and α_i^a [43, 45]:^c

$$i\dot{\alpha}_0(t) = \sum_{i,a} \langle \Phi_0 | \hat{H}_{\text{int}}(t) | \Phi_i^a \rangle \alpha_i^a(t), \quad (2.30a)$$

$$i\dot{\alpha}_i^a(t) = (\epsilon_a - \epsilon_i) \alpha_i^a(t) \quad (2.30b)$$

$$+ \sum_{j,b} \langle \Phi_i^a | \hat{H}_1 | \Phi_j^b \rangle \alpha_j^b(t) \\ + \langle \Phi_i^a | \hat{H}_{\text{int}}(t) | \Phi_0 \rangle \alpha_0(t) + \sum_{j,b} \langle \Phi_i^a | \hat{H}_{\text{int}}(t) | \Phi_j^b \rangle \alpha_j^b(t).$$

In Eq. (2.30), either $\hat{H}_{\text{int}}^V(t) = \mathbf{A}(t) \cdot \hat{\mathbf{P}}$ (2.21) or $\hat{H}_{\text{int}}^L(t) = -\mathbf{E}(t) \cdot \hat{\mathbf{R}}$ (2.24) can be chosen; ϵ_a and ϵ_i stand for the orbital energies for spin orbitals a and i , respectively. With $|\Psi(t)\rangle$ at hand, we can compute expectation values and other physical quantities, e.g., the dipole moment in various forms [44], (generalized) photoabsorption cross section [46, 51, 53], emitted HHG spectrum [45], photoelectron distribution [47], just to name a few.

^cAlternatively, one can get the EOMs by means of the time-dependent variational principle [31, 112].

2.2.3 Multichannel physics and electronic correlation effects

TDCIS can be utilized not only to make quantitative predictions but also to extract physical insights from the simulations. To see how the latter aspect works, consider the following question: does the field-free MF orbital picture used to represent the wave function and the Hamiltonian—a picture that we carry around in our heads—have any physical significance under the influence of the residual Coulomb interaction \hat{H}_1 and the light-matter interaction $\hat{H}_{\text{int}}(t)$? Or, does it serve as a purely mathematical instrument?

A key advantage of TDCIS is its conceptual clarity: it actually allows us to attach physical meanings to certain types of MF solutions. This greatly facilitates the retrieval and the classification of the information content of the wave function, and, in turn, the manipulation of its dynamics in such a way that different multielectron effects can be easily evaluated. To begin with, let us return to and investigate the MF reference state.

MF ground state. On the CIS level, the field-free HF ground state is an eigenstate, in fact, the ground state, of the full atomic Hamiltonian \hat{H}_{atom} . The statement that there is no direct coupling between the 0h-0h and any 1p-1h determinant, i.e., $\langle \Phi_0 | \hat{H}_{\text{atom}} | \Phi_i^a \rangle = 0$, is known as *Brillouin's theorem* [43, 109]. As a result, $|\Phi_0\rangle$ is the initial state to launch the time propagation; this yields the initial conditions $\alpha_0(0) = 1$ and $\alpha_i^a(0) = 0$ for the EOMs in Eq. (2.30). More importantly, the field-free ground-state population is simply given by $|\alpha_0(t)|^2$ and any of its change is an exclusive consequence of \hat{H}_{int} [see Eq. (2.30a)].

MF ionic states, ionization channels, and ion density matrix. Unlike $|\Phi_0\rangle$, $|\Phi_i^a\rangle$ are not a CIS excited eigenstate and interact with each other via \hat{H}_1 [see the second term in Eq. (2.30b)]. Although interpreting each $|\Phi_i^a\rangle$ makes little sense, it is meaningful if we look at only a part of it, namely the ionic state with one electron missing in the i -th spin orbital, $|\Phi_i\rangle = \hat{c}_i |\Phi_0\rangle$. This amounts to viewing the photoexcited N -electron atom as two coupled subsystems: one excited electron and one ionic core with the remaining $(N - 1)$ electrons. Within \mathbb{V}_{CIS} , a field-free HF 1h ionic state is an ionic eigenstate of \hat{H}_{atom} and is decoupled from any other 1h determinant, i.e., $\langle \Phi_i | \hat{H}_{\text{atom}} | \Phi_j \rangle = 0$ for $i \neq j$ [43, 109]. Thanks to *Koopman's theorem*, values of the hole index i taken in the wave-function expansion in Eq. (2.29) immediately specify the ionic species produced by \hat{H}_{int} . Accordingly, i can be used to group $|\Psi(t)\rangle$ into

distinct *ionization channels*; the ionization potential of channel i is $-\epsilon_i$ [42, 43].^d

Once created, the ionic subsystem is generally not in a pure but a mixed ionic state. The state of the photoion is uniquely defined by the reduced *ion density matrix (IDM)*, which can be obtained by taking the partial trace of the total N -electron density matrix over the uninteresting degrees of freedom of the photoelectron [44, 113]. The IDM matrix elements read

$$\rho_{i,j}^{\text{IDM}}(t) = \sum_a \langle \Phi_i^a | \Psi(t) \rangle \langle \Psi(t) | \Phi_j^a \rangle. \quad (2.31)$$

The diagonal element $\rho_{i,i}^{\text{IDM}}$ represents the ion population in $|\Phi_i\rangle$; the off-diagonal one $\rho_{i,j}^{\text{IDM}}$ with $i \neq j$ indicates the coherence between $|\Phi_i\rangle$ and $|\Phi_j\rangle$.

Strictly speaking, the field-free ionic eigenstates are only “physical” when $\hat{H}_1(t)$ is more or less zero. Nevertheless, since $|\Phi_i\rangle$ are not much affected by the external light field, the hole index i , ionization channels, and IDM are relatively robust concepts even during strong light-atom interaction. This is supported by the pump-probe experiment in Chapter 5, where the observed valence-core transition lines sit at the field-free transition energies at a pump intensity on the order of 10^{14} W/cm².

As another remark, since we equate the formation of an ion to the formation of a hole, we do not differentiate between bound and continuum populations (if ion yields could ever be uniquely defined in an intense time-dependent field [30, 31, 114]). An excited state is seen as a bound p-h pair as in quantum defect theory [115] and solid-state physics [116].

Multichannel physics. Because the hole index i indicates the physical ionic state in the presence of \hat{H}_1 and $\hat{H}_{\text{int}}(t)$, it is employed to classify different channels of the photoionization dynamics. The light-matter interaction \hat{H}_{int} leads to the growth of the ion population in $|\Phi_i\rangle$. This is decided by the kind of matrix elements $\langle \Phi_i^a | \hat{H}_{\text{int}}(t) | \Phi_0 \rangle$ in Eq. (2.30b), which promotes an electron out of the i -th occupied spin orbital. Considering a set of i permits the creation of multiple photoion species [42, 43]. This *multichannel character* of TDCIS is depicted in Fig. 2.3. As such, TDCIS overcomes the constraint of the one-channel single-active-electron (SAE) approximation commonly used in strong-field calculations, where the photoelectron is allowed to come out of only the outermost occupied orbital [8, 38].

^dIf one adds, for instance, the 2p-2h excitation class, the 0p-0h ground and 1h ionic states are no longer an eigenstate of \hat{H}_{atom} . In that case, the above analyses will require much more than reading and partitioning the wave function represented in the MF basis: one has to explicitly calculate these correlated states and then project $|\Psi(t)\rangle$ onto them.

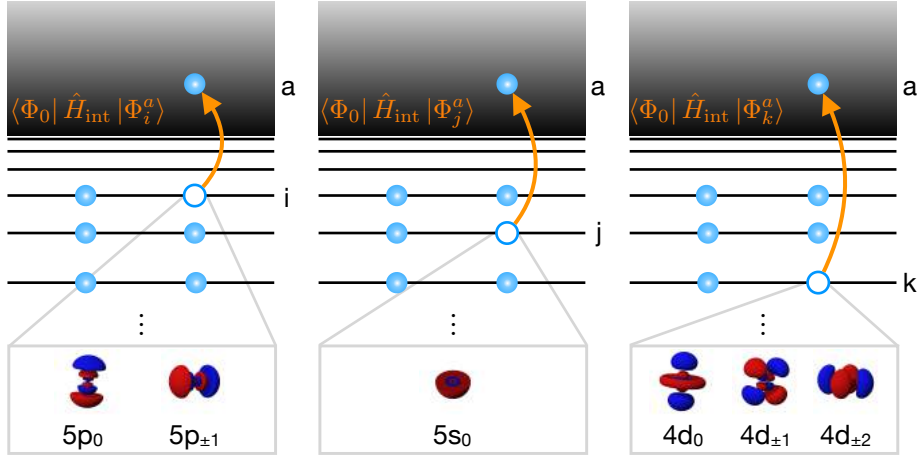


Figure 2.3. Schematic view of multichannel physics contained in TDCIS. A particle can be promoted from various occupied orbitals i in the neutral ground state through the light-matter interaction \hat{H}_{int} , leaving behind a photoion with $(N - 1)$ -electrons described by the IDM, generally in a mixed state. For the simulations of Xe in this thesis, activate channels include all the symmetry-adapted orbitals in and above the $4d$ subshell.

By tuning the range of i in the wave-function ansatz in Eq. (2.29), we can select different channels to participate in the ionization dynamics and identify the multiorbital effects of the overall process [45, 46, 50, 57].

Electronic correlation effects. In TDCIS, we distinguish between two different effects of the residual Coulomb interaction, depending on whether or not the residual interaction can change an ionic eigenstate [42]. If \hat{H}_1 does not couple $|\Phi_i^a\rangle$ to another state, it is called *intra-channel (Coulomb) coupling*; this is decided by the type of MF matrix elements $\langle \Phi_i^a | \hat{H}_1 | \Phi_i^b \rangle$. In this case, the role of \hat{H}_1 is to correct the short-range MF potential of the neutral atom; it gives the potential with a long-range Coulomb tail $-1/r$ as $r \rightarrow \infty$. The intrachannel potential is nonlocal and obviously depends on the detailed shape and alignment of the ion and have multipole contributions, which goes beyond the standard local central field used in SAE. On the other hand, if \hat{H}_1 leads to the mixing of $|\Phi_i^a\rangle$ with another state, it is called *interchannel (Coulomb) coupling*; this is decided by the type of matrix elements $\langle \Phi_i^a | \hat{H}_1 | \Phi_j^b \rangle$ with $i \neq j$. The change of the ionic state signified the simultaneous change of the state of the excited electron mediated by residual Coulomb interaction. This gives rise to the formation of a correlated, or entangled p-h pair. The difference between intrachannel and interchannel coupling is sketched in Fig. 2.4. As such, TDCIS includes another multielectron aspects

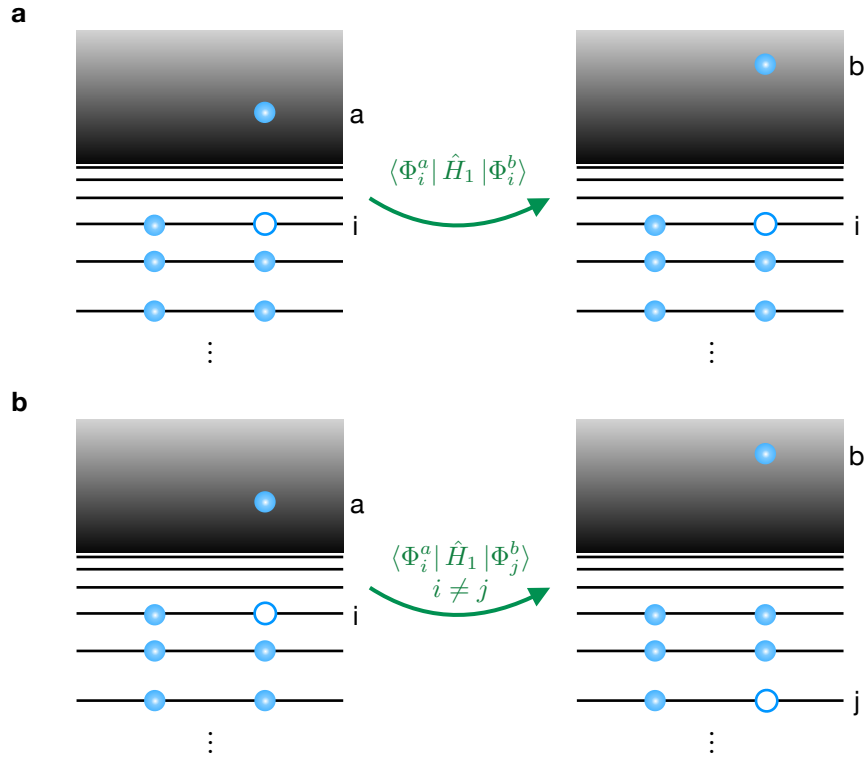


Figure 2.4. Schematic view of two different types of residual Coulomb interaction effects contained in TDCIS. **(a)** Intrachannel coupling: \hat{H}_1 does not change the state of the ion; it only corrects the asymptotic behavior of the effective potential seen by the photoelectron. **(a)** Interchannel coupling: \hat{H}_1 changes the state of the ion from i to j . In this case, the residual Coulomb interaction forms a pair of correlated photoion and photoelectron. This is the kind of electronic correlation effects included in TDCIS.

beyond the MF and SAE-type treatments, where the ion state is fixed, as represented by a frozen fixed potential.

In many occasions in this thesis, we compare the photoionization process in two different scenarios: the intrachannel and the full TDCIS models. In the intrachannel model, all the interchannel coupling matrix elements are manually set to zero. In so doing, we can identify how correlation effects influence the photoionization dynamics [50, 58].

Limitations of TDCIS. The advantages of TDCIS include its numerical efficiency, conceptual transparency, and a more technical point: size consistency. It represents a first step beyond SAE, and certainly warrants further improvement in order to have an even better quantita-

tive capacity and to be able to describe more complicated processes. This can be done in a systematic manner by enlarging the configuration space.

The limitations of TDCIS arise naturally from the constraint of the CIS space, which includes only the MF ground state and its singly excited configurations. As a result, processes that involve double or even higher excitation classes are absent. Examples are ground-state correlations (which could be reasonably neglected for noble-gas atoms), polarization response of the photoion (TDCIS acknowledges electronic correlation effects, but only allows the hole to hop between different orbitals; all the other electrons are frozen), multiple ionization or multiple excitation processes (such as shake-up, shake-off, and Auger decay).

2.3 Implementation aspects

This section presents some most important practical implementation aspects of the TDCIS in the currently available XCID package. We briefly explain how we solve TDSE or TISE directly on a numerical grid. For details please see Refs. [41, 42].

- *The mean-field procedure and discretization:* We adopt the restricted closed-shell HF procedure, which means that the spin orbitals that are only differed by spin are degenerate. From now on we only consider the spatial component of the orbital $\phi_p(\mathbf{r})$ (p refers to either an occupied or a virtual orbital). For atomic systems, it is conventional to take the spherical coordinates and exploit the symmetry using the spherical harmonics [44]:

$$\phi_p(\mathbf{r}) = \frac{u_{n_p, l_p}(r)}{r} Y_{l_p, m_p}(\theta, \phi), \quad (2.32)$$

where n_p is the principle quantum number, l_p is the orbital angular momentum quantum number, and m_p is the orbital magnetic quantum number. By representing $u_{n_p, l_p}(r)$ on a discretized radial numerical grid, we obtain a set of MF equations for the electron radial coordinate r and solve it in a self-consistent manner [44, 48].

- *Orbital representation and symmetries:* Each N -electron MF configuration is expressed in the orbital representation resulted from the HF procedure. Since we have to deal with a large amount of configurations, it is important to exploit symmetry as much as possible. Since our Hamiltonian is spin-free, the total spin is conserved and only the excited state with gerade parity can get populated [43]. Also, since we are interested in

the dynamics triggered by *linearly polarized light*, the total magnetic quantum number is conserved [45]. The 1p-1h configurations are symmetry-adapted configurations. An important consequence is that an ionization channel is now specified by a hole index [42]:

$$\phi_i \rightarrow n_i, l_i, \pm|m_i|, \quad (2.33)$$

where the spin quantum number is dropped since it is simply $\pm 1/2$.

- *Correction of occupied orbital energies:* Koopman's theorem gives reasonable estimation of electron binding energies. However, since binding energies are important for the description of ionization dynamics and enter the EOMs only as a parameter, their values may be adjusted by hand to match the experimental values [104, 117]. Although TDCIS does not explicitly include Auger decay, such an effect can be mimicked by adding a complex part (representing the Auger lifetime) to the occupied orbital energy [118].
- *Evaluation of matrix elements:* The matrix elements for the Hamiltonian and for any operator are evaluated using the Slater-Condon rules [109]. The angular part can be evaluated analytically using the angular-momentum-coupling algebra, i.e., the Clebsch-Gordan coefficients. The radial part needs to be done by carrying out numerical integration [44].
- *Solution of N -electron TISE:* The (time-dependent) Hamiltonian matrix is numerically diagonalized using the Arnoldi iteration using the ARPACK package. A random vector is used to launch the iteration [56].
- *Solution of N -electron TDSE:* The EOMs are a set of coupled ordinary differential equations, which can be solved using, e.g., Runge-Kutta-Fehlberg Method (RKF45).

2.4 Summary

The key messages of this chapter are summarized as follows:

- ◇ The time-dependent nonrelativistic N -electron Hamiltonian including exact two-electron Coulomb interaction is introduced to describe atomic photoionization in and between the two ionization limits. The light field is treated classically under the dipole approximation (Sec. 2.1).

- ◇ Photoionization dynamics is encapsulated by the N -electron TDSE; field-free or instantaneous field-dressed electronic structure is captured by the N -electron TISE.
- ◇ The N -electron TISE and TDSE can be solved using TDCIS, a wave-function–based *ab initio* electronic structure theory (Sec. 2.2).
- ◇ TDCIS includes two multielectron aspects of single photoionization processes: multi-channel physics (i.e., different ion states can be created) and essential electronic correlation effects (i.e., the photoion and the photoelectron can be coupled with each other through interchannel interaction).
- ◇ The current implementation of TDCIS, the XCID package, handles photoionization dynamics of a closed-shell atom in linearly polarized light fields (Sec. 2.3).

Chapter 3

Theory of resonances

After getting familiarized with the theoretical background of photoionization, we now zoom into the subset of photoionization dynamics that this thesis focuses on, namely that involves resonances. As discussed in Chapter 1, this thesis pays attention to resonances that arise due to the shape of a potential on a mean-field level. In this chapter, we introduce the theoretical description and the numerical solution of resonances, especially in terms of resonance states. As will be shown in the upcoming two application chapters, the concept of resonance states is of central importance.

Section 3.1 discusses the concept of resonances. Section 3.2 describes how to directly calculate resonance states using two NHQM techniques. Section 3.3 shortly explains the implementation of NHQM within TDCIS. Section 3.4 recapitulates this chapter.

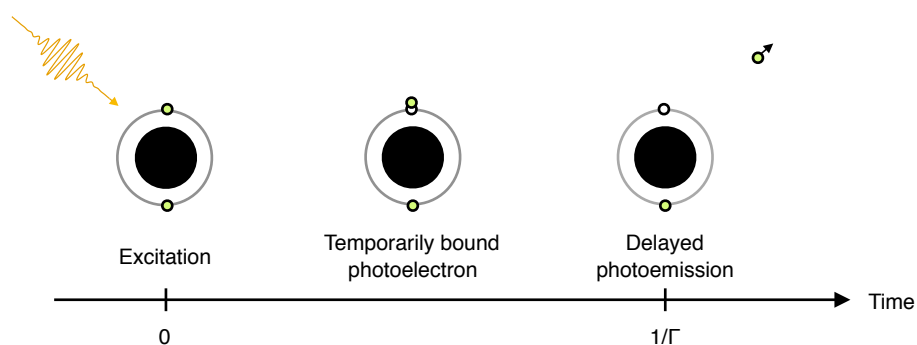


Figure 3.1. Topic of this chapter: theoretical description and numerical solution of resonance states. For detailed description of the figure see the caption of Fig. 1.6.

3.1 Theoretical description of resonances

Photoionization is essentially a scattering process, namely a half collision process. After light pumps energy into the electronic system, the composite excited system in the interaction region breaks up into products of photoion and photoelectron, with the latter eventually leaving to the asymptotic region.

In scattering theory, it is known that, at some energy above the breakup threshold, although the composite excited system has a sufficient energy to disintegrate into two or more subsystems, it can be held together for a while and undergoes a delayed fragmentation process (see Fig. 3.1). The system is said to hit a *resonance*: it is in a metastable state with a finite lifetime. Resonances are the most striking phenomenon in the whole range of scattering experiments [79].

Resonances are ubiquitous — radioactive decay of atomic nuclei, autoionization and Auger decay of atoms, transition states during chemical reactions, and Fano resonances in mesoscopic devices — just to name a few examples. Although resonances are commonly associated with structures in the scattering cross section, the notion of resonances is far more fundamental than that: cross section is nothing but *one possible manifestation* of the underlying resonance states, which bear a clear physical definition.

This section presents the basic notions of resonance states. A simple computational example is used to help develop an intuition on the resonance behavior and thus the general theory used to describe resonance states. The following content is largely based on the excellent book chapter of Klaiman and Gilary [78].

3.1.1 Wave-packet view of resonances

A most intuitive way to understand resonances is to study resonance wave-packet dynamics. Since this thesis focuses on potential-barrier effects during photoionization, we demonstrate the resonance dynamics using an example on shape-type resonances in a half-collision process (where the system is prepared in an localized excited state and then disintegrate).^a

^aResonances are commonly divided into two categories: shape-type and Feshbach-type resonances. As the name suggests, shape-type resonances arise due to the shape of a potential, where a particle can be trapped for a while and goes to the asymptotes via quantum tunneling. On the other hand, Feshbach-type resonances decay because of the coupling between a bound particle in one potential and continuum states of another potential. Note that this classification scheme is not unique and can depend on how one defines the reference potential.

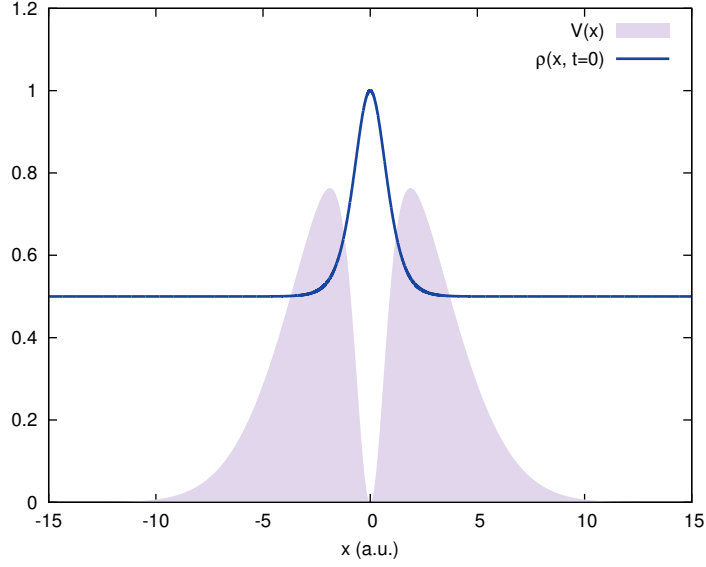


Figure 3.2. Distributions of the one-dimensional model potential $V(x)$ given in Eq. (3.1) and the initial density $|\psi(x, t = 0)|^2$ of the wave packet given in Eq. (3.3). The density is plotted with the energy of the wave packet, $\langle \hat{H} \rangle = 0.5$, as a baseline. This is the excitation energy of the first resonance supported by the potential. The short-range potential is roughly confined between $x = -10$ and $x = 10$.

The model Hamiltonian. Let us consider a one-dimensional, time-independent Hamiltonian of a particle [119]:

$$\hat{H} = -\frac{1}{2}\partial_x^2 + V(x), \quad (3.1)$$

where the short-range potential is given by

$$V(x) = \left(1 - \frac{1}{\cosh^2 x}\right) e^{-0.05x^2} \quad (3.2)$$

and is plotted in Fig. 3.2. This potential supports no bound state but only continuum states. It accommodates several resonances, with the lowest-lying one sitting at an excitation energy of $\Xi = 0.5$ [78].

Solution of TDSE. In order to study resonance phenomena, one has to venture into the continuum. Continuum states are highly delocalized and diffuse objects: unlike bound states, they are not squared integrable (L^2 -integrable) and can only be energy normalized [120]. To describe a quantum particle in the continuum and invoke the standard probabilistic interpretation, we take a continuous superposition of scattering states, i.e., a wave packet, and watch its time evolution to build up our physical intuition.

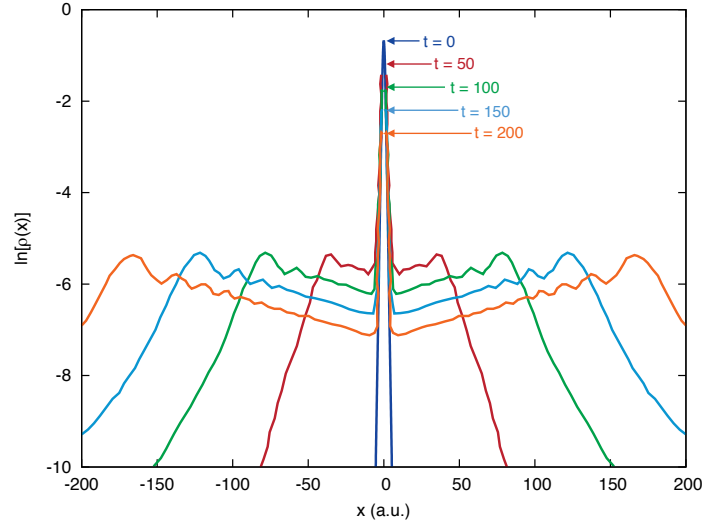


Figure 3.3. Snapshots of the wave-packet density at consecutive time intervals on a logarithmic scale. Part of the data is taken from Ref. [78]. The maximum density of the wave packet at a specific time is indicated by an arrow.

Based on an educated guess, we prepare an initial wave packet of the form [78]

$$\psi(x, t = 0) = \frac{1}{\sqrt{2} \cosh x}, \quad (3.3)$$

which has an energy expectation value of 0.5 and is localized inside the potential well (see the probability density $|\psi(x, t = 0)|^2$ in Fig. 3.2). The dynamics of the wave packet is obtained by solving the TDSE with the Hamiltonian specified in Eq. (3.1):

$$i\partial_t \psi(x, t) = \hat{H}\psi(x, t). \quad (3.4)$$

Properties of the resonance wavepacket. Figure 3.3 depicts the snapshots of the wave packet density $\rho(x, t) \equiv |\psi(x, t)|^2$ at different times on a logarithmic scale. For our analysis, it is helpful to analyze the dynamics into two spatial regions separately: (1) inside the interaction region, i.e., between the potential barriers, and (2) outside the interaction region, where the potential vanishes and the particle is no longer bound. Of course there is always some ambiguity in drawing this separation. However, as a rule of thumb, one can choose the classical turning points of the particle's motion [78]. The evolution of the wave packet density $\rho(x, t)$ *inside* the interaction region points to the following observations:

- a. *Spatial dependence:* the wave packet looks much like a bound state inside the barrier.

- b. *Temporal dependence*:** the density of the wave packet decays exponentially, as the peak amplitude drops at a constant speed.

This signifies that when on resonance, the particle is temporarily trapped by the potential well and leaks out of it by tunneling at a fixed, finite rate. When off resonance, the particle will leave the interaction much more faster [121].

If we move *outside* the interaction region, we have the following observations on $\rho(x, t)$ [78]:

- c. *Spatial dependence*:** the wave packet density diverges exponentially since it appears as a straight line on the logarithmic scale. Since the wave function of the wave packet is L^2 -integrable, the divergent behavior ceases at some point in space.
- d. *Temporal dependence I*:** we notice the formation of resonance wavefronts, which expand at a constant speed and correspond to a free-particle with a constant momentum.
- e. *Temporal dependence II*:** the density within the wavefronts decays exponentially at a fixed position.
- f. *Temporal dependence III*:** at the resonance wavefronts, the density remains as a constant value.

Obviously, the resonant wave-packet dynamics shows a dual nature/oxymoron of the resonance process: it is a bound state inside the potential barriers, while it behaves like a free-particle outside. If we focus in the interaction region, the wave packet behaves like a stationary state (in the sense that there is no redistribution of the density) but with a finite lifetime—it is in a quasistationary or metastable state.

Although the wave-packet dynamics befits our physical intuition, this approach has a few disadvantages: (1) the resonance phenomena have to be understood using a continuous superposition of continuum states, (2) we need to propagate the wave packet over time, (3) for a more complicated potential, we may not know how to prepare the initial wave packet, which may affect the dynamics we see, and (4) it becomes tricky if there are short-lived resonances with similar excitation energies. It would be much more convenient if we could describe resonances using one single eigenstate, just like what we do for understanding the standard bound-state dynamics. Our analysis has already given a hint on this: in the interaction region, resonance looks pretty much like a bound-state.

3.1.2 Eigenstate view of resonances

Motivated by the study of the decay of α particles in nuclear reactions, Siegert [122] was the first to realize that the entire resonance dynamics could be encapsulated using one single resonance eigenstate. Let us see how this can happen.

Solution of TISE with outgoing boundary conditions. The proposition of Siegert is that resonances can be obtained by solving the TISE

$$H\phi(x) = E\phi(x) \quad (3.5)$$

supplemented by *outgoing-wave boundary conditions* (BCs) [77]. The BCs in our one dimensional case read

$$\begin{aligned} (\partial_x - ik)\phi(x) &= 0, \quad x = L \\ (\partial_x + ik)\phi(x) &= 0, \quad x = -L, \end{aligned} \quad (3.6)$$

where $k = \sqrt{2E}$ and L refers to the boundaries of the interaction region. This set of BCs means that we seek for the solutions that have outgoing flux at the edges of the interaction region, i.e., $\phi(|x| \geq L) = e^{i|k|x}$. This is precisely the behavior we want to describe: after the particle leaves the potential, it moves past the boundaries and never returns.^b

For our simple case, the solution of the above TISE yields a discrete set of eigenvalues and eigenstates. Resonances correspond to the states with a complex-valued eigenenergy:

$$E_{\text{res}} = \Xi - i\frac{\Gamma}{2}, \quad \Xi, \Gamma \in \mathbb{R}^+, \quad (3.7)$$

which now bears the name of *Siegert energy*. Based on the the relation between E and k , we obtain a complex-valued wave vector

$$\begin{aligned} k &= |k|e^{-i\frac{\delta}{2}}, \quad |k| = \sqrt{2} \left(\Xi^2 + \frac{\Gamma^2}{4} \right)^{1/4}, \quad \delta = \tan^{-1} \frac{\Gamma}{2\Xi} \\ &\equiv k_{\text{re}} - ik_{\text{im}}. \end{aligned} \quad (3.8)$$

Note that, since k_{re} is a positive number, the eigenstate corresponds to an outgoing state of our interest.

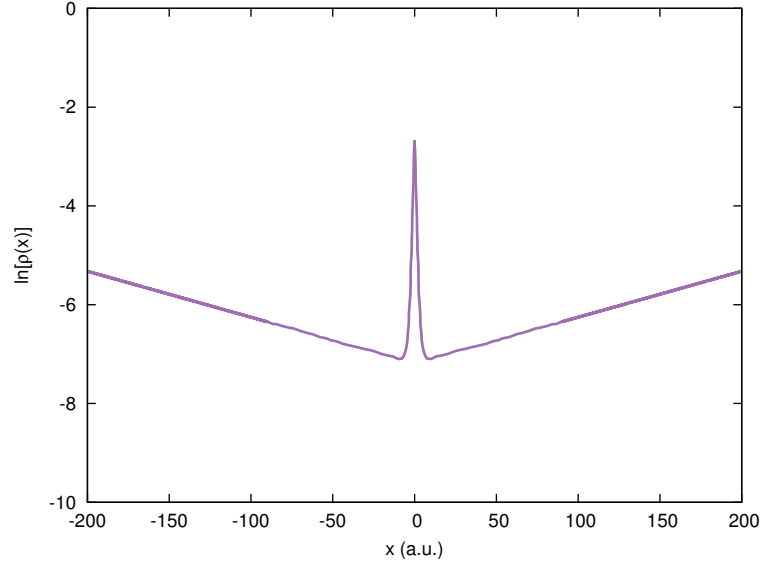


Figure 3.4. Density of the resonance eigenfunction on a logarithmic scale, which is obtained by solving the TISE with the outgoing wave BCs in Eq. (3.6).

Properties of the Siegert eigenstate. The eigensolution we found $\phi_{\text{res}}(x)$ generally has the name of Siegert state or Gamow vector. In order to understand the attributes of it, we examine the Siegert state by looking at the density $\rho(x) = |\phi_{\text{res}}(x)|^2$ as displayed in Fig. 3.4 on a logarithmic scale.

Since the Siegert state is an eigensolution of TISE, it has trivial time dependence $\psi_{\text{res}}(x, t) = e^{-i\Xi t - \frac{\Gamma}{2}t} \phi_{\text{res}}(x)$. Following the strategy of the time-dependent discussion in 3.1.1, we first study the properties of this state *inside* the interaction region:

- A. *Spatial dependence:* the density of the wave function $\phi_{\text{res}}(x)$ looks much like a bound state inside the barrier.
- B. *Temporal dependence:* the density of the wave function $\psi_{\text{res}}(x, t)$ decays exponentially at the rate of Γ . This means that the tunneling rate is Γ ; or equivalently, the lifetime of the Siegert state is $1/\Gamma$. The amplitude of the density, if plotted on a logarithmic scale, will decrease at a constant speed.

If we move *outside* the interaction region, we have the following observations:

^bIn the case of a three-dimensional long-range potential, e.g., Coulomb potential, the boundary conditions are imposed at $r \rightarrow \infty$ [77].

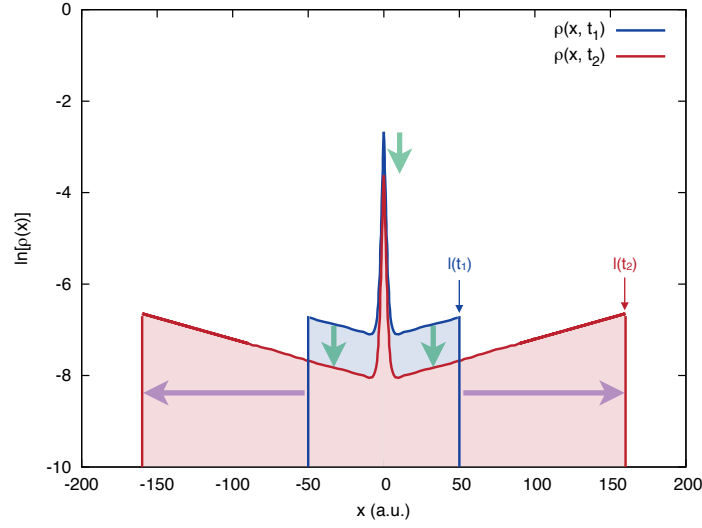


Figure 3.5. Expansion of the resonance wavefronts over time. The wave-function density remains as a constant at the resonance wavefronts. Inside the expanding volume (shaded area), there is a conservation of the particle number [123], although it is less obvious on the logarithmic scale.

- C. *Spatial dependence*: the density of $\phi_{\text{res}}(x)$ is a straight line on the log scale and diverges exponentially as $|x| \rightarrow \infty$ because of the factor $e^{k_{\text{im}}|x|}$ when $|x| > L$.
- D. *Temporal dependence I*: $\psi_{\text{res}}(x, t)$ corresponds to a free particle moving away from the interaction region at the speed of k_{re} . This can be seen from the factor $e^{ik_{\text{re}}|x|}$. Alternatively, we can also get the same conclusion from the continuity equation

$$j(|x| > L, t) = \text{Im}\{\psi_{\text{res}}^* \partial_x \psi_{\text{res}}\} = k_{\text{re}} \rho(x, t). \quad (3.9)$$

- E. *Temporal dependence II*: the density decays exponentially at a finite, fixed position. Since this temporal decay is balanced by the spatial divergence, as $t \rightarrow \infty$, the probability of observing the particle is accumulated at $|x| \rightarrow \infty$. Hence, notwithstanding the unsetting divergent behavior of the resonance wave function, it does have a physical interpretation.
- F. *Temporal dependence III*: Since the stream of the particle density moves away from the interaction region at a constant speed, let us consider a constantly expanding box with the boundaries $l(t) = k_{\text{re}} t$ [123]. The moving boundaries are sketched in Fig. 3.5. If we move together with the imaginary resonance wavefronts, we can prove that the density of $\psi_{\text{res}}(x, t)$ is a constant over time, just as the wave-packet case.

The proof is easy. Without loss of generality, we consider the side of $x > L$. Suppose at a time t_1 the boundary is at $l(t_1) \equiv l_1$, and the resonance wave function density is $\rho(t_1, l_1)$. Then, at a later time $t_2 = (t_1 + \Delta t)$, the boundary is at $l(t_2) = (l_1 + k_{\text{re}}\Delta t)$. This gives the density

$$\rho(t_2, l_2) = \rho(t_1, l_1)e^{-\Gamma\Delta t}e^{2k_{\text{re}}k_{\text{im}}\Delta t} = \rho(t_1, l_1). \quad (3.10)$$

In above, we have used the relation in Eq. (3.8), i.e.,

$$2k_{\text{re}}k_{\text{im}} = 2|k|^2 \cos \frac{\phi}{2} \sin \frac{\phi}{2} = |k|^2 \sin \phi = \frac{|E|}{2} \sin \phi = \Gamma. \quad (3.11)$$

Furthermore, one can show that, within these expanding wavefronts, the integral of the particle density is a constant, finite value, meaning that the particle number in the resonance state is conserved over time [123].

By comparing the above time-independent results **A.-F.** to the previous time-dependent results **a.-f.** in 3.1.1, we note that there is a solid one-to-to correspondence. Hence, this single Siegert eigenstate can be used to capture the entire resonance behavior previously represented by a resonance wave packet, and, as nicely put in Ref. [78], is a real flesh-and-blood being.

Advantages of the time-independent approach. Generally speaking, by solving TISE with outgoing BCs [see Eq. (3.6)], one can get resonance eigenstates which are identified by their discrete, complex eigenenergies [see Eq. (3.7)]. These states are metastable states that live for a finite duration: they represent a localized compound species that decays away by emitting a particle to asymptotes, in the case of shape resonances, via tunneling. This slows down the breakup process in comparison to the case without any trapping.

The concept of resonance eigenstates greatly facilitates our understanding of the resonance behavior. It circumvents the conceptual difficulty in dealing with dynamics happening in the continuous part of the energy spectrum—the inability to correlate the physical phenomena to a single (or a few) eigenstates. On the computational side, this stationary-state approach is attractive, as it can be achieved by solving once the TISE and avoids the propagation of the wave packet. In addition, the Siegert energies extracted from the wave-packet dynamics often depend on how one prepares the initial states. Finally, the time-dependent approach gets increasingly difficult when dealing with multiple, short-lived resonances.

Additional remarks on the resonance states. Before ending this section, we point a few remarks on the resonance states that have not been addressed in our previous discussion.

- *On the hermiticity of the Hamiltonian:* The physical Hamiltonian we are familiar with is a hermitian operator, which has real energy eigenvalues. Since Siegert energies are complex numbers, the Hamiltonian giving birth to them is apparently non-Hermitian. In general, when dealing with resonance states, one need to invoke non-Hermitian quantum mechanics (NHQM), where various familiar features of the standard quantum mechanics (QM) get modified.

The Hermiticity of an operator depends on the boundary conditions of the function it is allowed to act on. In the standard Hermitian QM all the states in this physical Hilbert states take on a finite value, i.e., they are bounded functions. Since we impose the outgoing BCs and searching for asymptotically divergent resonance states, the Hamiltonian is no longer hermitian; while the resonance states do not lie in the hermitian domain of the Hamiltonian, they are elements in the non-Hermitian domain of a generalized Hilbert space.

- *On the connection to the S-matrix and scattering cross section:* In this section, we studied the wave-packet dynamics in hermitian QM to understand resonance behavior. This can equally be achieved using stationary scattering theory.

The important quantity used to study resonances is the S-matrix, which is defined as the ratio between the amplitude of the outgoing plane wave and that of the incoming wave. On resonance, only outgoing waves exist and the incoming waves vanish, so S-matrix diverges. It can be proved that the Siegert states correspond to poles of the S-matrix [77].

Because of this connection, resonance poles cause rapid variation, or resonance-like structure, in the scattering cross section. Typically under the approximation of isolated, narrow resonances with smooth background, resonance states give rise to Breit-Wigner profile [79]. We should emphasize here again that spectroscopic features are only one way to reveal a resonance state, which is an intrinsic property of a given Hamiltonian.

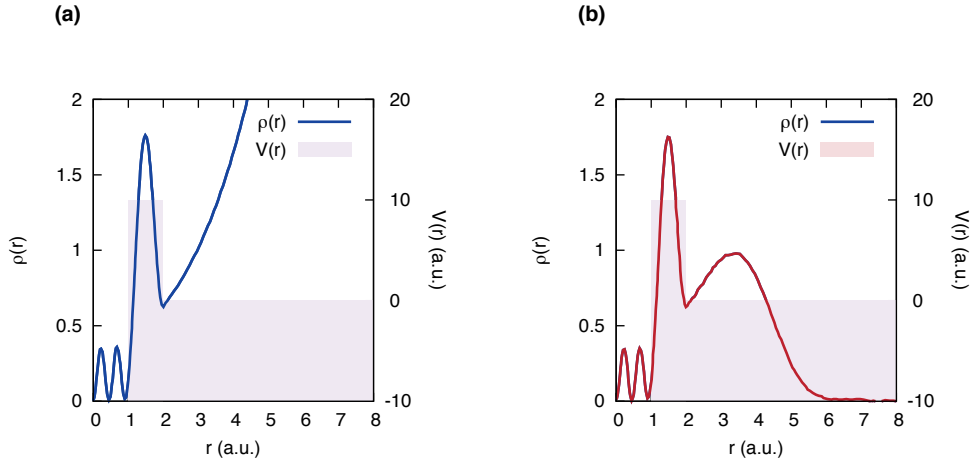


Figure 3.6. Comparison of the resonance wave-function radial density of **(a)** a model Hamiltonian $\hat{H} = -\frac{\nabla^2}{2} + V(r)$ and **(b)** the Hamiltonian after a suitable mathematical transformation \hat{H}' . The transformation is introduced to tame the asymptotic divergent behavior of a resonance state. The spherically symmetric potential $V(r)$ is also plotted. Here, the transformation is based on adding a CAP to the original Hamiltonian. The data are taken from Ref. [80].

3.2 Direct calculation of resonance states

As shown in the previous section, resonances are fundamental quantum states of the Hamiltonian. They correspond to the solution of TISE

$$\hat{H}\Phi_{res} = E_{res}\Phi_{res} \quad (3.12)$$

with a complex Siegert energy. Each Siegert state represents a localized state in the inner region that decays away by emitting a particle into the asymptotic region.

However, numerical solution of such out-going, divergent states is not a matter of routines. The main reasons are: (1) numerical inefficiency arising from directly imposing the boundary conditions, which results in a nonlinear eigenvalue problem that needs to be solved iteratively [124], and (2) the asymptotic divergent behavior of the Siegert states, which cannot be directly represented on a numerical spatial grid using a bounded basis set.^c

The first step towards an appropriate reconciliation of the above-mentioned problems is to force the resonance wavefunctions to be square integrable by carrying out a suitable

^cNote that Siegert pseudostate approach has been proposed to make the TISE approach easier to be implemented on a computer [125].

mathematical transformation. As shown below, there are various different, although in fact mutually equivalent, ways in which such a transformation can be introduced. Each transformation of this kind converts the original exponentially divergent resonance wavefunction into a bounded normalizable function which can be considered as a part of generalized Hilbert space. Fig. 3.6 shows a comparison between the resonance wave function of an original Hamiltonian \hat{H} and that of a transformed Hamiltonian \hat{H}' .

This section presents how to directly calculate square-integrable resonance states within the framework of nonhermitian quantum mechanics such that (1) the resonance states are amenable to standard bound-state treatments, and (2) they satisfy our feeling that resonances are localized. The methodology is based on two techniques, namely *complex scaling* and the use of *complex absorbing potentials* (CAPs). Therefore, resonance states can be obtained by numerical diagonalization of a modified Hamiltonian using bounded basis set.

3.2.1 Method of complex scaling

The first method is *complex scaling* (CS), also called complex-coordinate or complex rotation method [77, 121, 126, 127]. This method was conceived by Hartree in the 1940s (see Ref. [128] and the references therein), and was proposed and analyzed with rigorous mathematical proofs by Balslev and Combes [129] and Simon [130] in the 1970s.

Idea of complex scaling. The idea of complex scaling is to perform an analytical continuation of the radial coordinate of each particle such that it is rotated into a complex coordinate plane [126]:

$$r \rightarrow re^{i\theta} \equiv \rho(r), \quad (3.13)$$

where θ specifies the rotation angle. For a many-particle system, $\vec{r} = (\vec{r}_1, \vec{r}_2, \dots, \vec{r}_n)$. The transformation defined in Eq. (3.13) is equivalent to a unitary similarity transformation operator given by^d

$$\hat{S} \equiv e^{i\theta r \partial_r}. \quad (3.14)$$

^dSimilarity transformation is a mathematical transformation that stretches the lengths of vectors but does not change the relative angle between any two vectors.

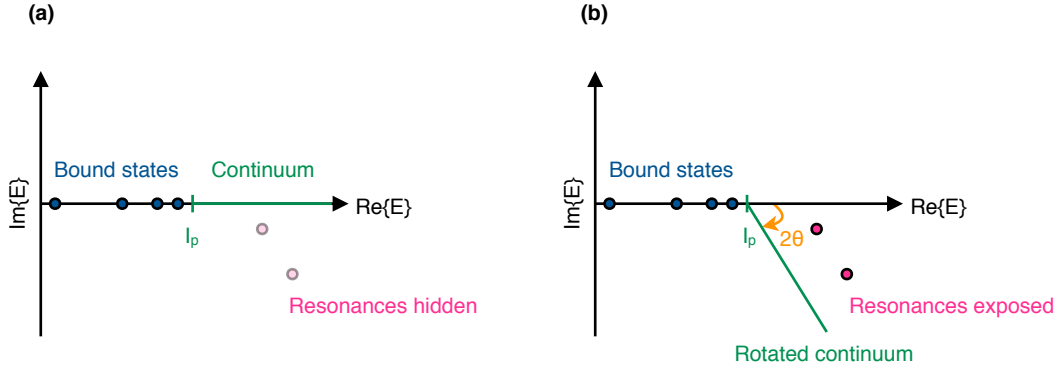


Figure 3.7. Comparison of the energy spectrum of (a) a Hermitian Hamiltonian \hat{H} and (b) a complex-scaled non-Hermitian Hamiltonian \hat{H}^θ . The horizontal axis represents the real part of an eigenenergy, and the vertical axis represents the imaginary part of an eigenenergy. The position of the ionization threshold is indicated by I_p . After complex scaling, the bound states (blue filled circles) remain on the real energy axis, the continuum (green line) is rotated clockwise by twice the scaling angle, 2θ , and resonance states (pink filled circles) become eigenstates situated above the rotated continuum. Once a resonance is exposed, its position is independent of θ .

The transformed TISE then reads

$$(\hat{S}\hat{H}\hat{S}^{-1})(\hat{S}\Psi) = E(\hat{S}\Psi), \quad (3.15)$$

$$\hat{H}^\theta\Psi^\theta = E\Psi^\theta. \quad (3.16)$$

Spectrum of the scaled Hamiltonian. Clearly, the transformed Hamiltonian \hat{H}^θ is non-Hermitian due to the introduction of the complex coordinate. The eigensolutions of \hat{H}^θ generally have a set of complex energy eigenvalues, which is called the complex energy spectrum of \hat{H}^θ . The distribution of the complex energy spectrum of \hat{H}^θ and the correspondence to the energy spectrum of \hat{H} follow the *Balslev-Combes theorem* [77, 126, 129]. In below, we show how to different types of states react to the complex scaling and how to identify them accordingly. In particular, we demonstrate that this transformation eliminates the divergent behavior of Siegert states and they become an eigensolution of \hat{H}^θ .

The comparison between the energy spectrum of the original Hermitian Hamiltonian \hat{H} and that of the scaled non-Hermitian Hamiltonian \hat{H}^θ is shown in Fig. 3.7. Note that when using a finite-valued bounded basis functions to diagonalize the Hamiltonian, an eigenstate must be bounded functions. Here, for simplicity, let us consider a one-particle case and assume the ionization threshold $I_p = 0$ (the spectral properties of the scaled Hamiltonian are

the same for an N -electron Coulomb system [126]).

- *Bound states*: they remain as an eigenstate of \hat{H}^θ ; their energy eigenvalues are invariant and stay in the real energy axes after complex scaling.

The reason can be understood as follows. For a bound state of \hat{H} , the asymptotic behavior $\Psi_{\text{bs}}(r \rightarrow \infty) \propto e^{-r}/r$. After the transformation, the asymptotic behavior becomes $\Psi_{\text{bs}}^\theta(r \rightarrow \infty) \propto e^{-re^{i\theta}} = \exp(-r \cos \theta + i \sin \theta)$. Hence, as long as $\theta < \pi/2$, $\Psi_{\text{bs}}^\theta(r) \rightarrow 0$; Ψ_{bs}^θ is L^2 -integrable and is an eigenstate of \hat{H}^θ .

- *Continuum states*: the transformed Hamiltonian has continuum that is rotated from the real energy axis clockwise into the complex energy plane by an angle of 2θ .

The reason can be understood as follows. For a continuum state of \hat{H} , the asymptotic behavior $\Psi_{\text{cs}} \propto e^{+ikr}/r$ and e^{-ikr}/r , where $k = \sqrt{2E}$. After the transformation, one of the exponentials will explode asymptotically, violating the requirement of everywhere finite wave functions. Hence, to preserve the bounded asymptotic behavior as $r \rightarrow re^{i\theta}$, we must simultaneously take $k \rightarrow ke^{i\theta}$. This means that the continuum states of \hat{H}^θ have energy $E_{\text{cs}}^\theta = E_{\text{cs}} e^{-i2\theta}$. The ionization threshold is invariant.

- *Resonance states*: the transformed Hamiltonian shows complex, discrete eigenvalues in the fourth quadrant of the complex energy plane, which are associated with resonances.

The reason can be understood as follows. For the unscaled Hamiltonian, the asymptotic behavior of a resonance state $\Psi_{\text{res}}(r \rightarrow \infty) \propto e^{ikr}/r$, where the complex k is defined in Eq. (3.8). Since the resonance wave function is divergent, it is not an eigenstate of \hat{H} represented using a bounded basis set; the resonance is “hidden” in the energy spectrum of \hat{H} . After the transformation, the asymptotic behavior of a resonance $\Psi_{\text{res}}^\theta(r \rightarrow \infty) \propto \exp(i|k|r \cos(\theta - \delta/2) - i|k|r \sin(\theta - \delta/2))$. In the range of $\frac{\delta}{2} < \theta < \pi + \frac{\delta}{2}$, where $\delta = \tan^{-1} \frac{\Gamma}{2E}$, the asymptotic resonance wave function approaches zero and, thus, is an L^2 -integrable eigenstate of the scaled Hamiltonian. There is a smallest, critical angle $\delta = \tan^{-1} \frac{\Gamma}{2E}$ to “expose” or to tame the divergent behavior of the resonance, which represents the angle of the Siegert energy in the complex energy plane (in other words, we can also say that the continuum states have to be rotated far enough into the complex plane).

Note that, in passing, we acquire the constraint of the rotation angle: $\delta/2 < \theta < \pi/2$; the lower limit comes from the requirement to eliminate the divergent behavior of a resonance, while the upper limit comes from the requirement of not to affect the asymptotic behavior as

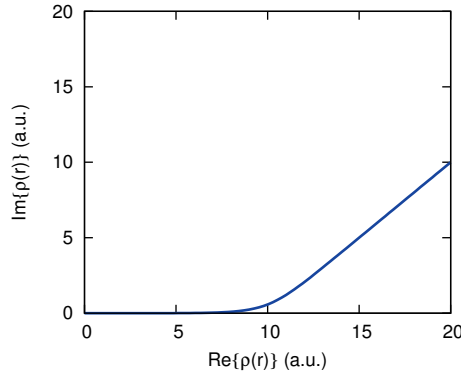


Figure 3.8. The form of SES used in this thesis. In this case, $\theta = \pi/4$, $\lambda = 1$, and $r_0 = 10$.

well as the energies of the bound states. Once the resonance is exposed, the Siegert energy is independent of θ provided the basis set used is complete.

In the presence of light-matter interaction, the spectral features of the scaled Hamiltonian remain as the same as what we have discussed above. Because the length-gauge interaction Hamiltonian reads $H_{\text{int}}(t) = -\mathbf{E}(t) \cdot \mathbf{r}$ (see Sec. 2.1.2), it may appear that the asymptotic behavior of quantum states no longer follows the form e^{ikr}/r . However, by going to another frame of light-matter interaction, namely the Kramers-Henneberger (KH) frame, the Hamiltonian representing the instantaneous light-matter interaction is encapsulated by a time-dependent, spatially confined dressed Coulomb potential [28]. There, again, we recover the asymptotic behavior of e^{ikr}/r , so the spectrum of the instantaneous field-included Hamiltonian is exactly the same as that of the field-free Hamiltonian as discussed before. Since the unitary transformation has no impact on the set of eigensolutions (if a complete basis set is used), the properties obtained in the KH frame is the same as those in other frames [121].^e

Variations of complex scaling. The original form of complex scaling puts a strong restriction on the potential, that it has to be dilatation analytical (i.e., it can be written down analytically so that we can get infinite order of its derivatives). This can be proven to be true for a short-range or purely Coulomb potential, even in the many-body case [129, 130]. However, it is a nontrivial question as to whether complex scaling works for other potentials, such as HF, HFS, or our intrachannel potential. In order to bypass the requirement of dilatation analyticity of

^eIf one would like to explicitly include the time dependence of the interaction Hamiltonian, one would have to combine KH transformation with Floquet theory. Again, the same conclusion could be obtained in that way [121].

the potential, we can start to scale the coordinate outside the interaction region, where it is either zero or have well known asymptotic form. This is the idea of *exterior complex scaling* (ECS), as originally proposed by Simon [131].

A further improvement is the *smooth exterior complex scaling* (SES), first proposed by Rom, Engdahl, and Moiseyev [132]. While ECS carries out the rotation into the complex coordinate plane abruptly at some radius r_0 , which leads to the presence of a delta function potential term in the scaled Hamiltonian and some numerical difficulty [77], SES suggests to perform the scaling smoothly, starting around r_0 . In this thesis, we will use the SES following the path of Moiseyev [133] in the form of Karlsson [134] to rotate the particle's radial coordinate into the complex plane

$$\rho(r) = r + (e^{i\theta} - 1) \left[r + \lambda \ln \left(\frac{1 + e^{(r_0-r)/\lambda}}{1 + e^{r_0/\lambda}} \right) \right], \quad (3.17)$$

where θ is the scaling angle, λ is the smoothing parameter, and r_0 is where we start to rotate into the complex coordinate plane. This SES path is shown in Fig. 3.8. As a rule of thumb, the scaling parameters, in particular θ and r_0 are chosen such that the continuum is rotated enough for the resonances to show up, but at the same time keep all the bound state energies remain on the real energy axis.

3.2.2 Method of complex absorbing potentials

Idea of using CAPs. The idea of the usage of CAPs is very intuitive: if the resonance wave function diverges asymptotically, why don't we just add a complex potential outside the interaction region to change its behavior? This leads to a modified Hamiltonian of the following form [80, 135]:

$$\hat{H}^\eta = \hat{H} - i\eta W(r), \quad (3.18)$$

where $\eta \in R^+$ represents the strength of the CAP, positive-definite function $W(r)$ is a potential that is placed far enough from the interaction region. The form of the CAP used in this thesis reads [44]

$$W(r) = h(r - r_0) (r - r_0)^2, \quad (3.19)$$

where $h(x)$ is the Heaviside step function, and r is the distance from the origin. This CAP is zero until a radius r_0 , after which it is a quadratically growing potential.

The effect of adding a CAP can be best understood in a time-dependent manner, via the continuity equation [80]. Let us write down the TDSE for a particle with a time-independent Hamiltonian in three dimensional space in the presence of a CAP:

$$i\partial_t\psi(\mathbf{r}, t) = \left[-\frac{1}{2}\nabla^2 + V(\mathbf{r}) - i\eta W(\mathbf{r}) \right] \psi(\mathbf{r}, t). \quad (3.20)$$

We are interested in the time evolution of the probability density $\rho(\mathbf{r}, t) = \psi^*(\mathbf{r}, t)\psi(\mathbf{r}, t)$:

$$\begin{aligned} \partial_t\rho(\mathbf{r}, t) &= \psi^*(\mathbf{r}, t)\partial_t\psi(\mathbf{r}, t) + \psi(\mathbf{r}, t)\partial_t\psi^*(\mathbf{r}, t) \\ &= \psi^* \left(\frac{i}{2}\nabla^2 - iV - \eta W \right) \psi + \psi \left(-\frac{i}{2}\nabla^2 + iV - \eta W \right) \psi^* \\ &= -\nabla \cdot \mathbf{j}(\mathbf{r}, t) - 2\eta W(\mathbf{r})\rho(\mathbf{r}, t). \end{aligned} \quad (3.21)$$

In above, we have used TDSE and its complex conjugate to obtain $\partial_t\psi$ and $\partial_t\psi^*$; the probability flux density is defined by $\mathbf{j}(\mathbf{r}, t) = -\frac{i}{2}(\psi^*\nabla\psi - \psi\nabla\psi^*)$. In the absence of the CAP, we recover the standard continuity equation $\partial_t\rho(\mathbf{r}, t) + \nabla \cdot \mathbf{j}(\mathbf{r}, t) = 0$, which signifies the conservation of the norm of the wave function. In the presence of the CAP, the term $-2\eta W(\mathbf{r})\rho(\mathbf{r}, t)$ drains away the probability provided the product ηW is positive.

Connection and comparison to complex scaling. When adding a CAP, the modified Hamiltonian is nonhermitian and generally allows for complex energy eigenvalues. Since the absorption typically starts far away from the interaction region, the bound-state spectrum of \hat{H}^η is the same as that of \hat{H} . What about the states that lie in the continuous spectrum of \hat{H}^η ? How do they behave? And are there any states corresponding to the resonances we are looking for?

The answer to the above questions have been studied in a series of papers of Riss and Meyer [136–139]. They have rigorously shown that, as long as W satisfies a few general requirements, \hat{H}^η defines a analytic continuation of \hat{H} at the limit of $\eta \rightarrow 0^+$. Under this condition, the spectrum converged to what has been shown in Fig. 3.7: bound states remain on the real energy axis, continuum states are rotated into the lower complex plane, and resonances are exposed poles situated above the rotated continuum. Obviously, whether a resonance can be exposed depends on how well the CAP can modify the asymptotic divergent behavior: when adding a CAP to an Hamiltonian, the tail of the resonance wave function that corresponds to an outgoing particle will be absorbed and, when the absorption is effective enough, it becomes a squared integrable function.

Note that our discussion on the spectrum of \hat{H}^η underlies the disadvantage of CAPs: despite of the ease for implementation, since in practice η is never zero, one has to run a few

calculation and track the positions of the resonances along their η trajectories. The Siegert energies are typically identified as the stable points along the trajectories [80]. Whereas complex scaling has rigorous mathematical foundation, the use of CAPs is more of an empirical basis.

In a reversed way, Moiseyev has proven that SES is fully equivalent to adding an effective complex absorbing potential [77, 121]:

$$\hat{H}^{\theta, \text{SES}} = \hat{H} + \hat{V}_{\text{RF-CAP}}. \quad (3.22)$$

The reflection-free complex absorbing potential $\hat{V}_{\text{RF-CAP}}$ is a complex-valued, nonlocal potential. While the choice of the form of a standard CAP relies on trial and error and can be problem-dependent, the form of $\hat{V}_{\text{RF-CAP}}$ requires less optimization: it can be derived from the potential and kinetic energy operators and is energy-independent.

3.2.3 Fundamentals of nonhermitian quantum mechanics

After applying complex scaling or adding a CAP to the original Hamiltonian, we obtain a Hamiltonian that is non-Hermitian. We have discussed how to identify different types of eigenstates of the resulting Hamiltonian. But questions remain. For example, do the eigen-solutions of the modified Hamiltonian form a complete and orthogonal basis set? In particular, this aspect is important for the calculation of matrix elements and the development of perturbation theory in the framework of NHQM. Also, how do we take inner products or define norm to extract information of these eigenstates? Here, we discuss some basic aspects of NHQM. Due to the non-Hermiticity of the Hamiltonian, the way we make use of the eigenstates deviates, in several respects, from the familiar way in the conventional Hermitian quantum mechanics.

Left and right eigenstates. An important technical consequence arising from the non-Hermiticity of the modified Hamiltonian is that the bra eigenstate of an arbitrary Hamiltonian \hat{H} , $\langle \Phi_i |$, is not anymore the Hermitian transpose of the ket eigenstate $|\Phi_i\rangle \equiv |\Phi_i\rangle$. That is, $\langle \Phi_i | \neq \langle \Phi_i | = |\Phi_i\rangle^\dagger$. In below, we review the concepts of bra and ket states.

A ket or a right eigenstate $|\Phi_i\rangle \equiv |\Phi_i\rangle$ is a eigenvector of \hat{H} satisfying [77, 121]

$$\hat{H}|\Phi_i\rangle = E_i|\Phi_i\rangle. \quad (3.23)$$

Let us consider a matrix representation of the above equation (typically in the coordinate representation),

$$\mathbf{H}\Phi_i^R = E_i\Phi_i^R, \quad (3.24)$$

where Φ_i^R is a column vector.

On the other hand, a *bra* or a *left eigenstate* $(\Phi_j|$ satisfies the following equation [77, 121]

$$(\Phi_j|\hat{H} = E_j(\Phi_j|, \quad (3.25)$$

which in the matrix form can be written as

$$(\Phi_j^L)^T \mathbf{H} = E_j(\Phi_j^L)^T \stackrel{T}{\Rightarrow} \mathbf{H}^T \Phi_j^L = E_j \Phi_j^L \quad (3.26)$$

where $(\Phi_j^L)^T$ is a row vector, and T denotes the transpose of a matrix. Note that in above we have used the fact that the eigenvalues of \mathbf{H} are identical to the eigenvalues of \mathbf{H}^T .

By comparing Eq. (3.24) to Eq. (3.26), we find that there is a one-to-one correspondence between a right eigenvector and a left eigenvector via a common eigenvalue. That is, a given E_i decides a pair of vectors: Φ_i^R and its dual vector $(\Phi_i^L)^T$. In the most general case in NHQM, the left eigenstates need to be explicitly calculated. Before we discuss such a general case, let us first consider two special cases, in which there is a simple mapping from a ket eigenvector to its dual vector.

- When \mathbf{H} is a *hermitian* matrix, i.e., when $\mathbf{H}^T = \mathbf{H}^*$ or $\mathbf{H} = \mathbf{H}^\dagger$: under this condition, by comparing Eqs. (3.24) and (3.26), the left eigenvector is simply the conjugate transpose of the right eigenvector, $(\Phi_i^L)^T = (\Phi_i^R)^{*T} = (\Phi_i^R)^\dagger$. This gives $(\Phi_i| = \langle \Phi_i| \equiv |\Phi_i\rangle^\dagger$, which is what we are familiar with in standard quantum mechanics.
- When \mathbf{H} is a *complex symmetric* matrix, i.e., when $\mathbf{H}^T = \mathbf{H}$: under this condition, by comparing Eqs. (3.24) and (3.26), the left eigenvector is simply the transpose of the right eigenvector, $(\Phi_i^L)^T = (\Phi_i^R)^T$, or, in an abstract form, $(\Phi_i| = |\Phi_i\rangle^T$. This is the case, e.g., when the Hamiltonian matrix becomes complex only upon complex scaling or adding a CAP, and real basis functions are used to represent \mathbf{H} .

Orthogonality and completeness of the eigenstates. Why do we bother to discuss right and left eigenvectors at all? First of all, we use them to define a complete and orthonormal basis set of a general Hamiltonian matrix. To see how this happens, let \mathbf{X}_R be the matrix

formed by columns from the right eigenvectors Φ_i^R , X_L be the matrix formed by rows from the left eigenvectors $(\Phi_i^L)^T$, and $\text{diag}(E_1, E_2, \dots, E_n)$ be the diagonal matrix formed by the eigenvalues [140]. Then Eqs. (3.24) and (3.26) can be recast into

$$H X_R = X_R \text{diag}(E_1, \dots, E_n), \quad (3.27)$$

$$X_L H = \text{diag}(E_1, \dots, E_n) X_L. \quad (3.28)$$

Multiplying Eq. (3.27) on the left by X_L , Eq. (3.28) on the right by X_R and then subtracting the two gives

$$(X_L X_R) \text{diag}(E_1, \dots, E_n) = \text{diag}(E_1, \dots, E_n) (X_L X_R). \quad (3.29)$$

This says that the matrix of inner products of the left and right eigenvectors commutes with the diagonal matrix of eigenvalues. But the only matrices that commute with a diagonal matrix of *distinct elements* are themselves diagonal.^f Thus, if the eigenvalues are nondegenerate, each left eigenvector is orthogonal to all right eigenvectors except its corresponding one, and vice versa. By choice of normalization, the dot products of corresponding left and right eigenvectors can always be made unity for any matrix with nondegenerate eigenvalues. This brings about the *completeness* relationship

$$X_L X_R = \mathbb{1} \quad \text{or} \quad \sum |\Phi_j\rangle \langle \Phi_j| = \hat{1} \quad (3.30)$$

and the *orthonormality* relationship

$$(\Phi_j^L)^T \Phi_i^R = \delta_{i,j} \quad \text{or} \quad \langle \Phi_i | \Phi_j \rangle = \delta_{i,j}. \quad (3.31)$$

The orthonormal complete set of \hat{H} is important for the formulation of perturbation theory and variational principle [77] as well as the evaluation of various matrix elements [44] of a general Hamiltonian. Also, note that Eq. (3.30) provides a general way to compute the left eigenvectors provided the right eigenvectors are known, i.e., $X_L = X_R^{-1}$, if H is neither a Hermitian nor a complex symmetric matrix.

Inner product: contraction of the left and right states. Inner product is formed by a contraction operation between a pair of vectors that yields a number: one in the vector space of \mathbb{V} , which is the Hilbert space formed by all the key eigenstates $\{|\Phi_i\rangle\}$, and another one in

^fIn very rare situations when two or more eigenvalues and eigenfunctions of \hat{H} coalesce, i.e., degenerate, please refer to a detailed discussion in other formulation Ref. [77].

the dual vector space $\tilde{\mathbb{V}}$, which is the Hilbert space formed by all the bra eigenstates $\{(\Phi_j|)\}$. This defines the *generalized c-product* which has the following bilinear form [77]

$$(\Psi'|, |\Psi\rangle), \quad (\Psi'| \in \tilde{\mathbb{V}}, |\Psi\rangle \in \mathbb{V}. \quad (3.32)$$

When \hat{H} is complex symmetric, the above inner product is called the *symmetric inner product*. Note that, for any state $|\Psi\rangle = \sum a_i |\Phi_i\rangle$, the generalized *c-norm* is generally a complex number. For example, let us consider the case where the Hamiltonian is complex and symmetric, then $\langle\Psi| = \sum a_i \langle\Phi_i|$, and then $\langle\Psi|\Psi\rangle = \sum a_i^2 \in \mathbb{C}$.

The inner product defined in Eq. (3.32) should be distinguished from the *Hermitian inner product*

$$\langle\Psi'|, |\Psi\rangle), \quad \langle\Psi'| \in \mathbb{V}^*, |\Psi\rangle \in \mathbb{V}, \quad (3.33)$$

where \mathbb{V}^* is formed by the Hermitian conjugates of all the key eigenstates as in conventional quantum mechanics. When the Hamiltonian is non-hermitian, the Hermitian norm $\langle\Psi|\Psi\rangle = \sum_{i,j} a_i^* a_j \langle\Phi_i|\Phi_j\rangle$, where $\langle\Phi_i|\Phi_j\rangle \neq \delta_{i,j}$ and is called the overlap matrix element between the two states.

As a rule of thumb, whenever one needs to evoke the orthogonality relationship among the eigenstates of a non-Hermitian Hamiltonian, the *c-product* defined in Eq. (3.32) must be used [77]. On the other hand, when calculating expectation values of an observable, we use the Hermitian inner product such that the expectation value is a real number [44, 48].

3.3 Implementation aspects

In below, we explain how to incorporate SES and CAPs into the framework of TDCIS.

First, we note that these two techniques not only can be used to calculate resonances by solving TISE, but can also be used as an *absorber* when solving TDSE. When dealing with ionization dynamics, one utilizes a finite numerical box. Thus, when the wave packet reaches the edges of the box, it can get reflected and lead to numerical artifacts. The function of SES and CAPs in wave-packet propagation is thus to avoid such artificial reflections by absorbing the outgoing flux arriving in the exterior region ($r > r_0$) [44] [see Eq. (3.21)]. As a result, whether we solve TISE or TDSE, we have a non-Hermitian Hamiltonian to deal with.

The non-Hermiticity leads to the following modifications of the TDCIS theory introduced in Chapter 2:

- *Modified mean-field procedure:* The effect of SES or CAPs are incorporated in the MF procedure. After separating out the angular part of the orbital (represented using spherical harmonics), we obtain an MF equation for the radial part of the orbital, which is a complex symmetric eigenvalue problem [42, 44].

The right eigenvector in the spatial representation can be written as

$$(\mathbf{r}|\phi_p) = \frac{u_{n_p,l_p}(r)}{r} Y_{l_p,m_p}(\theta, \phi), \quad (3.34)$$

where $u_{n_p,l_p}(r)$ is a real-valued function for occupied orbitals (since SES and CAPs are not supposed to affect what is in the interior region), while $u_{n_p,l_p}(r)$ is a complex-valued function for virtual orbitals. The left eigenvector in the spatial representation reads

$$(\phi_p|\mathbf{r}) = \frac{u_{n_p,l_p}(r)}{r} Y_{l_p,m_p}^*(\theta, \phi), \quad (3.35)$$

where the radial part is the same as for the right eigenstate (since it is an eigenstate of a complex symmetric Hamiltonian) and only the angular part is complex conjugated. The orthogonality relations among modified orbitals, which are ensured using the c -product, read

$$(\phi_p|\phi_q) = \delta_{p,q}. \quad (3.36)$$

- *Evaluation of matrix elements:* The orthogonality relations of the MF N -electron configurations follow the orthogonality relations of the modified orbitals. In particular, for the 1p-1h excitations, the relations defined via the c -product read [44]

$$(\Phi_i^a|\Phi_b^j) = \delta_{i,j} \delta_{a,b}. \quad (3.37)$$

This should be compared to the definition of the Hermitian inner product

$$\langle \Phi_i^a | \Phi_b^j \rangle = \delta_{i,j} \langle \phi_a | \phi_b \rangle \neq \delta_{i,j} \delta_{a,b}, \quad (3.38)$$

where we have used the fact that the nonhermiticity does not have any influence on the occupied orbitals and hence they are orthogonal to each other. The Hermitian product between two virtual orbitals are not zero, and this overlap integral needs to be calculated.

Since only the c -product guarantees the orthogonality of the MF basis set, the matrix elements for the Hamiltonian need to be replaced using $(\cdot|\cdot)$. The same holds for the matrix elements appearing in the EOMs in Eq. (2.30) [42, 44].

- *Evaluation of expectation values:* Expectation values are calculated using the Hermitian inner product such that it gives a real number [42, 44]. Since $\langle \Psi(t) | \neq |\Psi(t)\rangle^\dagger$, one needs, in principle, to perform a separate propagation for $\langle \Psi(t) |$. This causes some numerical difficulties since the norm of $\langle \Psi(t) |$ goes to infinity as the norm of $|\Psi(t)\rangle$ goes to zero [77]. As an approximation, we take $\langle \Psi(t) | \approx |\Psi(t)\rangle^\dagger$, which means that the effect of the absorber gets imprinted on the expectation value, whereas in the case of a separate propagation it would not [48].
- *Effects on the norm of the wave function and the IDM:* Since SES or a CAP acts as an absorber of the outgoing flux, the norm of the wave function $\langle \Psi(t) | \Psi(t)\rangle$ is not conserved during the time propagation anymore. This loss of the norm over time affects the density matrix $|\Psi(t)\rangle \langle \Psi(t)|$, and hence the ion density matrix $\sum_a (\Phi_i^a \Psi(t)) \langle \Psi(t) | \Phi_j^a$ in Eq. (2.31). Because the probability that there is no hole $|\alpha_0(t)|^2$ and the probability that there is a hole $\sum_i \rho_{i,i}^{\text{IDM}}(t)$ must add up to one, we must correct the IDM for the loss of norm during the time propagation. The details of this correction can be found in Ref. [44].

3.4 Summary

The key messages of this chapter are summarized as follows:

- ◊ During shape resonance, an excited particle is temporarily trapped by the potential barrier and then gets emitted by tunneling through the barrier (Sec. 3.1).
- ◊ Resonance dynamics can be fully described using one single eigenstate of TISE that satisfies outgoing wave BCs. Such a Siegert state is a metastable state characterized by a discrete, complex energy eigenvalue, i.e., the Siegert energy.
- ◊ SES and CAPs are two computationally efficient methods for the calculation of resonance eigenstates. The resulting resonance states are L^2 -integrable functions that are amenable to standard bound-state treatments (Sec. 3.2).
- ◊ The above two methods bring in a modified Hamiltonian that is non-Hermitian. Rigorous theory has been developed in order to understand the spectral properties and to classify different types of electronic structure of the non-Hermitian Hamiltonian.
- ◊ One important consequence of introducing non-Hermiticity is that one needs to distinguish between generalized c -product and standard Hermitian inner product.

- ◇ SES and CAPs can also be applied to time-dependent problems, where they are used to absorb ionized electron wave packet reflected at the edges of the numerical grid (Sec. 3.3). Whether we are solving TISE or TDSE in this thesis, we handle a non-Hermitian Hamiltonian using NHQM.

Chapter 4

Application I: Collective resonance behavior of Xe

It is the time to apply the theories explained in Chapters 2 and 3 to the study of ultrafast electronic resonances in atomic Xe. In this chapter, we investigate the short-lived collective resonances that occur during perturbative XUV photoionization in the Xe $4d$ inner shell.

This chapter is structured as follows. Sec. 4.1 introduces the Xe GDR, a prominent example of collective electronic behavior in atomic systems. Sec. 4.2 shows how we uncover the resonance substructure of the GDR, which has been strongly supported by a recent ex-

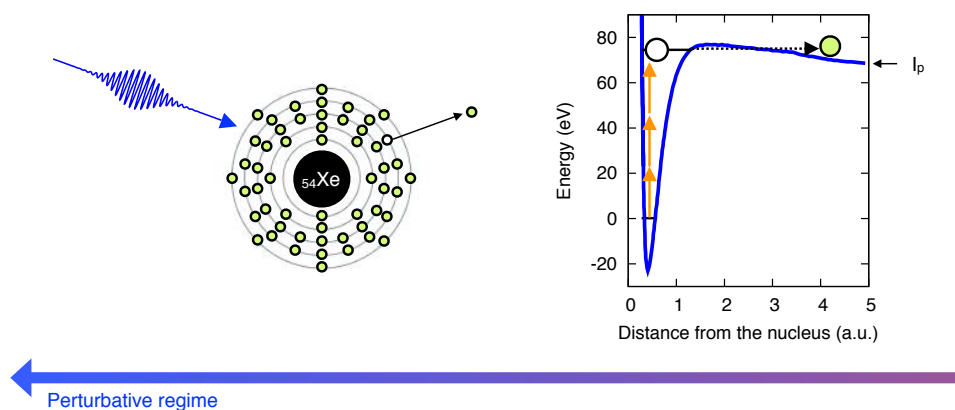


Figure 4.1. Topic of this chapter: short-lived collective resonances in XUV perturbative photoionization of the Xe $4d$ shell. For detailed description of the figure see the caption of Fig. 1.7(a). The main results presented here have been published in *Physical Review A* **91**, 032503 (2015) [52] and *Journal of Physics Communications* **2**, 045024 (2018) [91].

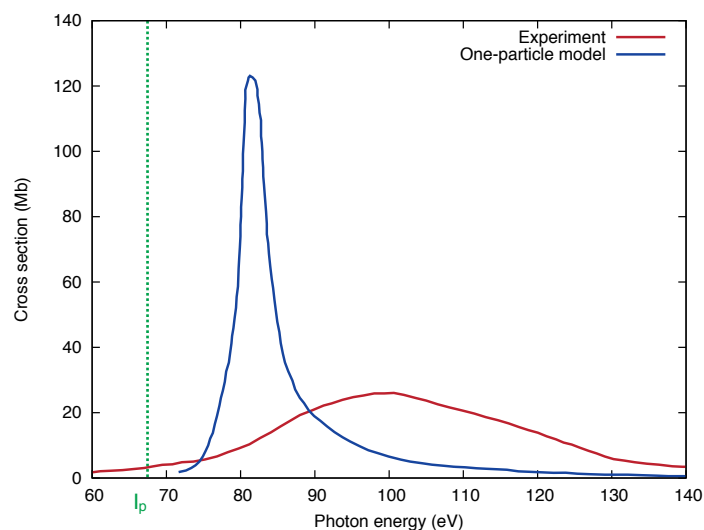


Figure 4.2. Comparison of the XUV one-photon absorption cross sections of Xe measured by Ederer and calculated by Cooper using independent-particle theory. The unit of the cross sections is megabarn (Mb). The $4d$ ionization threshold I_p is about 67.5 eV [104]. The data are taken from Refs. [82] and [141].

periment at FLASH. Sec. 4.3 presents a new perspective to understand collective dipole to multipole resonances and their spectroscopic fingerprints in and beyond the linear-response regime. Sec. 4.4 is the chapter summary.

4.1 Introduction

Introduction. Although the one-particle approximation can well describe a multielectron atom in several aspects, it fails conspicuously in some cases to capture the many-body nature of an atom. Indeed, as early as 1933, Bloch proposed the existence of plasma-like collective excitations within an atom [142]. It is well known nowadays that such collective excitations can take place during XUV one-photon ionization of heavy atoms, best showcased by the giant dipole resonance (GDR) of Xe [34, 84–86].

The GDR of Xe was first observed experimentally in 1964, independently by Ederer [82] and Lukirskii et al. [83]. Far from what would be anticipated from a hydrogenic one-electron model (that the cross section should drop monotonically above an ionization threshold until reaching the next one) [84], the one-photon cross section they measured shows a pronounced and nearly symmetric maximum centered around 100 eV with a width of about 40 eV in the

4d continuum (see Fig. 4.2).

This experimental finding triggered immediate theoretical interest. The first theoretical analysis of the GDR linear absorption spectrum was carried out by Cooper in 1964 [141]. By using a local MF model, Cooper explained the appearance of the resonance-like feature as follows. An inner 4d electron, after absorbing a photon, tends to go to an ϵf state [3]. It then experiences an effective spherically symmetric one-particle potential

$$v(r) = v_{\text{HFS}}(r) + \frac{l(l+1)}{2r^2}, \quad l = 3, \quad (4.1)$$

which is the HFS potential (with the Latter tail correction [143]) plus a repulsive term associated with the angular momentum of the photoelectron. The resulting total potential, as plotted in Fig. 4.1, has a centrifugal potential barrier, which is able to temporarily trap the electron. This shape-type resonance picture can account for the departure of the cross section from the prediction of the hydrogenic model [29].

The result of Cooper's calculation is compared to the experimental data in Fig. 4.2 [141]. Clearly, the occurrence of the resonance-like structure in the one-photon cross section can only be qualitatively explained by the one-particle model. Thanks to a vast amount of advanced many-body calculations in the next two decades [144–149], it is realized that the inclusion of electronic correlations plays a key role in bringing in the quantitative agreement between theory and experiment. The importance of correlation effects can be intuitively understood: right because of the temporary trapping of the excited electron close to the ion, strong particle-hole interactions are set off and dramatically modify the GDR linear spectrum given by the shape-resonance picture.

Nowadays it is well established that the Xe GDR must be described as the result of the collective excitations of at least all the ten electrons in the 4d subshell, forming short-lived plasma-like cooperative electronic motion [84, 85]. As the GDR is a property of inner-shell electrons, it is found in other atoms close to Xe in the periodic table and survives in molecules and solids [85, 86]. Furthermore, the atomic GDR is closely interconnected with the GDR in other types of many-body systems, such as nuclei, metallic clusters, fullerenes [84, 85].

State of the art and limitations. A considerable number of measurements have been performed for a precise characterization of the Xe GDR spectrum with perturbative XUV light sources [150–153]. However, with the birth of various new source technologies, this old spectroscopic feature continues to enthrall state-of-the-art experimenters. For example, in the perturbative light-matter–interaction regime, the GDR creates an anomalous charge-state

distribution when Xe is irradiated by an XVU FEL [154–156]. In the nonperturbative regime, the GDR leads to a striking enhancement of the plateau in the HHG spectrum when Xe is driven by an intense MIR laser [76], which mirrors the partial cross section of the $5p$ valence shell strongly modulated by the GDR [58] [see Fig. 1.5(b)]. Hence, it is important to fully understand the nature of the Xe GDR.

Following the earliest independent-particle model [141], various advanced many-body theories have succeeded in reproducing the experimental one-photon cross section associated with the Xe GDR remarkably well [147–149, 149, 157, 158]. Such linear-response-type studies have so far been our major source to gather information on the nature of the GDR. Indeed, even the interpretations on the HHG spectrum and the charge-state distribution of Xe were either derived [58] or extrapolated [154] from what one knows from the one-photon cross section. This means that little is known about (1) the GDR *resonance state* per se apart from its *simplest spectroscopic manifestation* and (2) the existence of other types of collective resonances in Xe, namely the *multipole collective resonances*.

In this chapter, we will overcome the above two limitations. We will first study the fundamental dipole resonance eigenmode(s) in the energy region around 100 eV, where the broad maximum in the linear spectrum is located. We will then tackle all types of resonances—be them dipole or multipole modes—from the most fundamental level, i.e., that of the resonance-state electronic structure. We will show how new understanding of the collective electron motion in the Xe $4d$ shell emerges as one goes beyond the conventional linear spectroscopic approach.

4.2 Exposing the hidden substructure of the giant dipole resonance

Motivation. As pointed out in the last section, a variety of advanced many-electron theories has been able to make substantial quantitative improvement of Cooper’s one-particle spectrum [141] and to reproduce the measured linear absorption spectrum associated with the Xe GDR exceptionally well [147–149, 149, 157, 158]. Nevertheless, a fundamental question frequently overlooked is what exactly are the basic collective resonance modes, or resonance eigenstates, that give rise to the spectral properties of the Xe GDR. A work by Wendin in 1971 [33] (see Ref. [147] for details) using RPAE identifies two collective resonances in this energy range.^a Another calculation, by Lundqvist in 1980 [159], utilizing a hydrodynamic

^aThrough private communications with Wendin, we have come to realize that Wendin does not consider that he found the GDR resonance substructure in Refs. [33, 147]. The reason is that Wendin thinks of resonances

treatment of electron density oscillations also finds two collective modes, but one of them sits at an energy quite incompatible with experimental observations. In addition to the very limited theoretical predictions of the resonance positions, neither of these studies explicitly specifies the resonance widths, which are key indicators of the sustainability of a collective excitation. Consequently, the nature of the inherent collective resonances hidden in the broad spectral blur of the Xe GDR still remains an unsolved question.

Contributions of this thesis. In this section, we provide the first thorough characterization of the resonance substructure underlying the Xe GDR. We resolve two collective dipolar resonances residing in the spectral range of the GDR, with one position differing from that given by Wendin [147] by 15 eV. Whereas Wendin resorted to an approximate condition only applicable to weakly damped plasma [160] to estimate the positions of the collective excitations (which is not ideal when dealing with short-lived resonances as in this case), this work provides quantitative results for the resonance positions and lifetimes without making such an approximation.

In contrast to the standard view that many-body correlations merely quantitatively shift and flatten one single resonance as inferred from the photoabsorption spectra [3, 141, 144–146, 148, 149], we demonstrate that many-body correlations result in fundamentally different resonance substructure in this energy region: whereas there is a group of resonances in our one-particle intrachannel model, we observe two far-separated resonances as soon as we switch on interchannel interactions involving the $4d$ electrons. In comparison to the plasma-type treatments used in Refs. [147, 159], the full many-body wave functions can be directly obtained in our approach. As the wave functions of the two resonances cannot be expressed by any single particle-hole state [161], we concretely show that they are indeed new collective modes.

Methodology. In this work, the isolation of the resonance substructures is consistently accomplished by means of two complementary and general methods implemented within the TDCIS framework (see 2.2.2). The first, time-dependent approach involves a novel application of the time-frequency Gabor analysis [162, 163] to the autocorrelation function of

as *resonance-like features* in the cross section. Since there is only one peak in the observed cross section, there is only one resonance from his perspective. This is in contrast to the view we hold: we see resonances as *fundamental eigenstates* or *electronic-structure properties* of a Hamiltonian, as in the theory of resonances [77, 124].

a wave packet (to be introduced in the upcoming subsection). While it is a common routine in molecular dynamics to look for resonance energies in the Fourier domain [164–166], our analysis in the combined time-frequency domain not only shows improved performance in disentangling strongly overlapping resonances, but also supplies an appealingly intuitive view on the time evolutions of various wave-packet components.

The second, time-independent approach provides a comprehensive characterization of all the resonance properties, including the resonance wave functions, by directly diagonalizing the N -body Hamiltonian using an NHQM technique, specifically the SES technique (see 3.2.1). Complex scaling is typically used to address resonance phenomena in few-electron atoms [167–170] and molecules [171], but it had not yet been used before for collective resonances in a multielectron system as complex as Xe.

A single set of numerical parameters is employed throughout our calculations to compare consistently the results obtained by the two approaches. It is worthwhile to reiterate that in both the time-dependent and time-independent approaches we have to handle a non-Hermitian Hamiltonian for the reason given in Sec. 3.3. Thus, care has to be taken in choosing the suitable form of inner products (see 3.2.3).

In the energy range of concern, it is adequate to assume that electron depopulations only happen from the $4d$, $5s$, and $5p$ orbitals.^b Nonetheless, for a meaningful comparison with the work by Wendin [147], the calculations presented first are performed without activating the outer $5s$ and $5p$ shells. As will be shown later, these channels only cause minor quantitative modifications. For further numerical details, please refer to the original publication [52].

To systematically assess the many-body effects, we often compare the results of two scenarios: the full CIS model and a reduced intrachannel model (see 2.2.3). The genuine two-electron correlations within CIS are fully encapsulated by the interchannel-coupling Coulomb matrix elements $(\Phi_j^b | \hat{H}_1 | \Phi_i^a)$ with $i \neq j$ [29, 45]. It is this type of interactions that can simultaneously change the state of the photoelectron ($a \rightarrow b$) and that of the cation ($i \rightarrow j$), enabling the formation of an entangled particle-hole pair [42]. In the intrachannel model, all the interchannel terms are set to zero, and only the intrachannel terms $(\Phi_i^b | \hat{H}_1 | \Phi_i^a)$ are considered [29, 45]. The intrachannel Hamiltonian effectively acts as a one-particle nonlocal potential [42].

^bThe experimental binding energies for the $4d$, $5s$, and $5p$ electrons are 67.5 eV [104], 23.4 eV [117], and 12.1 eV [117], respectively. The value corresponding to a higher total angular momentum quantum number j is taken, since its ionization threshold is lower. The average Auger decay width of the $4d$ holes is 107.5 meV [172], whose effect is mimicked by adding an imaginary part to the hole orbital (see 2.3).

4.2.1 Time-dependent approach to overlapping resonances

Here, we propose a general algorithm to extract Siegert energies out of resonance dynamics. This scheme is (1) applicable not only to electronic but also to other types of resonance phenomena, (2) based on wave-packet propagation, thus not requiring explicit knowledge of the resonance eigenfunctions, and (3) particularly suited for the situation when there are overlapping resonances, namely broad resonances with similar excitation energies.

Resonance dynamics in the time domain. The key physical quantity employed throughout our analysis is the time-dependent autocorrelation function defined as

$$C(t) \equiv (\Psi(0)|\Psi(t)), \quad (4.2)$$

where $|\Psi(0)\rangle$ is an initial wave packet and $|\Psi(t)\rangle$ is the freely evolved wave packet at a later time t . Note that the c -product (in the symmetric form) is adopted here. This is because, in time-dependent simulations, a complex potential is added to the field-free Hamiltonian in order to absorb the outgoing particle flux reaching the end of the numerical grid. No matter which method (e.g., ECS/SES [77] or CAPs [80]) is used to generate the complex potential, we are dealing with a Hamiltonian that is non-Hermitian (see Sec. 3.3). There is no restriction on which approach shall be chosen for the numerical solution of the TDSE.

For a quantitative determination of the resonance Siegert energies, we assume that, by proper preparation, the initial state is essentially composed of the resonance states of interest and all the contributions from the bound states and the continuum can be ignored. Expanding $|\Psi(0)\rangle$ in terms of the orthonormal resonance wave functions $|\Psi(0)\rangle = \sum_n a_n |\Phi_n\rangle$, Eq. (4.2) then bears the following structure

$$C(t) = \sum_n a_n^2 e^{-iE_n t - \frac{\Gamma_n}{2} t}. \quad (4.3)$$

The validity of Eq. (4.3) and the resonances that can be extracted evidently depend on the quality of $|\Psi(0)\rangle$. How we prepare the wave packet ideal for studying the GDR of Xe will be discussed in the upcoming subsection.

Resonance dynamics in the frequency domain. A common strategy to infer Siegert energies from wave-packet propagation is to conduct a Fourier analysis and study the autocorrelation function in the frequency domain [164–166]. Performing a one-sided Fourier

transformation on Eq. (4.3) [assuming $C(t) = 0$ for $t < 0$] yields

$$\begin{aligned} C(\omega) &= \frac{1}{\sqrt{2\pi}} \int_0^{+\infty} dt e^{i\omega t} C(t) \\ &= \sum_n \frac{a_n^2}{\sqrt{2\pi}} \frac{\frac{\Gamma_n}{2} + i(\omega - \Xi_n)}{\frac{\Gamma_n^2}{4} + (\omega - \Xi_n)^2}, \end{aligned} \quad (4.4)$$

i.e., a superposition of Lorentzian functions and dispersive curves parametrized by the Siegert energies.^c

For a single resonance, the spectral distribution of the autocorrelation function reads

$$|C^{(1)}(\omega)|^2 = \frac{|a_1^2|^2}{2\pi} \frac{1}{\frac{\Gamma_1^2}{4} + (\omega - \Xi_1)^2}, \quad (4.5)$$

which is a Lorentzian with a peak at Ξ_1 and a width of Γ_1 . If more than one resonance exists, $|C(\omega)|^2$ comprises several Lorentzians and their interferences. Upon empirically specifying the number of resonance states, it is possible to retrieve the Siegert energies by numerically fitting $|C(\omega)|^2$ based on Eq. (4.4).

Resonance dynamics in the time-frequency domain. Next, we extend the standard spectral analysis to a time-frequency analysis [162, 163, 173] of the autocorrelation function and examine its information content in the *combined time-frequency domain*. Applying a Gabor transformation [163, 174, 175] to Eq. (4.3), we can derive

$$C_t(\omega) = \frac{1}{\sigma\sqrt{2\pi}} \int_0^{+\infty} dt' e^{i\omega t'} e^{-\frac{(t'-t)^2}{2\sigma^2}} C(t') \quad (4.6)$$

$$\approx \sum_n a_n^2 e^{\frac{\sigma^2 \Gamma_n^2}{8} - \frac{\Gamma_n}{2} t - \frac{\sigma^2}{2} (\omega - \Xi_n)^2 + i\sigma^2 (\frac{t}{\sigma^2} - \frac{\Gamma_n}{2})(\omega - \Xi_n)}. \quad (4.7)$$

Equation (4.6) can be interpreted as gating the time-dependent signal by a Gaussian window function of width σ centered at t . Due to the finite size of the window function and the sudden turn-on of the autocorrelation function at $t = 0$, the analytical expression in Eq. (4.7) works as a reasonable approximation to $C_t(\omega)$ when $t \gg \sigma$.

For a single resonance, the transient spectral distribution of the autocorrelation function at time t can be simply approximated by

$$|C_t^{(1)}(\omega)|^2 \approx |a_1^2|^2 e^{\frac{\sigma^2 \Gamma_1^2}{4}} e^{-\Gamma_1 t} e^{-\sigma^2 (\omega - \Xi_1)^2}, \quad (4.8)$$

^cNote that a_n^2 is a complex number and can impart an additional phase to the following functions. This also results in the fact that it remains difficult to devise an analytic signal extending $C(t)$ into $t \in (-\infty, 0]$.

i.e., a Gaussian with a peak at Ξ_1 and a width determined by σ . From the decay rate of the amplitude, Γ_1 can be extracted.

The advantage of the Gabor analysis over the Fourier analysis becomes apparent when *multiple resonances* come into play. In this situation, $|C(\omega)|^2$ comprises several Gaussians and their interferences. Consider the example where there are overlapping broad resonances yet with different lifetimes. Compared to the static information conveyed by the Fourier spectrum, it is more likely to detect the resonances through the time evolution of the Gabor profile, where their competition causes dynamics in the frequency distribution. Quantification of the resonance energies can be done by fitting $|C_t(\omega)|^2$ with the help of Eq. (4.7) at different time steps.

It is worthwhile to note that $C(\omega)$ is related to a measurable physical quantity—the linear photoabsorption cross section [51, 176]—although we usually consider its modulus squared to reduce the number of irrelevant fitting parameters (e.g., the phase of a_n^2). Also, a real physical observable—the dipole moment—can be used in the time-frequency analysis as well.^d In this case, its frequency distribution is associated with the spectrum of electromagnetic radiation emitted by the system [177]. Finally, it is tempting to point out the conceptual similarity between the Gabor transformation and the spectrogram measured in a pump-probe experiment [90, 178, 179], albeit there is no real probe pulse involved in the current theory.

4.2.2 GDR substructure revealed: time-dependent method

We now apply the time-dependent approach to overlapping resonances presented in the previous subsection to decode the electronic resonance substructure of the 4d GDR of Xe. The wave-packet dynamics shown below are obtained by numerically solving the field-free N -electron TDSE using the TDCIS approach (see Sec. 2.2).

GDR dynamics in the time domain. To probe the resonances associated with one-photon absorption, the initial wave packet can be conveniently set as

$$|\Psi(0)\rangle = \hat{D}_z |\Phi_0\rangle, \quad (4.9)$$

^dThe reason for analyzing the autocorrelation function instead of the dipole moment is that the former is a complex quantity, which often gives rise to neater analytical expressions for the (time-)frequency distributions.

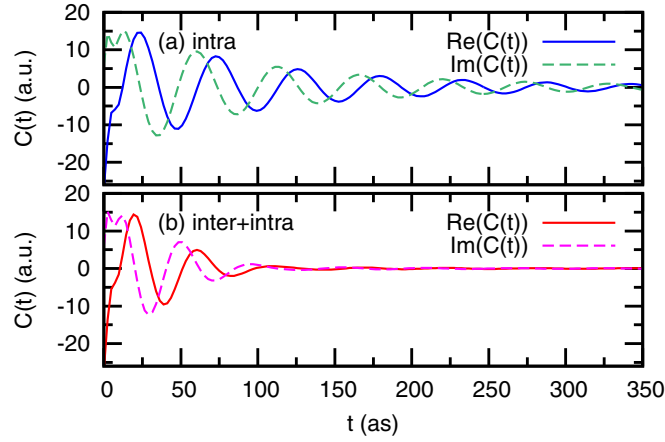


Figure 4.3. Autocorrelation functions $C(t)$ as a function of time for **(a)** the intrachannel model (“intra”) and **(b)** the full TDCIS model (“inter+intra”). Solid curves represent the real part, and dashed curves the imaginary part, of $C(t)$. The figure is reproduced from Ref. [52]. Copyright ©2015 American Physical Society.

, where \hat{D}_z denotes the z component of the dipole operator relative to the polarization direction of the electric field in a measurement.^e Eq. (4.9) is equivalent to creating a wave packet via a delta-kick pulse polarized along the z axis. Since it is well known that the Xe GDR exhausts all the oscillator strength in the XUV region [84, 85], the wave packet prepared in this way is largely composed of the relevant resonances, and its autocorrelation function $C(t)$ is expected to take the form assumed in Eq. (4.3).

The wave packet subsequently undergoes field-free relaxation. Fig. 4.3 plots the time evolution of the complex-valued autocorrelation function for both the reduced one-electron intrachannel model and the many-electron full TDCIS model. The raw data in both cases look like a simple damped oscillator without much structure apart from some spikes in the beginning. This suggests that there are some dynamics that rapidly disappear, which arise from a slight population of the initial wave packet in the continuum states (where a particle will not get trapped) [78]. Including the interchannel interactions causes the autocorrelation function to attenuate more rapidly and to ring at a higher frequency.

^eThe dipole operator in either the length or the velocity gauge can be used (see 2.1.2). The choice does not affect the retrieved Siegert energies. However, since the CIS theory is not strictly gauge invariant [43], the wave function of $|\Psi(0)\rangle$ has a slight degree of gauge dependence. In this study, we choose the velocity-form dipole operator, namely, \hat{P}_z .

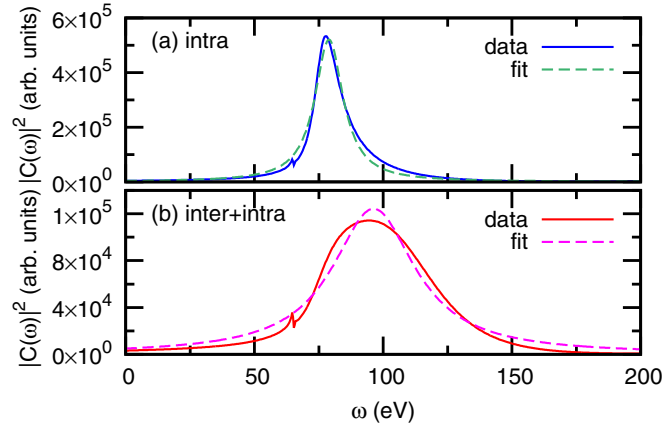


Figure 4.4. Autocorrelation functions $|C(\omega)|^2$ in the frequency domain for (a) the intrachannel model (“intra”) and (b) the full TDCIS model (“inter+intra”). Solid curves represent the data, dashed curves the fit with Eq. (4.5). The figure is reproduced from Ref. [52]. Copyright ©2015 American Physical Society.

GDR dynamics in the frequency domain. The above features are more pronounced if we look at the autocorrelation functions in the frequency domain as illustrated in Fig. 4.4.^f The Fourier transform $|C(\omega)|^2$ in each calculation shows one smooth peak, accompanied by Rydberg series preceding the $4d$ ionization energy [51]. The linewidth of the Rydberg states is narrow, since a $4d^{-1}$ hole decays on the femtosecond time scale [172]. Switching on the interchannel couplings broadens and weakens the peak as well as displacing it to a higher frequency, similar to what is seen in the one-photon absorption spectra (see Fig. 4.2 and Ref. [51]).

We can extract the effective Siegert energy for the single peak in Figs. 4.4(a) and 4.4(b). The data are fitted numerically with Eq. (4.5) utilizing the nonlinear least-squares Marquardt-Levenberg algorithm. This yields $(\Xi, \Gamma) = (79.0 \text{ eV}, 12.9 \text{ eV})$ for the intrachannel model and $(96.3 \text{ eV}, 38.9 \text{ eV})$ for the full TDCIS model. Note that $|C(\omega)|^2$ in the full TDCIS model is relatively poorly described by its Lorentzian fit and is more asymmetric, a hint to the multiple resonances behind the huge spectral hump of the Xe GDR.

GDR dynamics in the time-frequency domain. Now we are in a position to go beyond the standard spectral method and to investigate the Xe GDR in the combined time-frequency

^fAt this step, $C(t)$ is exponentially damped by hand to reduce the spectral aliasing error [140]. More specifically, $C'(t) \equiv C(t)e^{-t/\tau}$, with $\tau \approx 108 \text{ a.u.}$ [107]. This adds a global, small lifetime to all the wave-packet components and can be easily rectified afterwards.

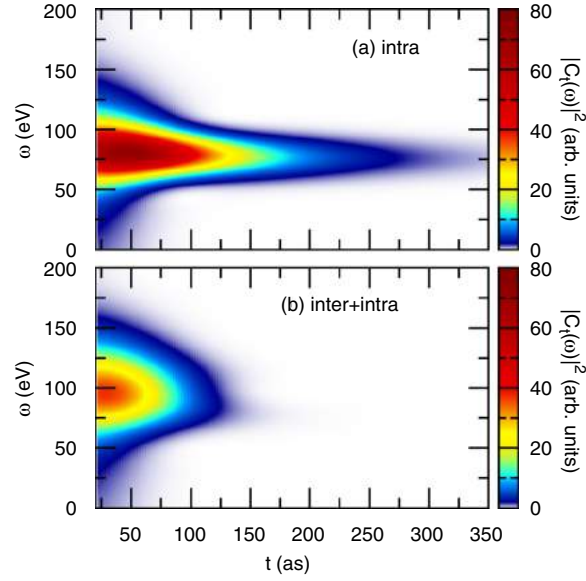


Figure 4.5. Autocorrelation functions $|C_t(\omega)|^2$ in the combined time-frequency domain for (a) the intrachannel model (“intra”) and (b) the full TDCIS model (“inter+intra”). The figure is reproduced from Ref. [52]. Copyright ©2015 American Physical Society.

domain. Fig. 4.5 depicts the Gabor transform $|C_t(\omega)|^2$ for both the intrachannel and the full TDCIS models.⁸ In addition to the information that is already revealed by $C(t)$ and $|C(\omega)|^2$, one salient new feature emerges: the spectral distribution in the intrachannel case dies out almost symmetrically over time, whereas the spectral distribution in the full TDCIS model decays asymmetrically, with the maximum shifting to a lower energy. In the vicinity of 150 as, one can clearly recognize two frequency components in Fig. 4.5(b), and can deduce that the higher-energy one has a shorter lifetime.

Figure 4.6 presents snapshots of the frequency distributions $|C_t(\omega)|^2$ in Fig. 4.5 at consecutive time steps, where the characteristics we allude to can be even better visualized. In the intrachannel model, Figs. 4.6(a)-4.6(c) exhibit one single, decaying peak around 80 eV. In the full TDCIS model, the time evolution of the transient spectral distribution is fundamentally different. In Fig. 4.6(d), the initial spectrum displays a broad and nearly symmetric peak located around 90 eV. However, the spectrum soon becomes highly asymmetric, with the maximum shifting to a lower energy, and decays more rapidly than the intrachannel case.

⁸At this point, we filter out the tiny contribution from the Rydberg series to focus on the properties pertaining to the GDR. Another autocorrelation function, $C''(t)$, is defined by removing the Rydberg series in $C'(\omega)$, interpolating the remaining curve using the natural cubic splines, and then inverse Fourier transforming it back to the time domain.

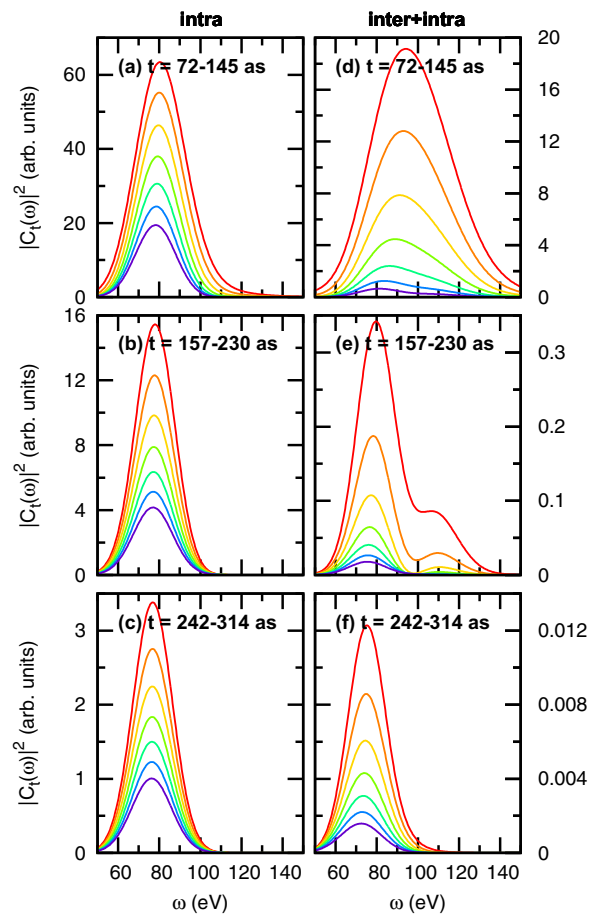


Figure 4.6. Decay dynamics of the Gabor spectra $|C_t(\omega)|^2$ at consecutive time intervals. **(a)-(c)** Intrachannel model (“intra”); **(d)-(f)** full TDCIS model (“inter+intra”). In each panel, the time step between two neighboring lines is about 3 as. The figure is reproduced from Ref. [52]. Copyright ©2015 American Physical Society.

The successive dynamics in Fig. 4.6(e) vividly illustrate how the substructure in the GDR develops: two peaks can be identified, and the higher-lying one fades away much more quickly. This is followed by Fig. 4.6(f), where the higher-lying mode has completely vanished and only the lower-lying one remains, with a position similar to that of the intrachannel resonance. Just based on simple observations, the Gabor analysis intuitively illuminates how the interchannel interactions result in the damping and fragmentation of the resonances, as well as a rough idea of the positions and widths of the two sub-resonances. Benefiting from the fact that different spectral components have different lifetimes, the Gabor analysis successfully decodes the resonance substructure of the GDR, which cannot be achieved by the Fourier analysis.

Characterization of the GDR substructure. Next, the Siegert energies are quantitatively determined following the logic presented in 4.2.1. In our intrachannel model, we know that the three symmetry-adapted ionization channels, $4d_0$, $4d_{\pm 1}$, and $4d_{\pm 2}$, should behave in a similar way, so every one of them should support a resonance (although these three intrachannel resonances cannot be distinguished and act as a group in our analysis so far). Using this *a priori* input, we perform the analysis in the intrachannel case for each $4d_{\pm m}$ ionization channel. One peak in the Gabor profiles at subsequent time steps is then fitted numerically with Eq. (4.8). The outcomes are listed in Table 4.1. Note that there is a minute splitting among the intrachannel resonance energies, $\Xi_{4d_{\pm 1}} > \Xi_{4d_{\pm 2}} > \Xi_{4d_0}$ and $\Gamma_{4d_{\pm 1}} > \Gamma_{4d_{\pm 2}} > \Gamma_{4d_0}$. This splitting already leaves its trace in Figs. 4.6(a)-4.6(c): as time passes by, the peak position gradually moves towards a slightly lower frequency, in accordance with the fitting results that the lowest-lying intrachannel resonance has the smallest decay width.

For the full CIS model, the fitting process is dissected into two stages. In the first stage, roughly corresponding to the time interval shown in Fig. 4.6(e), two resonances are singled out. Resorting to Eq. (4.7) with $n = 2$, the Gabor spectrum has the approximate analytical expression

$$|C_t^{(2)}(\omega)|^2 \approx f_{1,t}(\omega) + f_{2,t}(\omega) + 2[f_{1,t}(\omega)f_{2,t}(\omega)]^{1/2} f_{1-2,t}(\omega), \quad (4.10)$$

where

$$f_{n,t}(\omega) \equiv |a_n^2|^2 e^{\frac{\sigma^2 \Gamma_n^2}{4}} e^{-\Gamma_n t} e^{-\sigma^2(\omega - \Xi_n)^2}, \quad n = 1, 2,$$

$$f_{1-2,t}(\omega) \equiv \cos \left[\frac{\sigma^2(\Gamma_2 - \Gamma_1)\omega}{2} + (\Gamma_2 - \Gamma_1)t - \frac{\sigma^2(\Gamma_2\Xi_2 - \Gamma_1\Xi_1)}{2} + (\phi_2 - \phi_1) \right]. \quad (4.11)$$

Table 4.1. Siegert energies of the resonances in the intrachannel model (“Intra”) and the full TDCIS model (“Full”). Results are listed for the Gabor analysis (see 4.2.2) and for the SES method (see 4.2.3). For comparison, the predictions given by Wendin [147] are included.

	Gabor ^a		SES ^b		Wendin [147]	
	Ξ_n (eV)	Γ_n (eV)	Ξ_n (eV)	Γ_n (eV)	Ξ_n (eV)	Γ_n (eV)
Intra: $4d_0$	76.5 ± 0.3 ^c	8.2 ± 0.4 ^c	76.3	8.3	–	–
Intra: $4d_{\pm 1}$	77.9 ± 0.7 ^c	13.5 ± 0.4 ^c	77.6	13.8	–	–
Intra: $4d_{\pm 2}$	77.4 ± 0.3 ^c	10.6 ± 0.1 ^c	77.2	10.6	–	–
Full: R_1	80.4 ± 0.7 ^d , 73 ± 2 ^e	32 ± 1 ^d , 17.8 ± 0.4 ^e	74.3	24.6	74.3	–
Full: R_2	112 ± 1 ^d	47 ± 9 ^d	107.2	59.9	92.3	–

^a In each calculation, the Gabor spectra are fitted numerically in a time interval $[t_i, t_f]$ at a time step of 3 as. This gives the fitting parameters Ξ_n, Γ_n as a function of time. Error bars are then defined as the standard deviations of Ξ_n, Γ_n over the time sequence.

^b All SES values have an error bar of 0.1 eV. This is calculated by varying over a reasonable range the numerical parameters such as the number of radial grid points, the maximum radial coordinate, and the SES parameters θ and λ .

^c Using Eq. (4.8) for one resonance in $[t_i, t_f] = [145 \text{ as}, 363 \text{ as}]$.

^d Using Eq. (4.10) for two resonances in $[t_i, t_f] = [145 \text{ as}, 169 \text{ as}]$.

^e Using Eq. (4.8) for one resonance in $[t_i, t_f] = [242 \text{ as}, 363 \text{ as}]$.

In Eq. (4.10), the first two terms are the individual contributions from the two identified dipole resonances R_1 and R_2 , and the third one is their interference. In Eq. (4.11), ϕ_n denotes the phase of a_n^2 . The data are fitted with the above formulas, and the Siegert energies are listed in Table 4.1. The error bars here are bigger than those in the intrachannel case, especially for the decay width of the faster-decaying R_2 . This is possibly due to the increasing difficulties in the nonlinear fitting procedure. Also, in order to arrive at the analytical expression for $|C_t(\omega)|^2$, Eq. (4.3) assumes that all the contributions to $C(t)$ from the bound states and the continuum can be neglected, which is less appropriate if the resonances decay relatively rapidly.

In the second stage, which nearly coincides with the time interval shown in Fig. 4.6(f), only one resonance is seen. Using Eq. (4.8), we produce another Siegert energy for R_1 in Table 4.1. It does not fully agree with that retrieved at the former stage, especially in terms of the resonance width. The two-resonance model used at the first stage is only applicable in a short period of time, where the resonance parameters certainly cannot fluctuate too much. Hence, this discrepancy reflects further numerical instability in the fitting parameters that cannot be entirely represented by the previously calculated uncertainties. Since the Gabor spectrum in this time interval has a fairly weak amplitude, the contribution from the Rydberg

series (after the filtering) inevitably kicks in. As a result, the effective energy position and width for R_1 acquired at this second stage are lower than those extracted at the first stage.

The most appealing feature of the Gabor analysis is that it provides an intuitive dynamical view on the competition between various spectral components, which may be connected to what is measured in a pump-probe experiment [90, 178, 179]. However, it is apparent that the Gabor method cannot quantify Siegert energies very accurately due to the assumption made in deriving the analytical expression for $C(t)$ in Eq. (4.3) and the nonlinear fitting procedure. Considering the energy uncertainties and the discrepancy between the resonance energies for R_1 extracted at two different stages, the Gabor analysis gives an overall energy resolution of ≈ 10 eV.

4.2.3 GDR substructure revealed: time-independent method

The existence of two dipole resonances R_1 and R_2 in the GDR energy region given by the full TDCIS model can also be unveiled using a time-independent approach. Here, we employ the SES technique to transform the field-free CIS N -electron Hamiltonian in the CIS configuration space (see Sec. 3.2), and then numerically diagonalize the resulting Hamiltonian using the iterative Arnoldi algorithm implemented in the ARPACK library [180] (see Sec. 2.2). An initial random vector is used to launch the iteration.

In comparison to the Gabor analysis of the resonance wave-packet dynamics, this time-independent approach has the following advantages: (1) the Siegert energies obtained are free from fitting errors, and (2) it provides complete information on the resonances including the Siegert energies as well as the L^2 -integrable resonance wave functions.

Since we concentrate on the resonance modes in the linear-response regime, the eigenstates shown below are required to have a minimum overlap with the HF ground state through a dipole transition: $|(\Psi|\hat{D}_z|\Phi_0)| > 10^{-6}$.

Figure 4.7 shows the complex energy spectra of the energy eigenvalues for the case with only intrachannel couplings and the case with both inter- and intrachannel couplings, i.e., the full-model calculation within CIS. Ideally, the energy spectra in both cases should follow the structure predicted by the Balslev-Combes theorem [121, 126, 127, 129] (see 3.2.1): the bound states remain on the real energy axis, the continuum is rotated clockwise by twice the scaling angle, 2θ , with respect to the $4d$ ionization threshold at 67.5 eV [104], and the resonances are exposed poles above the rotated continuum. However, the use of an

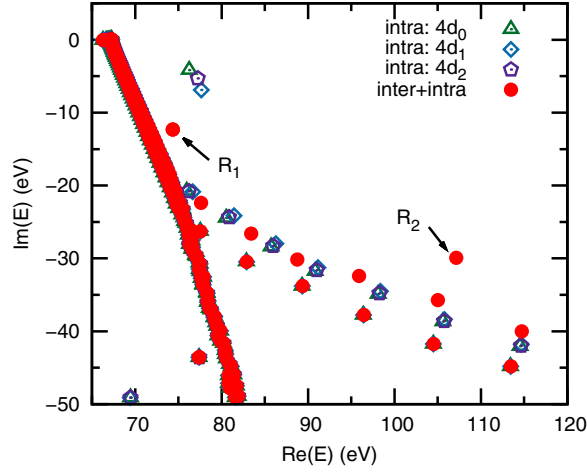


Figure 4.7. Complex energy spectra of the complex-scaled many-body Hamiltonian for the intrachannel (“intra”) and full CIS (“inter+intra”) models. Horizontal and vertical axes represent the real and imaginary parts of the energy eigenvalues, respectively. Three close-lying resonances are found in the intrachannel calculation (indicated by open polygons); two far-separated resonances (labeled R_1 and R_2) are found in the full CIS calculation (indicated by filled circles). The figure is reproduced from Ref. [52]. Copyright ©2015 American Physical Society.

incomplete basis set results in numerical artifacts such as branching of the continuum away from the threshold [136] and a rotation angle deviating from 2θ [181]. Recall that the eigenenergy of each resonance pole is the Siegert energy [80, 121]: $E = \Xi - i\Gamma/2$, with Ξ the excitation energy and Γ the inverse lifetime for the quasibound electron to escape to infinity.

Complex energy spectrum in the GDR region: intrachannel model. First, we focus on the result of the intrachannel-coupling model in Fig. 4.7. In this case, each eigenstate possesses a unique hole index i and the contributions from different $4d$ ionization channels can be easily set apart. Three resonances are found, one for each $4d_{\pm m}$ channel. They lie fairly close to each other, forming a group of resonances around an energy with a real part ≈ 77 eV and an imaginary part ≈ -5.4 eV, which corresponds to a lifetime of ≈ 60 as. The resonance positions and widths in the intrachannel model are detailed in Table 4.1. The SES results are in excellent agreement with the results of the Gabor analysis within the fitting error bars. In particular, the minute splitting trend of the three intrachannel resonances is described consistently by the two complementary methods.

In order to elucidate the origin of the small splitting among the intrachannel resonances,

we perform another intrachannel calculation by approximating the residual Coulomb interaction \hat{H}_1 with its monopole term [45]. When so doing, the resonances associated with the $4d_0$, $4d_{\pm 1}$, and $4d_{\pm 2}$ channels have exactly the same resonance energy. Therefore, even without many-body effects, the electron excited from the different $4d_{\pm m}$ orbitals experiences different potentials owing to the shape of the nonspherical ionic core. This qualitative effect, although small, clearly exemplifies the impact of the ionic structure beyond the description of a simple spherically symmetric potential (e.g., the Herman-Skillman [182] or HF [109] potentials) or even an angular-momentum-dependent pseudopotential [183] widely used to model multi-electron atoms in perturbative [141, 184] or nonperturbative [40, 185, 186] light fields.

Complex energy spectrum in the GDR region: full CIS model. Activating interchannel coupling, the group of intrachannel resonances becomes two resonance states distantly located in the complex energy plane in Fig. 4.7. We have checked carefully that their positions do not vary with the scaling parameters, so they are not numerical artifacts. In comparison with the intrachannel resonances, resonance R_1 in Fig. 4.7 has almost the same excitation energy but a larger decay width; resonance R_2 is pushed away much farther into the lower half of the complex energy plane. The change of the resonance substructure upon the inclusion of interchannel couplings highlights that many-body correlations not only are required for a quantitative agreement between theory and experiment [3, 141, 144–146, 148], but in fact give rise to a fundamentally different resonance substructure in the GDR energy region. This is a unique insight provided by our study, since Ref. [147] does not show calculations without many-body correlations. The positions and widths of the resonances in the full model are listed and compared to the results of Gabor analysis in Table 4.1. In comparison to the intrachannel case, the discrepancy between the Siegert energies given by the two methods agree less well in the fully interacting case, especially for the fast-decaying R_2 and when using the two-resonance fitting model. This again emphasizes the drawback of the Gabor analysis, namely the larger error bars associated with the fitting procedure.

With the interchannel interactions, each resonance cannot be attributed to a single ionization pathway. By examining the ion density matrix $\rho_{i,j}^{\text{IDM}}$ in Eq. (2.31) for each resonance wave function, we find that, for both R_1 and R_2 , the $4d_0^{-1}$, $4d_{\pm 1}^{-1}$, and $4d_{\pm 2}^{-1}$ hole populations have a rough ratio of 1 : 2 : 1, which can be explained by an angular momentum analysis. Because the interchannel interactions strongly couple the various $4d_{\pm m}^{-1}$ hole states, it is crucial to consider the orbitals in addition to the one aligned along the polarization axis (i.e., $4d_0^{-1}$) for the physical processes involving the GDR, e.g., the giant enhancement in the HHG spectrum of Xe [58]. We also compute the angular momentum composition of the excited

electron, which shows a prominent f -wave character for both the resonances. This is true in our intrachannel calculation, too. Indeed, the Xe GDR is dominated by $4d \rightarrow \epsilon f$ transitions with roots in the independent-particle picture [3, 141].

Analysis of the many-electron resonance wave functions. Our time-independent CIS approach gives the total many-body resonance wave functions, which are not attainable using plasma-type treatments including RPAE, whose focus is to directly calculate the many-body linear response function [33, 144, 159]. We analyze $|\Phi_1\rangle$ and $|\Phi_2\rangle$ by decomposing them in terms of the orthonormal intrachannel basis set:

$$|\Phi_n\rangle = \sum_{m=0,1,2} a_{\pm m} |\Phi_{4d_{\pm m}}\rangle + |\Delta\Phi_n\rangle, \quad n = 1, 2. \quad (4.12)$$

The first term in Eq. (4.12) contains the projections onto the intrachannel resonance functions $|\Phi_{4d_{\pm m}}\rangle$, and the second term symbolizes the remaining part with respect to the other intrachannel states. The complex weights $a_{\pm m}^2$ defined through the symmetric inner product are listed in Table 4.2. For both R_1 and R_2 , a_0^2 , $a_{\pm 1}^2$, and $a_{\pm 2}^2$ have the same order of magnitude. For R_1 , the intrachannel resonances account for a weight of $\sum_m a_m^2 \approx 0.7$ out of a total norm of 1; for R_2 , they contribute a weight ≈ 0.3 . This means that the interchannel interactions not only mix all the intrachannel resonance states, but also mix in continuum states to form new resonances. At this stage, we clearly see in our configuration-interaction language why we can refer to R_1 and R_2 as new *collective dipolar modes*: they are entangled particle-hole states involving the various $4d_{\pm m}^{-1}$ hole states and do not resemble any single intrachannel resonance wave function.^h In RPAE, collective excitations are not directly defined by the many-body wave functions themselves, but by a coherent sum over different particle-hole states in evaluating the dipole [84] or dielectric function [147, 160] matrix elements. Note that both collective states have a significant overlap with the HF ground state via a dipole transition, with $\langle\Phi_1|\hat{D}_z|\Phi_0\rangle \approx 1.1$ and $\langle\Phi_2|\hat{D}_z|\Phi_0\rangle \approx 1.9$ for R_1 and R_2 , respectively.

4.2.4 Consequence of the approximation to the zeros of a dielectric function

Comparison to the previous work by Wendin. Here, we compare the excitation energies of the two collective dipole sub-resonances R_1 and R_2 predicted in this work to those calculated by Wendin in Ref. [147] (resonance widths are not calculated therein), which are also listed

^hAlternatively, one can also compute the oscillator strengths [3] for R_1 and R_2 within the NHQM framework to demonstrate the many-body nature of the resonances.

Table 4.2. Complex weights $a_{\pm m}^2$ with respect to the intrachannel resonance states $|\Phi_{4d_{\pm m}}\rangle$ for the collective resonances $|\Phi_1\rangle$ and $|\Phi_2\rangle$ in SES calculations.

	R_1	R_2
a_0^2	$0.175 - 0.033i$	$0.075 + 0.042i$
$a_{\pm 1}^2$	$0.345 + 0.009i$	$0.106 + 0.003i$
$a_{\pm 2}^2$	$0.198 - 0.018i$	$0.081 + 0.028i$
$\sum_m a_m^2$	$0.719 - 0.042i$	$0.262 + 0.073i$

in Table 4.1. The results of our SES method are chosen for the discussion here as the Siegert energies obtained using this method do not suffer from fitting errors. The resonance position of R_1 agrees perfectly with that given by Wendin. The position for R_2 differs from Wendin's number by 15 eV, but both positions are compatible with the spectral blur observed in the experimental XUV one-photon absorption cross section (see Fig. 4.2).

Although the RPAE approach taken in Ref. [147] contains higher order of electronic correlation effects in comparison to the CIS approach, we argue that the resonance parameters given in this work may be more reliable.ⁱ The reason comes from an approximate condition used in Ref. [147] to find collective excitations from the effective dielectric function. In principle, a collective resonance corresponds to a complex frequency where both the real and the imaginary parts of the many-body dielectric function simultaneously become zero [160, 187]. An estimated resonance position can be found by determining along the real energy axis a root for the real part of the dielectric function, *provided that the damping of the true resonance is sufficiently small* [160]. As one is dealing with two rather broad resonances in the case of the Xe GDR (particularly for R_2), this approximate condition, which is adopted by Wendin [147], is not strictly applicable. We believe that this is the most likely source for the discrepancy of Ξ_2 predicted in Ref. [147] and this present work.

Demonstration of the consequence of the approximate condition. We now demonstrate how the approximate condition of finding the zeros of the dielectric function invoked in Ref. [147] can result in Siegert energies that substantially deviate from the true resonance

ⁱWe point out that the exact values of the Siegert energies of R_1 and R_2 warrant further theoretical refinement. The CIS theory only contains 1p-1h configurations (in addition to the HF ground state). Hence, real and virtual double excitations [29, 84, 147] are among the physical processes outside the scope of the current study. Nonetheless, since TDCIS (in the velocity gauge) produces a peak position in good agreement with the experimental photoabsorption cross section [51], we expect that the inclusion of double excitations would not affect the resonance parameters substantially.

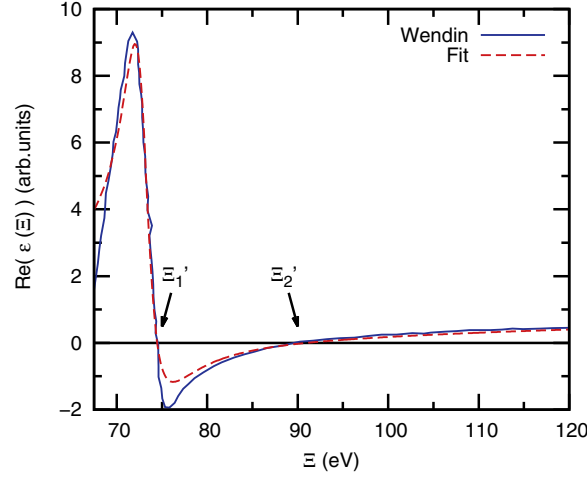


Figure 4.8. Real part of the many-body dielectric function $\text{Re}(\epsilon)$ along the real energy axis Ξ . Solid curve, Wendin's data [147]; dashed curve, fit with Eq. (4.13). The two resonance positions determined in the spirit of Wendin's work are labeled Ξ'_1 and Ξ'_2 . The figure is reproduced from Ref. [52]. Copyright ©2015 American Physical Society.

poles.

A collective resonance obtained from diagonalizing the complex-scaled many-body Hamiltonian corresponds to an energy $E_n = \Xi_n - i\Gamma_n/2$ in the complex energy plane where both the real and the imaginary parts of the many-body dielectric function $\epsilon(E)$ simultaneously vanish [160, 187]. In the limit of $\Gamma_n \rightarrow 0$, this exact condition is reduced to finding the roots of the real part of $\epsilon(\Xi)$ along the real energy axis Ξ , $\Gamma = 0$ [160].

For a dielectric function with two poles in the energy range of interest, it must follow the simple analytical structure in the complex energy plane [187]

$$\epsilon(E) = \frac{1}{1 - \left(\frac{a_1}{E - E_1} + \frac{a_2}{E - E_2} \right)}, \quad (4.13)$$

where a_1 and a_2 are two complex numbers.

To extract Wendin's dielectric function for the Xe GDR, we fit the real part of the data in Ref. [147] with $\text{Re}(\epsilon(\Xi))$ in Eq. (4.13). The a_n are treated as fitting parameters, and the E_n as known constants with the values given by the SES method in Table 4.1 (as mentioned before, we believe that our Siegert energies are closer to the true ones). The real part of the reconstructed dielectric function (with $a_1 = -10.0 - 19.7i$ and $a_2 = -1.6 + 6.4i$) is shown in Fig. 4.8, and describes Wendin's result reasonably well.

The real part of $\epsilon(\Xi)$ we retrieve passes through the real energy axis at $\Xi'_1 = 74.5$ eV and $\Xi'_2 = 91.0$ eV, which do not coincide with the excitation energies of the true collective poles $\Xi_1 = 74.3$ eV and $\Xi_2 = 107.2$ eV. This strongly indicates that the approximate condition of finding the roots of $\text{Re}(\epsilon(\Xi))$ as done in Ref. [147] does not suffice to provide accurate predictions for the short-lived collective resonances. In particular, the estimated Ξ_2 for the shorter-lived R_2 amounts to an error of 16.2 eV, which exceeds the discrepancy of Ξ_2 given by Wendin's work and our work. In our opinion, the most consequential approximation Wendin made lies not in the way he constructed the dielectric function ($\epsilon(E)$ obtained using RPAE is more accurate than what we can get using CIS), but in the way Wendin searched for the collective poles, which is suitable only for weakly damped oscillations (as they appear in, e.g., in metals) [160].

4.2.5 Evidence from a recent experiment at FLASH

Using the two complementary methods, we have rigorously demonstrated that the GDR of Xe bears a hidden substructure—there are in fact two collective dipole resonance states in the energy region above the $4d$ ionization threshold. Since this resonance-state substructure cannot be resolved using XUV linear spectroscopy (see Fig. 4.2), one may wonder if there is any other observable that is sensitive to it.

It turns out that this elusive correlated electronic structure can be probed by XUV non-linear spectroscopy. The evidence is provided by the recent two-photon ATI experiment at XUV-FEL FLASH [53], which we have alluded to in Sec. 1.3. Here, we briefly explain the results of Ref. [53].

Influence of the valence shell on the GDR substructure. There is one thing to mention before comparing the GDR substructure predicted in this work to the experimental results. In the calculations shown in 4.2.2 and 4.2.3, the active ionization channels lie in the $4d$ shell, and the outer $5s$ and $5p$ shells are frozen. This is an assumption made in Ref. [147] as well.

By lifting this restriction and reperforming the SES calculations, we find that including the $5s$ and $5p_{\pm m}$ channels leads to no qualitative but only minor quantitative modifications to the previous discussion. Hence, the Xe GDR mainly stems from the many-body correlations involving the ten $4d$ electrons [84], and the $5s$ and $5p$ electrons are only small admixtures. The Siegert energies for the three intrachannel resonances remain the same as in Table 4.1. In the full CIS model with active $4d$, $5s$, and $5p$ shells, the Siegert energies of R_1 and R_2 are

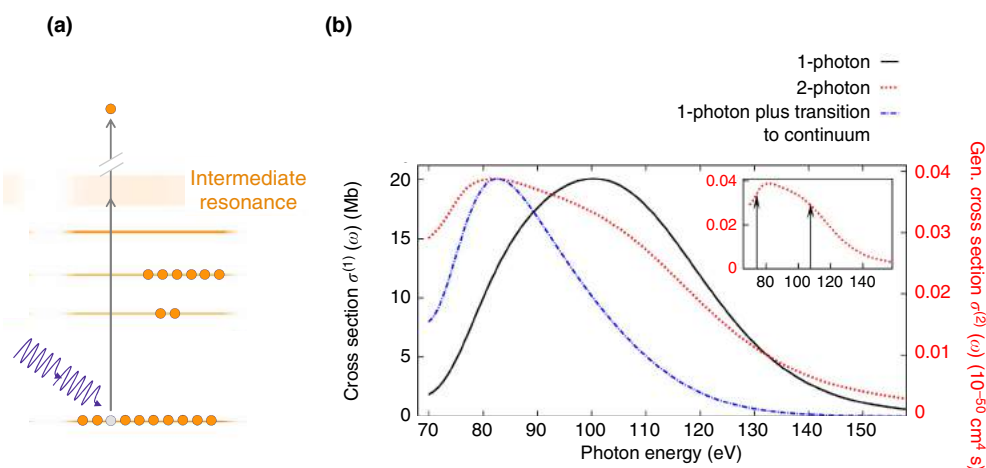


Figure 4.9. (a) Experimental scheme of the two-photon ATI experiment at FLASH. The quantitative agreement of photoemission yields between experimental data and TDCIS calculations at one of the two XUV photon energies can be found in Fig. 1.5(a). (b) Calculated (generalized) cross section as a function of the photon energy using the TDCIS approach: one-photon cross section (black solid line), two-photon cross section (red dotted line), and two-photon cross section based on the two-step model assuming one single intermediate resonance state (blue dash-dotted line). The inset shows the full two-photon cross section with two arrows indicating the excitation energies of the two sub-resonances calculated using the SES method. The figure is adapted from Ref. [53]. Copyright ©2015 Nature Publishing Group.

slightly revised to $(\Xi_1, \Gamma_1) = (73.4 \text{ eV}, 24.7 \text{ eV})$ and $(\Xi_2, \Gamma_2) = (111.8 \text{ eV}, 58.2 \text{ eV})$, respectively. Note that the higher-lying R_2 is more sensitive to the effects of the outer shells.

Experimental scheme and the theoretical modeling. The two-photon ATI experimental scheme employed in Ref. [53] is sketched in Fig. 4.9(a). Here, the first XUV photon promotes a $4d$ electron already above the ionization threshold, and the second XUV photon excites the electron further up into the continuum; the GDR is taken as an intermediate step of the sequential process. The two-photon electron yield is distinguished from the electron yields of other processes (i.e., $4d$ one-photon ionization, Auger decay, $5s$ and $5p$ one-photon ionization) by the kinetic energy of the ejected electron. The photoemission yield is recorded as a function of the FEL intensity at two selected photon energies, 105 eV and 140 eV.

As the experiment lies in the perturbative regime of light-matter interaction, the notion of (generalized) cross section is a suitable measure of the photoionization probability. The

one- and two-photon ionization cross sections are computed by solving the N -electron TDSE using TDCIS [53]. The cross sections are then fed into a set of coupled rate equations to determine the photoemission yields at various photon energies and intensities. Averaging over the spatial distribution of the beam profile is also performed. The theoretical results (scaled by a universal normalization factor) agree quantitatively with the experimental data. The comparison at the photon energy of 140 eV can be found in Fig. 1.5(a).

Interpretation of the two-photon cross section. After validating the full TDCIS model, one in turn comes back for an in-depth study on the calculated cross sections over a wide energy range. As shown in Fig. 4.9(b), in comparison with the one-photon cross section, the two-photon cross section is much broader and exhibits a prominent knee-type structure with two kinks.

The reason as to why the above two observations are a surprising one can be understood as follows. Within the framework of perturbation theory, if one assumes that there is one single intermediate resonance state in the GDR energy region, the two-photon cross section factorizes into a product of two one-photon cross sections [53]: the first one represents the transition from the ground state to the intermediate resonance, and the second one accounts for the transition from the resonance into final continuum states; the second step can be modeled by an energy dependence $E^{-13/2}$ [188]. According to this two step picture with one intermediate resonance, one expects a two-photon cross section that is narrower and shifted to a lower energy in reference to the one-photon cross section, because the cross section corresponding to the second step decrease monotonically with increasing energy. The two-photon cross section based on this simplified picture is also depicted in Fig. 4.9(b). Clearly, neither the width nor the knee-type structure of the full two-photon cross section can be explained by the two-step picture assuming one single resonance. This analysis provides strong evidence that there is more than one dipole-allowed resonance state residing in the energy range of the GDR. However, the exact number of resonances, their Siegert energies, and the collective nature can only be ascertained through the analysis presented in 4.2.2 and 4.2.3.

The inset of Fig. 4.9(b) plots the full two-photon cross section and the resonance positions predicted by the SES method. The resonance positions are consistent with the two kinks visible in the cross section (it is expected that the resonance positions will not exactly match the peak positions in the cross due to interference effects). Therefore, the combined results of Ref. [53], Wendin's pioneering work [147], and our work strongly support that the GDR is

in fact composed of two sub-resonances, whose substructure can be measured by exploiting the nonlinear response of Xe to intense XUV radiation.

4.3 Collective resonances in and beyond the linear-response regime

Motivation. In the previous section, we showed that there is more than one dipole-allowed, collective resonance state in the energy range of the GDR—that there are in fact two sub-resonances [52, 147]. The experiment at FLASH [53] based on XUV nonlinear spectroscopy provided strong evidence for this GDR substructure. The two-photon cross section in Ref. [53] exhibits a prominent knee-type structure with two kinks, which is in sharp contrast to the single smooth hump observed in the one-photon cross section [see Fig. 4.9(b)]. A question immediately surfaces: why is this resonance-state substructure, a key indicator of electronic correlations,^j hidden in linear spectroscopy, a central tool for our understanding of the collective behavior of Xe over the past half-century [29, 34, 82–86, 141, 144–148]?

Contributions of this thesis. In this section, we answer this question by resorting to the *fundamental electronic structure* using the concept of *resonance eigenstates*.^k We show that only one of the two sub-resonances can be resolved by linear spectroscopy, while the other is nearly invisible as a consequence of quantum interferences. Because the linear response of Xe only reveals *partial* information on the correlated electronic structure, there is no contradiction between the resonance substructure and the structureless hump in the one-photon cross section. In addition, we demonstrate how many-body effects result in the emergence of the two collective sub-resonances from the one-particle resonances. It turns out that the birthing process of the correlated electronic structure deviates substantially from what would be expected from conventional linear response theory. Furthermore, we predict the existence of hitherto unknown collective multipole resonance states of the $4d^{-1}\epsilon f$ type, the first unambiguous case of atomic plasmons on account of their comparatively long lifetimes. New prospects are now in sight for probing the multielectron dynamics of Xe with XUV nonlinear

^jIn the intrachannel model, there are no two far-separated dipole resonances; instead, there is only a group of three, close-lying resonances (see, e.g., Fig. 4.7).

^kBefore proceeding further, let us emphasize again what we mean by a resonance. In the theory of resonances, a resonance can be strictly identified as a discrete eigenstate of the Hamiltonian with a complex eigenenergy [77, 80, 121, 126, 127]. We therefore distinguish between a resonance in terms of the electronic structure and a resonance-like feature in the photoabsorption spectra; the latter is simply a possible manifestation of the former.

spectroscopy or attosecond metrology.

This work extends the literature on collective electronic excitations in and beyond atomic systems in two important ways. First, we provide a unique *bottom-up* approach to interpret the spectroscopic data of collective excitations. We study the collective resonance states *explicitly*, which enables an analysis of the cross sections on a state-by-state basis. Conversely, prior research adopts a *top-down* approach, where the resonance states are inferred from spectroscopic features [29, 34, 84–86]. Standard linear response theory applying advanced many-body techniques has made remarkable achievements in the quantitative description of the one-photon absorption data of the GDR [144–149]. Nevertheless, the fact that spectroscopic signals are knotty outcomes of quantum interferences among overlapping resonance and continuum states undermines their ability to reveal not only the full structural information but also the role of correlations in shaping the electronic structure.

Second, our study is, to the best of our knowledge, the first successful attempt to find collective multipole excitations in a realistic many-electron system. As far as experiment is concerned, the collective resonances of Xe under consideration are still confined to the dipole mode(s) [53, 76, 82, 83, 154, 156]. On the theory side, Ref. [189] examines the quadrupole transition matrix elements related to the $np^{-1}\epsilon f$ resonances of Xe in a many-body framework. Yet, as the number of np electrons is much less than that of $4d$, the resonances there are basically of one-particle origin [189]. Using a mean-field model, Ref. [190] peruses the generalized cross sections connected to the $4d^{-1}\epsilon f$ octupole resonance of Xe. According to the dipole case, it is no surprise that adding electronic correlations will shift the parameters of the noninteracting multipole resonances. What is unanticipated, however, is the direction in which these modifications unfold: as will be shown below, multielectron effects actually sharpen the widths of the $4d^{-1}\epsilon f$ multipole resonances of Xe inasmuch that they end up being at least 20 eV narrower than their dipole counterparts.

Methodology. Here, we choose to continue with the time-independent method used in the last section. That is, we diagonalize the field-free N -electron CIS Hamiltonian (see 2.2.2) subjected to complex scaling using SES (see 3.2.1). This is because this method gives complete information on the electronic structure in the energy region of interest—the energy eigenvalues as well as the many-electron wave functions can be obtained for both the resonance and the continuum states. Since we are interested in all types of resonances, we do not impose and relax the criterion $|(\Psi|\hat{D}_z|\Phi_0)| > 10^{-6}$ used in 4.2.3.

The numerical parameters used in this section are slightly different from those used in the

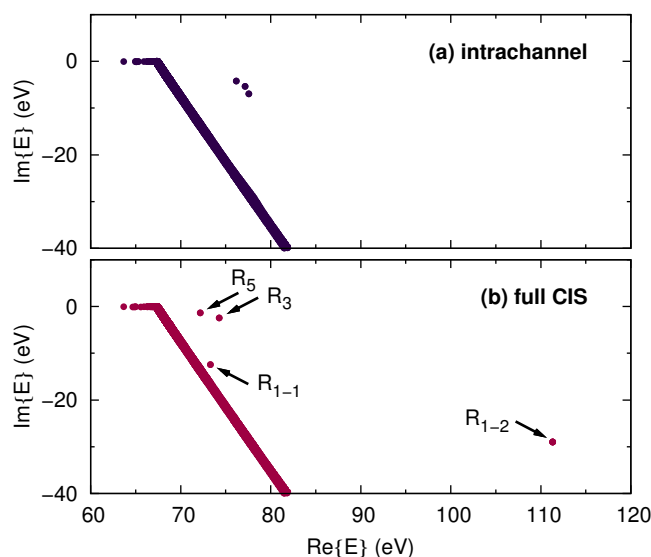


Figure 4.10. Complex energy spectra near the $4d$ threshold of Xe in (a) the intrachannel and (b) the full CIS models. Each filled circle symbolizes an eigenstate of the scaled N -electron Hamiltonian. Horizontal and vertical axes represent the real and imaginary parts of the energy eigenvalue, respectively. The figure is reproduced from Ref. [91]. Copyright ©2018 Y.-J.C. et al.

last section. In particular, we adopt a larger scaling angle to suppress the branching artifact in the complex energy spectrum (see Fig. 4.7) and to rotate the continuum further down into the complex energy plane. Active ionization channels include all the orbitals in the $4d$, $5s$, and $5p$ subshells. Further numerical details can be found in the original publication [91].

4.3.1 Characterization of the resonance states

Let us first characterize the fundamental electronic structure of interest, namely the $4d^{-1}\epsilon f$ resonance states of Xe.

Resonance eigenstates in the intrachannel model. Figure 4.10(a) presents the spectrum of the energy eigenvalues for the complex-scaled, non-Hermitian intrachannel Hamiltonian in close proximity to the $4d$ ionization threshold at 67.5 eV [104]. The result shown here is essentially the same as in Fig. 4.7: a group of three practically degenerate $4d_{\pm m}^{-1}\epsilon f_{\pm m}$ uncorrelated resonances can be observed, one for each $4d_{\pm m}$ channel. The tiny energy splitting hints at a slight dependency of the nonspherically symmetric one-particle potential on the hole alignment (characterized by the magnetic quantum number of the hole m_i).

Table 4.3. Siegert energies of the collective resonance states in the full CIS model. The energy values have an error bar of 0.5 eV, which is estimated by varying the SES parameters over a sensible range.

Label	Configuration	Ξ (eV)	Γ (eV)	Γ^{-1} (as)
R_{1-1}	$4d^{-1}\epsilon f(^1P)$	73.3	24.9	26.4
R_{1-2}	$4d^{-1}\epsilon f(^1P)$	111.3	58.0	11.4
R_3	$4d^{-1}\epsilon f(^1F)$	74.3	4.9	135.4
R_5	$4d^{-1}\epsilon f(^1H)$	72.2	2.8	237.4

Resonance eigenstates in the full CIS model. Figure 4.10(b) depicts the energy spectrum for the full CIS model, where four resonances are visible. Clearly, the resonance substructure critically hinges on the two-body Coulomb interactions. The Siegert energies of the exposed resonances are detailed in Table 4.3. Each resonance state here has a definite total orbital angular momentum quantum number L . R_{1-1} and R_{1-2} [$4d^{-1}\epsilon f(^1P)$] are the two dipole sub-resonances in the spectral range of the GDR.¹ R_3 [$4d^{-1}\epsilon f(^1F)$] and R_5 [$4d^{-1}\epsilon f(^1H)$] were so far unknown and can be accessed only via multiphoton absorption. The 1D and 1G resonances are absent owing to the restrictions imposed on \mathbb{V}_{CIS} . Assuming electric dipole transitions for linearly polarized radiation [111], a closed-shell ground state is allowed to go to an odd-parity excited state with only an odd L . The hole population in each resonance state [44] is primarily distributed among different $4d_{\pm m}^{-1}$, with small admixtures of $5s_0^{-1}$ and $5p_{\pm m}^{-1}$ from the outer shell [29, 52, 84].

There are different ways to define if a resonance corresponds to a collective excitation. The first way is based on the importance of correlations for the quantitative description of the resonance parameters [84]—the resonances here satisfy this condition. Another way is based on whether the resonance wave function can be written as a superposition of various 1p-1h configurations [161]. For the dipole resonances R_{1-1} and R_{1-2} , we have shown that they meet this requirement (see Tab. 4.2). For the multiple resonances R_3 and R_5 , the same conclusion will be drawn in the next subsection.

4.3.2 Many-body effects on the emergence of the correlated electronic structure

To elucidate the role of correlations in shaping the one-particle into the many-body resonance substructure, Fig. 4.11 illustrates how an eigenstate in the intrachannel model evolves into one in the full CIS model upon adiabatic switching of multielectron interactions. Briefly,

¹ R_{1-1} and R_{1-2} were labeled as R_1 and R_2 , respectively, in the previous section. Here, another number is added to the index to emphasize that those two are dipolar resonances.

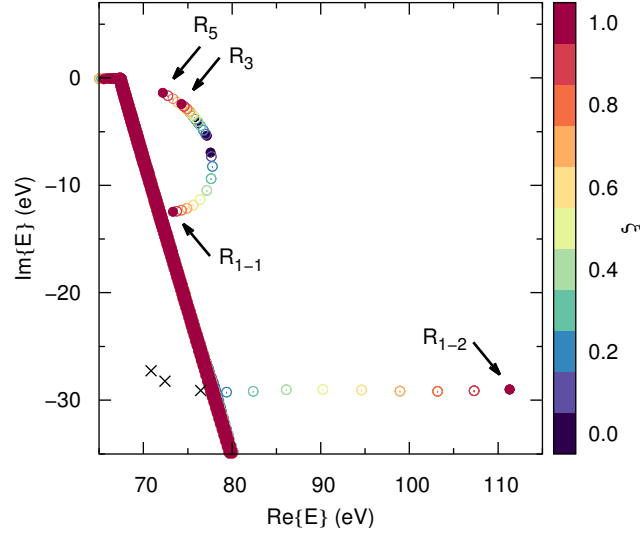


Figure 4.11. Evolution of the complex energy spectrum from the intrachannel to the full CIS model. The interchannel-coupling strength ξ is represented by the false color. Locations of the unexposed intrachannel resonances are indicated by black crosses. The figure is reproduced from Ref. [91]. Copyright ©2018 Y.-J.C. et al.

we diagonalize the Hamiltonian gradually varying the strength of the interchannel-coupling terms $\xi(\Phi_j^b|\hat{H}_1|\Phi_i^a)$, $\xi \in [0, 1]$ ($i \neq j$). The intrachannel model is equivalent to the case where $\xi = 0$, and the full model to the case where $\xi = 1$.

Correlation effects on the exposed intrachannel resonance group. First, we focus on the upper-left corner of Fig. 4.11. As ξ increases, the three intrachannel resonances turn into R_{1-1} , R_3 , and R_5 in the full model. At first sight, one might picture this as multiplet splitting in the subspace spanned by the three one-particle resonances. However, the formation of R_{1-1} , R_3 , and R_5 is far more complicated than that and requires configuration mixing among the intrachannel resonance and continuum states. A simple way to see this is that the eigenvalues of the reduced 3×3 Hamiltonian with off-diagonal interchannel couplings must analytically add up to a constant for an arbitrary ξ , whereas the sum of the Ξ 's for these three poles is obviously not conserved. Therefore, the appearance of R_{1-1} , R_3 , and R_5 involves more than the pure coupling of the three nearly degenerate $4d_{\pm m}^{-1} \epsilon f_{\pm m}$ intrachannel resonance states, and the wave functions of R_{1-1} , R_3 , and R_5 must be expressed as a sum over 1p-1h configurations with different energies. This wave function perspective [161] (in addition to the perspective of resonance parameters [84]) emphasizes again that they correspond to a collective

resonance state.

Interestingly, multielectron effects are particularly strong on the widths of the members of this resonance group, resulting in anomalous segregation (at least 20 eV in terms of Γ) of the broad dipole mode and the two narrow multipole modes. To date, no *sustained* collective excitation in atoms, or “atomic plasmon”, has been found [85]—it always carries charge density oscillations damping out more or less within a period [84, 85]. As R_3 and R_5 represent *collective* and *weakly damped* oscillations (with $\Xi/\Gamma > 15$), they may be called “atomic multipole plasmons” and are expected to give rise to distinctive signatures in XUV nonlinear spectroscopy [191–193] or attosecond pump-probe experiments [15].

Correlation effects on the unexposed intrachannel resonance group. Next, let us look at the lower part of Fig. 4.11. When turning on couplings, the very broad resonance R_{1-2} emerges from the continuum, retains its width, and quickly becomes fairly isolated in the energy plane. The emergence of R_{1-2} does not mean that correlations create an additional resonance pole. Instead, it signals that the intrachannel potential can support another group of $4d_{\pm m}^{-1} \epsilon f_{\pm m}$ uncorrelated resonances with $\text{Re}\{E\} \approx 70$ eV, $\text{Im}\{E\} \approx -30$ eV (see the black crosses in Fig. 4.11) that is not exposed by the scaling angle chosen for the figures. With the angle used, these unexposed resonances are embedded in the intrachannel continuum close to $\text{Im}\{E\} = -30$ eV.^m

The two dipole sub-resonances R_{1-1} and R_{1-2} in the GDR region can be adiabatically traced back to two separate groups of one-particle resonances, whose existence was not known before. Note that it is rather unusual that a potential supports two resonance groups with distinct widths but similar excitation energies [80, 121]. Ergo, the question naturally follows as to which properties of the one-particle potential are necessary for the presence of such a double-pole structure. This nontrivial question will be answered in the following subsection.

^mIn Figs. 4.10 and 4.11, we already use a rather large scaling angle $\theta = 36^\circ$. In order to expose the second group of intrachannel resonances (indicated by the black crosses in Fig. 4.11), we need to use an even larger angle $\theta = 44^\circ$. The reason why we keep the second group unexposed here is because such a large scaling angle, while having little influence on the Siegert energies, does impair the quality of the resonance and continuum wave functions and thus the quality of the photoabsorption cross sections, which will be analyzed later in 4.3.4. For numerical consistency, we therefore do not explicitly expose the second group of intrachannel resonances.

4.3.3 Properties of the double-pole structure in the noninteracting limit

The double-pole structure in our noninteracting model, i.e., the exposed and the unexposed intrachannel resonance groups in Fig. 4.11, comes as a surprising result. First, since there is only one resonance-like feature visible in one-particle linear absorption spectrum (see Fig. 4.2), its presence was previously unknown. Second, it is rather unusual that a potential can support various resonance groups with distinct decay widths yet similar excitation energies [80, 121]. Following this observation, we hence investigate the properties of the one-particle potential necessary for the existence of such a double-pole structure. This is also a first step towards understanding the different roles collectivity plays in forming R_{1-1} and R_{1-2} , respectively.

Methodology. We do not explicitly construct the effective one-particle potential here. Nevertheless, the properties of the potential can be tuned implicitly by manipulating the intrachannel-coupling Coulomb matrix elements [41, 45]. Within CIS, the part of the N -body Hamiltonian that contains the residual electron-ion interactions beyond the description of the MF HF potential is [41, 45]

$$\hat{H}_1 = \frac{1}{2} \sum_{\substack{n,n'=1 \\ n \neq n'}}^N \frac{1}{|\hat{\mathbf{r}}_n - \hat{\mathbf{r}}_{n'}|} - \sum_{n=1}^N \hat{v}_{\text{MF}}. \quad (4.14)$$

In the intrachannel model, we consider only the matrix elements of the type $(\Phi_i^b | \hat{H}_1 | \Phi_i^a)$. This one-body part of \hat{H}_1 gives rise to the picture of an excited electron moving in the presence of an attractive ionic potential [41, 45].

In the following, we analyze two scenarios that impose further restrictions on the intrachannel-coupling terms. Because the behaviors of different $4d_{\pm m}$ ionization channels are much alike, we only show the results for the $4d_{\pm 1}$ channel.ⁿ

Importance of the ionic potential. In the first scenario, we simply switch off the residual intrachannel Coulomb interactions, so the one-particle potential reduces to the HF potential of a neutral Xe atom.

ⁿThe calculations are done using a scaling angle of $\theta = 44.5^\circ$, which can directly expose both resonance groups in the intrachannel model. This is also the largest possible scaling angle for our SES procedure: any scaling angle bigger than that will lead to noticeable perturbation of the Xe ground state.

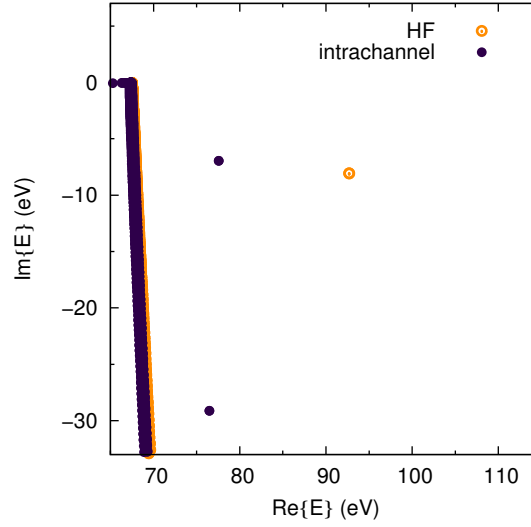


Figure 4.12. Comparison between the complex energy spectrum in the HF model and that in the intrachannel model. The figure is reproduced from Ref. [91]. Copyright ©2018 Y.-J.C. et al.

Figure 4.12 shows the comparison between the SES energy spectrum in the HF model and that in the intrachannel model. The intrachannel model gives rise to the double-pole structure, while the HF model predicts only one $4d_{\pm 1}^{-1}\epsilon f_{\pm 1}$ resonance. Apparently, the double-pole structure, or more specifically the shorter-lived resonance, cannot be captured by the short-range potential of neutral Xe and requires the long-range potential of Xe^+ . In the next step, we divide the ionic potential into various components and then discuss their individual influences.

Importance of the exchange ionic potential. To tackle the Coulomb integrals in Eq. (4.14), we perform the multipole expansion [44]:

$$\hat{r}_{1,2}^{-1} =: \frac{1}{|\hat{\mathbf{r}}_1(r_1, \theta_1, \phi_1) - \hat{\mathbf{r}}_2(r_2, \theta_2, \phi_2)|} = \sum_{L=0}^{\infty} \frac{4\pi}{2L+1} \frac{r_{<}^L}{r_{>}^{L+1}} \sum_{M=-L}^L Y_{L,M}^*(\theta_1, \phi_1) Y_{L,M}(\theta_2, \phi_2), \quad (4.15)$$

where the $r_{<} = \min\{r_1, r_2\}$ and $r_{>} = \max\{r_1, r_2\}$.

In the intrachannel model, the direct Coulomb matrix elements read [43, 45]:

$$v_{(b,i,a,i)} = \left(\phi_b(\hat{\mathbf{r}}_1) \phi_i(\hat{\mathbf{r}}_2) \left| \hat{r}_{1,2}^{-1} \right| \phi_a(\hat{\mathbf{r}}_1) \phi_i(\hat{\mathbf{r}}_2) \right), \quad (4.16)$$

and the exchange terms read [43, 45]:

$$v_{(b,i,i,a)} = \left(\phi_b(\hat{\mathbf{r}}_1) \phi_i(\hat{\mathbf{r}}_2) \left| \hat{r}_{1,2}^{-1} \right| \phi_i(\hat{\mathbf{r}}_1) \phi_a(\hat{\mathbf{r}}_2) \right). \quad (4.17)$$

In these expressions, ϕ_i denotes a hole orbital occupied in the HF ground state, and ϕ_a and ϕ_b symbolize virtual orbitals of the excited electron [43]. The angular parts of the orbitals are expressed in terms of spherical harmonics [44].

Let us simply analyze the angular parts of the matrix elements. Inserting Eq. (4.15) into Eqs. (4.16) and (4.17) respectively, we obtain the following relationships:

$$\begin{aligned} & \text{Angular part of the } L\text{-th order term of } v_{(b,i,a,i)} \\ & \propto \langle Y_{l_b, m_b} | Y_{L, M}^* | Y_{l_a, m_a} \rangle \langle Y_{l_i, m_i} | Y_{L, M} | Y_{l_i, m_i} \rangle, \end{aligned} \quad (4.18)$$

and

$$\begin{aligned} & \text{Angular part of the } L\text{-th order term of } v_{(b,i,i,a)} \\ & \propto \langle Y_{l_b, m_b} | Y_{L, M}^* | Y_{l_i, m_i} \rangle \langle Y_{l_i, m_i} | Y_{L, M} | Y_{l_a, m_a} \rangle. \end{aligned} \quad (4.19)$$

For an f -wave intrachannel resonance of a specific $4d_{m_i}$ channel, $l_i = 2$, $l_a = l_b = 3$, and $m_i = m_a = m_b$. According to the addition of angular momenta, we only have to consider the cases with $M = 0$. More importantly, due to the parity of spherical harmonics, the direct terms are nonzero only for an even L , and the exchange terms are nonzero only for an odd L . Thus, as one carries out a multipole expansion of the intrachannel Coulomb matrix elements, not only does one divide the photoelectron-ion interactions based on the angular features, but one also separates the local direct part of the ionic potential from the nonlocal exchange part.

Figure 4.13 illustrates the emergence of the double-pole structure in the intrachannel model when including up to the L_{\max} -th order term in the multipole expansion of the intrachannel Coulomb matrix elements. With exclusively the monopolar $L = 0$ term, the leading order contribution of the direct interactions, there is only the longer-lived uncorrelated resonance but not the shorter-lived one. However, as soon as one adds in the dipolar $L = 1$ term, the leading order contribution of the exchange interactions, the double poles with almost the same $\text{Re}\{E\}$ but very different $\text{Im}\{E\}$ immediately spring up. Putting in even higher order terms only causes small perturbations of the Siegert energies of the two resonances, which are converged for $L \geq 5$.

The above observation suggests that the appearance of the double-pole structure in the one-particle limit is an immediate consequence of the exchange part of the ionic potential, which enters the intrachannel Coulomb matrix elements ($\Phi_i^b | \hat{H}_1 | \Phi_i^a$) to leading order through a dipolar term. Due to the sensitivity to such nonlocality, the origin of the double-pole structure cannot be explained by the standard notion of shape resonances and local potential barriers [29] and thus remains nontrivial. As a final remark, we point out that the monopolar

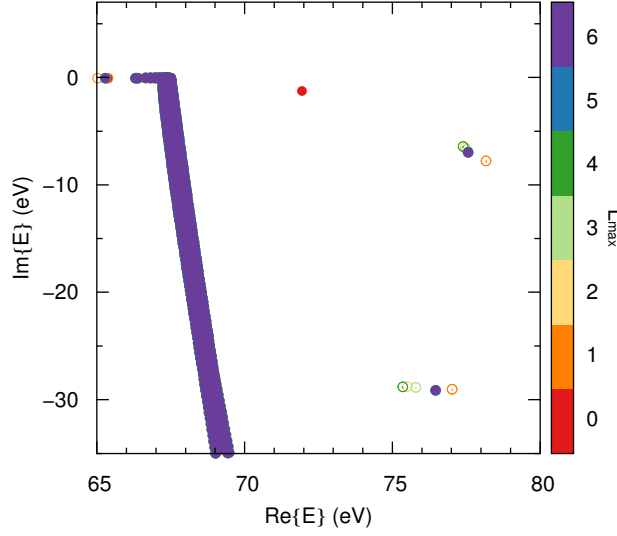


Figure 4.13. Evolution of the complex energy spectrum when including up to the L_{\max} -th order term in the multipole expansion of the intrachannel-coupling Coulomb matrix elements. The parameter L_{\max} is indicated by the false color. The double-pole structure emerges upon $L_{\max} = 1$. The figure is reproduced from Ref. [91]. Copyright ©2018 Y.-J.C. et al.

component of the ionic potential, which represents a simple central field $V(r)$, is insufficient for the description of the double-pole structure.

4.3.4 State-by-state analysis of the one-photon absorption spectrum

So far, our discussion has been centered on the fundamental $4d^{-1}\epsilon f$ resonance eigenstates of Xe. We now elaborate how the intrinsic electronic structure is mapped onto spectroscopic features in the photoabsorption spectra. We start by showing how to dissect the one-photon cross section associated with the GDR in a bottom-up, state-resolved manner.

Bottom-up analysis of the cross section. The total one-photon absorption cross section can be constructed from the bottom up, making use of the eigenstates of the complex-scaled N -body Hamiltonian [194, 195]:

$$\sigma_{\text{tot}}(\omega) = -4\pi\alpha\omega \text{Im} \sum_n \frac{D_n^2}{\omega - E_n} =: \sum_n \sigma_n(\omega), \quad (4.20)$$

where α is the fine structure constant, $D_n := (\Phi_n | \hat{D}_z | \Phi_0)$ is the dipole transition matrix element from the initial HF ground state $|\Phi_0\rangle$ to an excited state $|\Phi_n\rangle$ along the polarization axis z ,

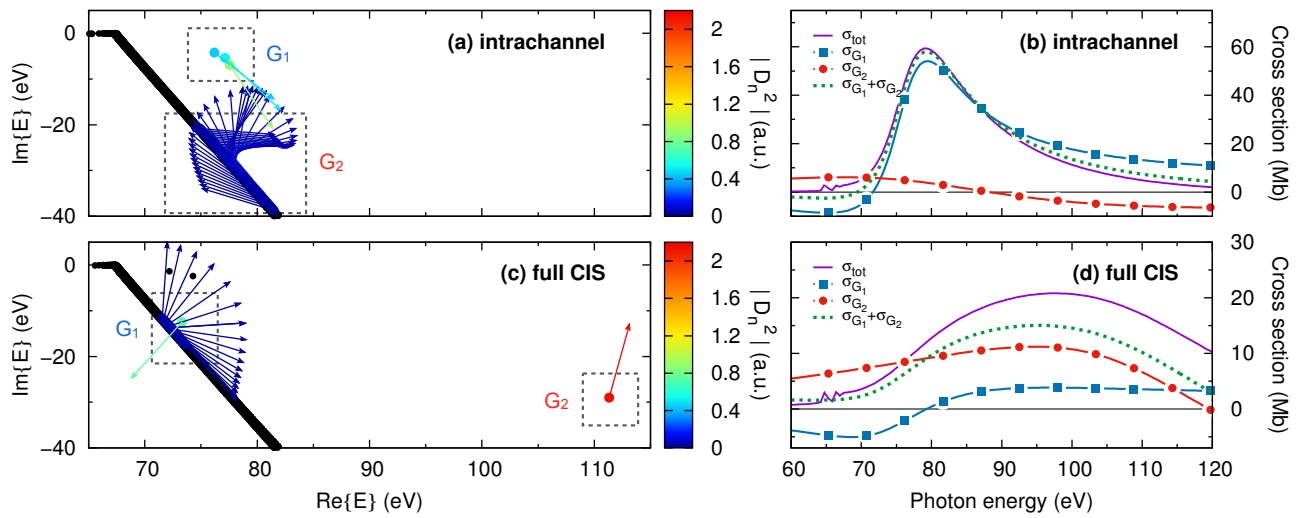


Figure 4.14. Left panels: Distributions of D_n^2 in (a) the intrachannel and (c) the full CIS models. Each state with $|D_n^2| > 0.016$ is represented by a filled circle and a vector of constant length. The amplitude $|D_n^2|$ is indicated by the false color, and the phase $\arg\{D_n^2\}$ is indicated by the angle of the vector with respect to the real energy axis. Other states with $|D_n^2| \leq 0.016$ are represented by smaller black dots. Right panels: Total cross sections and effective cross sections for states in various energy regions in (b) the intrachannel and (d) the full CIS models. The figure is reproduced from Ref. [91]. Copyright ©2018 Y.-J.C. et al.

and $\sigma_n(\omega)$ defines the corresponding individual cross section. Eq. (4.20) enables one to dissect the total cross section into the contributions of various final-state components. More importantly, thanks to complex scaling, each resonance state has a clear-cut contribution, since it is associated with one eigenfunction of the scaled Hamiltonian, rather than with a collection of continuum states of the unscaled Hamiltonian.

Note that, as a result of non-Hermiticity, Eq. (4.20) has some features that may look unfamiliar in comparison to standard Hermitian quantum mechanics. First, D_n is the dipole matrix element in the *symmetric* inner product form (\cdot, \cdot) rather than in the Hermitian form $\langle \cdot, \cdot \rangle$ [77, 121] (see 3.2.3). Second, since $\sigma_n(\omega)$ depends on D_n^2 instead of $|D_n|^2$, it generally has a *Fano* lineshape. Because of the energy denominator $(\omega - E_n)$ in Eq. (4.20), the $\sigma_n(\omega)$ of the states lying close to each other in the complex energy plane are expected to undergo strong interferences and should be analyzed as a group together.

The total cross sections in the intrachannel and the full CIS models obtained using this time-independent method [see $\sigma_{\text{tot}}(\omega)$ in Figs. 4.14(b) and (d)] are in excellent quantitative agreement with those evaluated using a time-dependent CIS method without complex scaling [51]. This verifies that SES does not perturb the wave functions in the physical inner region, where photoabsorption and particle-hole interactions happen. Note that our intrachannel $\sigma_{\text{tot}}(\omega)$ bears resemblance to Cooper's one-particle spectrum in Fig. 4.2. Also, there is reasonable quantitative agreement between the full CIS $\sigma_{\text{tot}}(\omega)$ and the experimental data [51].

One-photon cross section in the intrachannel model. Figure 4.14(a) displays the distribution of the squared dipole matrix elements D_n^2 in polar form for the intrachannel eigenstates.^o For clarity, only those with $|D_n^2| > 0.016$ are shown. The dipole strengths cluster around two separate regions G_1 and G_2 in the complex energy plane. We thereupon analyze the effective cross section for all the states in each region, where their individual $\sigma_n(\omega)$ overlap notably and undergo strong constructive or destructive interferences depending on the relative dipole phases.

In the first region G_1 lie only the exposed intrachannel resonances. As their D_n^2 are large

^oTo construct the total one-photon absorption cross sections $\sigma_{\text{tot}}(\omega)$ in Figs. 4.14(b) and (d), we include the contributions of all the eigenstates with an excitation energy between 60 and 200 eV. We evaluate the dipole transition matrix elements D_n using the dipole operator in the velocity form [43]. As shown by a CIS wave-packet calculation without complex scaling, the velocity form predicts a one-photon absorption spectrum in closer agreement with the experimental data [51].

in amplitude and nearly identical in phase, their σ_n interfere constructively and bring a net contribution $\sigma_{G_1}(\omega)$ that governs the narrow peak at 80 eV in $\sigma_{\text{tot}}(\omega)$ [Fig. 4.14(b)]. In the second region G_2 are the continuum states with $\text{Im}\{E\} \approx -30$ eV. Owing to the rapid phase variation in D_n^2 , the σ_n of those states interfere destructively. Accordingly, the effective $\sigma_{G_2}(\omega)$, which implicitly contains the contributions from the unexposed intrachannel resonances, practically plays no part in σ_{tot} . All the other states with $|D_n^2| \leq 0.016$ cause the minute difference between $\sigma_{G_1} + \sigma_{G_2}$ and σ_{tot} .

One-photon cross section in the full CIS model. Figure 4.14(c) is the distribution of the D_n^2 for the eigenstates in the full CIS model. Similar to the intrachannel case, the dipole strengths here are also concentrated in two regions. The first region G_1 encompasses R_{1-1} and the neighboring continuum states. If one assigns a net transition dipole to the continuum states, it roughly has half of the amplitude and points in the opposite direction in comparison to that of R_{1-1} . Due to this destructive interference, all the states in G_1 jointly produce a weak asymmetric background $\sigma_{G_1}(\omega)$ in $\sigma_{\text{tot}}(\omega)$ [Fig. 4.14(d)]. In the second region G_2 resides merely one eigenstate, R_{1-2} . For R_{1-2} has a large transition dipole and is very isolated, its own characteristic feature $\sigma_{G_2}(\omega)$ stands out without much interference and provides the major contribution to the broad hump around 100 eV in σ_{tot} . The discrepancy between $\sigma_{G_1} + \sigma_{G_2}$ and σ_{tot} mostly stems from the continuum states with $\text{Im}\{E\} \lesssim -30$ eV.

Discussion of the cross-section analysis. At this stage, it becomes evident that the linear response of Xe does not reveal the full landscape of the dipole-accessible electronic structure in the 4d continuum. In experimental [82, 83] and conventional theoretical [29, 34, 84–86, 141, 144–149] studies, resonance states are known in an implicit, top-down manner—they are inferred from features in the photoabsorption spectrum. Such indirectness explains why the dipole-allowed resonance substructure is unbeknownst to linear spectroscopy. Because of the interferences among overlapping eigenstates, only the exposed resonance group is visible in the intrachannel total one-photon cross section, and only the broader dipole sub-resonance R_{1-2} shows up as the GDR in the full CIS cross section.

In both the one-particle and the many-body one-photon absorption spectra, there is only one smooth, structureless resonance-like feature. As such, the energy up-shift and the broadening of the maximum in $\sigma_{\text{tot}}(\omega)$ upon the inclusion of multielectron interactions have long been interpreted, since the seminal work of Cooper in 1964 [141], as a correlation-induced modification of the Siegert energy of one single resonance state [141, 144–148]. Per contra,

we find that these spectroscopic changes actually arise from switching the visibilities of two distinct resonance groups without any adiabatic connection. Whereas interchannel couplings suppress the fingerprint of the exposed intrachannel resonances by moving R_{1-1} downward in the energy plane and introducing destructive interferences with nearby continuum states, they enhance the feature of the unexposed ones by moving R_{1-2} horizontally away from the continuum and eliminating destructive interferences.

4.3.5 Three-photon–two-color scheme for probing the collective octupole resonance

We have analyzed the optical response attributable to the $4d$ dipole resonances of Xe. We now present an effective three-photon–two-color scheme that is designed specifically to unveil the response of the collective octupole resonance R_3 predicted in this work. Our proposal may be realized with a combination of XUV FELs [191, 192] and lower-order HHG sources [193]. This two-color scheme has the advantage of its target selectivity: it has been shown that, on a mean-field level, a simpler three-photon–one-color scheme excites the Xe ground state predominantly to the final states with $4d^{-1}\epsilon f(^1P)$, but not to those with $4d^{-1}\epsilon f(^1F)$ [190].

Proposed three-photon–two-color scheme. The proposed three-photon–two-color scheme is sketched in Fig. 4.15(a). In the first step, the ground state is promoted to the lowest $4d^{-1}nd(^1D)$ Rydberg state at 64.8 eV through two-photon resonant excitation. This requires an intense, yet perturbative XUV source with a photon energy of 32.4 eV and a sub-eV bandwidth in order to avoid the excitation of other bound states with even parity. In the second step, the $4d^{-1}nd(^1D)$ state absorbs one photon with a different color and goes to R_3 [$4d^{-1}\epsilon f(^1F)$]. This necessitates a weak source at a photon energy of 9.5 eV in the VUV. The target specificity of our scheme is rationalized by the fact that the lowest $4d^{-1}nd(^1D)$ state has the strongest dipole transition matrix element to R_3 as compared to all the other states lying above the $4d$ ionization threshold.

Proof-of-concept cross-section calculations. As a proof of concept, we assume that the first excitation step generates a system in a pure state of the lowest $4d^{-1}nd(^1D)$ state. The total one-photon absorption cross section corresponding to the second step can then be calculated

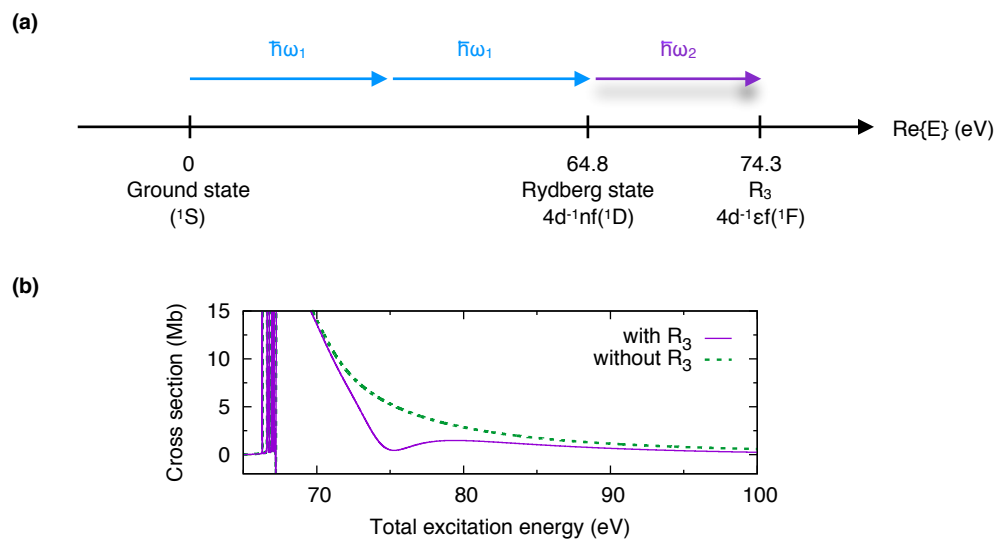


Figure 4.15. (a) Schematic view of the proposed three-photon–two-color scheme for the probing of the collective octupole resonance R_3 . The axis represents the excitation energy, $\text{Re}\{E\}$, of each underlying state. An XUV photon is indicated by a blue arrow (“ $\hbar\omega_1$ ”); a (tunable) VUV photon is indicated by a purple arrow (“ $\hbar\omega_2$ ”). (b) One-photon cross sections with (purple solid line) and without (green dashed line) the contribution of R_3 as a function of the total three-photon excitation energy relative to the Xe ground state, as a function of $(64.8 \text{ eV} + \hbar\omega_2)$, where 64.8 eV is the excitation energy of the lowest $4d^{-1}nd(^1D)$ Rydberg state. Part of the figure is reproduced from Ref. [91]. Copyright ©2018 Y.-J.C. et al.

by substituting the $4d^{-1}nd(^1D)$ wave function for $|\Phi_0\rangle$ in Eq. (4.20).^p

Figure 4.15 plots the one-photon cross sections with and without the contribution of R_3 as a function of the total three-photon excitation energy relative to the Xe ground state.^q Comparison between the two spectra verifies that the window resonance close to 75 eV originates precisely from the target R_3 .

Note that as the current XUV FELs [191, 192] have a typical pulse duration longer than the Auger decay time of $4d^{-1}$ [118], the XUV and VUV pulses have to overlap in time. Experimentally, this requires the two pulses to be synchronized with femtosecond accuracy. Photoelectron spectroscopy can help to disentangle the signal of R_3 from the background due to XUV or VUV absorption of the valence electrons. The kinetic energy of the photoelectron associated with the final state R_3 is 6.8 eV. Close to this energy, XUV one-photon ionization of the 5s subshell can yield a photoelectron carrying a kinetic energy of 9.1 eV. By further measuring the angular-resolved photoelectron distribution, it is feasible to separate the contribution of the target (with an f -wave character) from that of the background (with a p -wave character). On the theory side, the temporal overlap of the two pulses means that further studies on the cross section that take into account the effects of virtual excitations are expected to improve the quantitative details presented here.

4.4 Summary

The key messages of this chapter are summarized as follows:

- ◇ We disentangle two fundamental collective dipolar resonance states that are hidden in the one-photon cross section associated with the Xe GDR. Our study is the first that rec-

^pThere are two possible ways to go beyond such proof-of-concept calculations. First, one can generalize the expression in Eq. (4.20) from the one-photon to the three-photon case. This extension, which has not yet been developed, must be expected to be quite nontrivial, as the result cannot be intuitively inferred from the expression used in standard Hermitian quantum mechanics. Instead, one will need to perform the perturbation analysis up to the sixth order within the non-Hermitian framework. Alternatively, one can calculate the three-photon cross section using time-dependent wave-packet propagation techniques. However, this will not allow one to selectively include and exclude the contribution of R_3 as done in this subsection.

^qHere, we change the value of an SES parameter, r_0 [see Eq. (3.17)]. The value $r_0 = 8$ a.u. used for Figs. 4.10, 4.11, and 4.14 perturbs the lowest $4d^{-1}nd(^1D)$ Rydberg state in the three-photon–two-color scheme. For Fig. 4.15, we therefore use a more moderate $r_0 = 20$ a.u.. This also makes sure that the collective multipole resonances predicted in this work are independent of the numerical parameters and are thus not numerical artifacts.

ognizes and fully characterizes the GDR substructure; it extends Wendin's pioneering work, without invoking the approximation that is only applicable to weakly damped oscillations (Sec. 4.2).

- ◇ The detailed theoretical characterization of the GDR substructure is achieved consistently by two complementary methods implemented within the (TD)CIS framework. The wave-packet-based Gabor method generalizes the standard Fourier analysis to the combined time-frequency domain, such that strongly overlapping resonances living on different time scales can be more easily separated. The eigenstate-based SES method demonstrated here is the first example of treating collective resonances using the complex scaling technique; it gives access to the resonance wave functions and thus allows a transparent interpretation of the two resonances as new collective modes.
- ◇ This GDR substructure, albeit invisible in XUV linear spectroscopy, has gained strong evidence from the recent experiment at FLASH using XUV nonlinear spectroscopy.
- ◇ Continuing using the SES method, we approach all types of collective resonances in the Xe $4d$ shell, including the dipole as well as multiple resonances, from a new perspective: we directly tackle the resonance eigenstates at the most fundamental level—that of the correlated electronic structure, and then connect them to their spectroscopic manifestations. By explicitly tracking the adiabatic evolution of the resonance states, we demonstrate the diverse role of electronic correlations in the formation of various types of $4d^{-1}\epsilon f$ collective resonances (Sec. 4.3).
- ◇ In the dipole-resonance case, by examining the one-photon cross section in a bottom-up, state-resolved fashion, we show that linear spectroscopy captures only partial information of the GDR substructure as a result of quantum interferences. Moreover, we show that, when going from Cooper's one-particle spectrum to the experimental data, the spectroscopic changes cannot be obtained by adding correlations to one resonance eigenstate; they are signatures of swapping the visibilities of two individual resonances without any adiabatic connection. In doing so, we explain why standard top-down, linear-response-type theoretical studies reveal very limited (or even biased) information on the many-body nature of the GDR.
- ◇ Going beyond the dipole-allowed correlated electronic structure, we predict the existence of collective multipole resonances of Xe. Unlike any known collective feature in atoms, these resonances live exceptionally long (more than 100 attoseconds). They

thus provide a new playground for studying the collective nonlinear response of Xe using advanced light sources in either spectral or temporal domain.

Chapter 5

Application II: Subcycle strong-field–ionization dynamics of Xe

Now we present the second application of the theories elucidated in Chapters 2 and 3 to the study of ultrafast electronic resonances in atomic Xe. In this chapter, we investigate the resonance that appears during nonperturbative NIR photoionization in the Xe 5*p* valence shell; the resonance is not only short-lived but also evolves on an ultrafast time scale.

This chapter is organized as follows. Sec. 5.1 introduces the SFI process, a process of both

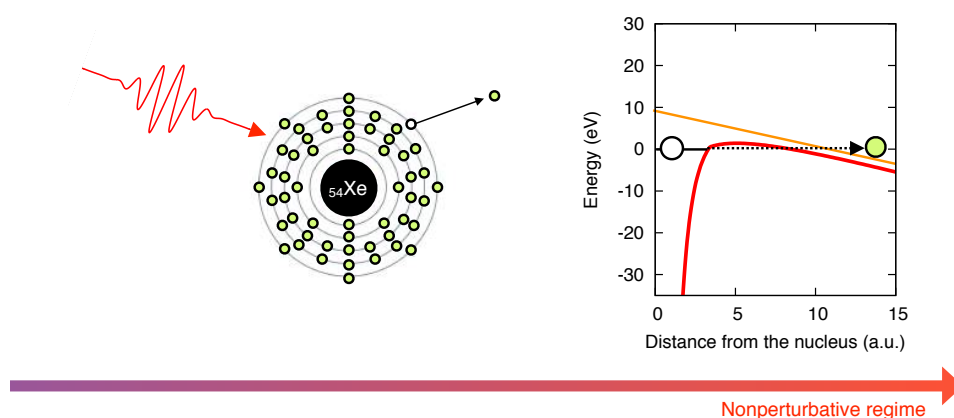


Figure 5.1. Topic of this chapter: short-lived resonance in NIR nonperturbative photoionization of the Xe 5*p* shell in a time-dependent setting. For detailed description of the figure see the caption of Fig. 1.7(b). The main results presented here have been published in *Nature Physics* **13**, 472 (2017) [60], a selected science highlight in *DESY Photon Science Annual Report 2017*.

fundamental and technological importance. Sec. 4.2 shows how we look into the subcycle SFI dynamics of Xe using an attosecond pump-probe spectroscopic technique; the quantitative capability of TDCIS is exemplified by comparing the experimental data to the simulated results. In Sec. 4.3, TDCIS is used to reveal the physical origin of an unexpected oscillatory feature of the observed SFI dynamics, which comes from a commonly overlooked facet of the strong-field–induced tunneling resonance state. Sec. 5.4 summarizes the chapter.

5.1 Introduction

Introduction. Ionization in the presence of an intense laser field can occur either through a multiphoton-mediated process (multiphoton ionization, MPI), where the missing energy to surpass the ionization barrier is provided by the simultaneous absorption of multiple photons, or by electron tunneling through a field-induced potential barrier when the laser electric field significantly alters the binding potential (strong-field ionization, SFI) (see Sec. 1.2). An example of such a field-dressed potential for Xe is plotted in Fig. 5.1, where we employ the HFS potential with the Latter tail correction [143] to describe the Xe atom and the length gauge to describe the laser-atom interaction (see 2.1.2).

The relative contribution of the two ionization pathways is commonly classified by the Keldysh parameter $\gamma = \omega_L \sqrt{2I_p m_e} / (|e|E_L)$, where ω_L is the frequency of the laser, I_p is the ionization potential, E_L is the laser electric field and $|e|$, m_e are the charge and mass of the electron, respectively [8, 28]. This classification concept can be understood by considering the time the electron needs to tunnel through the combined Coulomb-laser potential barrier [22, 23]. For a low-frequency laser field with high intensities ($\gamma \ll 1$), the electron is given enough time to overcome the field-induced barrier before the potential significantly changes. In this quasistatic regime, tunneling dominates over multiphoton ionization. Conversely, in the limit of high frequencies and low intensities ($\gamma \gg 1$), tunneling is suppressed by the decreased tunneling time window and the increased barrier width. In this nonquasistatic regime, ionization by the absorption of several photons is favored.^a

^aThe above classification can be viewed from two interconnected perspectives: the time perspective and the energy perspective (see Sec. 1.2). These two points of view, respectively, give the $\gamma \ll 1$ regime two different names: quasistatic regime (time perspective) and nonperturbative regime (energy perspective). In the literature, the term “adiabatic regime” is also commonly used [22, 23]. We point out that the concept of adiabaticity [93] in terms of the *instantaneous field-dressed eigenstates* in fact does not hold when $\gamma \ll 1$: during SFI, the ionization behavior is described by a diabatic state rather than by an adiabatic one [56]. We therefore avoid using the term “adiabatic limit” in this thesis.

Over the last few decades, the second ionization pathway, namely SFI, has drawn immense research attention. This mechanism not only provides a dynamical setting for the study of a most intriguing quantum phenomenon—tunneling, but also marks the starting point for our understanding of various nonlinear processes caused by nonperturbative light-matter interaction [8, 28]. The better knowledge of SFI in turn leads to the emergence of new means to generate and engineer light. HHG, for example, converts incident infrared radiation into a broad spectrum extending into the soft x-ray regime. Such a spectrum can then be used to synthesize attosecond bursts of light, making it possible to track and manipulate electron motion on its intrinsic time scale [15, 17].

The notion of SFI in atoms as well as in dielectrics was first introduced in a theoretical work by Keldysh in 1964 [88]. Since then, the Keldysh theory of optical tunneling has been refined by several strong-field theories [22, 23], notably the Ammosov-Delone-Krainov (ADK) tunneling-rate model [196] and the Keldysh-Fraissal-Reiss (KFR) theory [also known as the strong-field approximation (SFA)] [88, 197, 198]. The experimental observation of SFI awaited the invention of the chirped pulse amplification (CPA) technique in the mid-1980s [6]. This technique compresses the laser pulse durations down below a picosecond and increases the peak intensities enormously, allowing one to truly explore the $\gamma \ll 1$ regime. A vast number of experiments have been performed to study SFI by measuring the yield or the asymptotic momentum distribution of freed electrons or ions upon ionization by a strong laser field [199–201]. While the experimental studies on such physical quantities have offered vital information of the SFI process in a *time-integrated* manner, it is paramount to access the *real-time* dynamics of the ionization process to gain a more comprehensive understanding of SFI. Because modern conventional strong-field laser systems have optical periods corresponding to a few femtoseconds, it is necessary to apply attosecond techniques to probe the sub-laser-cycle ionization dynamics.

State of the art and limitations. From its initial realization, attosecond spectroscopy has revolutionized time-resolved methods by fully capturing the dynamics of quantum systems ranging from nuclear motion within molecules and solids to more elusive dynamics of the constituent electrons in atoms, molecules and solid-state devices [15, 17]. In the past decade, attosecond spectroscopy has been extensively applied to study electronic motion in real time, including the observation of a few-femtosecond Auger process [202] and unexpected single-photon ionization delays between electronic sub-shells in atoms [19, 203, 204] and in solid-state materials [20, 205]. The first experimental evidence for ionization steps in field-induced tunnel ionization came into light in 2007; the experiment was performed on atomic Ne by

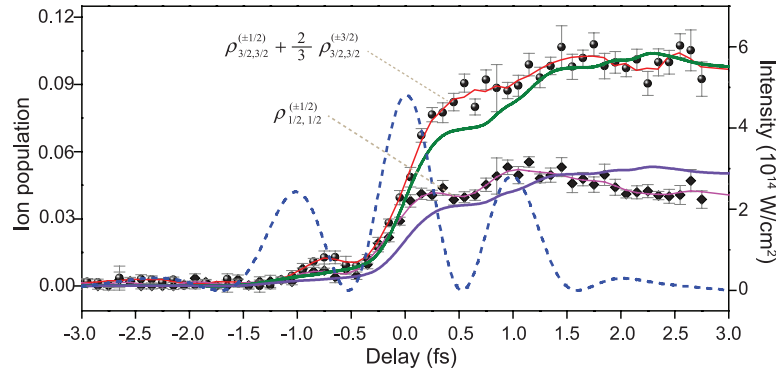


Figure 5.2. Ion-state-resolved subfemtosecond SFI dynamics in the Kr valence $4p$ shell measured using the ATAS technique by Wirth et al. The retrieved ion population dynamics in the ionic ground-state $4p_{j=3/2}^{-1}$ manifold (filled circles: experiment; green line: theory) and in the ionic excited-state $4p_{j=1/2}^{-1}$ manifold (filled diamonds: experiment; purple line: theory) both grow monotonically in steps as a function of the pump-probe delay. In above, j is the quantum number of the total angular momentum of the hole. The instantaneous intensity of the electric field is represented by a blue dashed line. The figure is adapted from Ref. [90]. Copyright ©2011 American Association for the Advancement of Science.

Uiberacker et al. [89].

In more recent years, attosecond metrology has also been combined with the transient absorption technique [206–209]. Quite complementary to the type of aforementioned experiments (the method of attosecond streaking), which is based on the detection of freed charged particles leaving to the asymptotes, the method of attosecond transient absorption spectroscopy (ATAS) is an all-optical setup that measures the dynamics of the remaining ions directly in the pump-probe interaction volume. Other unique features of ATAS include that it offers high temporal and spectral resolutions at the same time,^b and that it follows the occurrence of the dynamics through efficient resonant transitions between discrete and distinctive ionic energy levels. Following this routine, in 2011, Wirth et al. [90] presented a study on the time-resolved SFI dynamics in atomic Kr launched by a few-cycle ionizing field. The result of their experiment is shown in Fig. 5.2. Here, in addition to the tunnel ionization steps that have already been observed in Ref. [89], the SFI dynamics are further resolved for two

^bNote that there is no violation of the uncertainty principle here. The temporal resolution is decided by the (probe) pulse duration, while the spectral resolution is determined by the spectrometer. In other words, the simultaneous high temporal and spectral resolutions are not conjugated variables to each other and, thus, do not break the uncertainty principle.

different Kr^+ species that are characterized by an electron vacancy, or a hole, in a different spin-orbit-split valence orbital.

In this chapter, we will take on the ATAS approach in order to investigate the subcycle- and ion-state-resolved SFI dynamics of a more complicated atomic system: Xe. Through our joint experiment-theory collaboration, we will show that the stepwise, monotonically growing ion buildup process seen in Refs. [89, 90] is no longer the only type of electron motion during SFI and a previously unobserved type of electron motion surfaces. First, we will demonstrate the quantitative capacity of ATAS as a tool to take ultrafast snapshots of tunnel ionization. Then, by exploiting the TDCIS theory, we will reveal the origin of the formerly unnoticed attosecond electron dynamics in strong optical fields. Our work suggests that a new component needs to be added to the standard tunneling picture, especially as one moves towards the strong-field study of electronic systems with increasing complexity.

5.2 Taking attosecond snapshots of strong-field ionization

Motivation. Making ultrafast movies of electron motion is the ultimate goal of attosecond science [15, 17]. Despite of emerging experimental results, the interpretations of attosecond measurements are complicated and offer only a glimpse of their potential [210]. This challenge is precisely what one has to face while using the ATAS technique to track the subcycle SFI dynamics. Up to now, no analytical theory exists that rigorously maps the pump-probe signal to any instantaneous property of the ion at the moment when it is hit by the probe. Complications arise because, in order to follow the ion dynamics occurring *during* SFI, the pump and probe pulses must overlap temporally. Therefore, the ionic system is continuously subjected to the influence of the pump even after the probe step is over. This situation is to be contrasted with the case where ATAS is used to probe the ion dynamics happening *after* SFI [206]. There, the pump and probe pulses do not overlap in time, so the ionic system undergoes field-free evolution after the probe step, which allows the development of an analytical theory [211] that connects the pump-probe signal to the instantaneous ionic state as described by the ion density matrix (IDM) (see 2.2.3). Since this condition no longer holds when adopting overlapping pump and probe pulses, it is unclear whether or not the non-trivial post-probe evolution of the ion can make an additional contribution to the transient absorption signal—that is, an artifact—in the SFI dynamics reconstructed from ATAS data. In fact, a related problem has already been analyzed by the community of femtosecond transient absorption spectroscopy: it is well known that, while the pump and the probe pulses

are coherent and overlapping, they can make extra and irregular contributions to the transient absorption signals, generally termed “coherent artifacts” [212–214]. Therefore, there is an important question left open to the practitioners of ATAS: To which extent can the ATAS technique be used to take *instantaneous* attosecond snapshots of the SFI dynamics?

Contributions of this thesis. In this section, via a thorough comparison of high-quality experimental and numerical data, we concretely demonstrate that ATAS is able to capture essential features of the instantaneous SFI dynamics of Xe in a subcycle– and ion-state–resolved manner, even when the pump and probe pulses overlap temporally. Several improvements made in this work enable a more comprehensive comparison between experiment and theory, putting the earlier conclusion drawn from the ATAS experiment on Kr by Wirth et al. [90] and its subsequent theoretical analysis by Pabst et al. [46] on a more solid ground. Experimentally, a new method for generating high-flux, high-contrast, and tunable single attosecond pulses [215] is employed, leading to reduced statistical errors in the measured data. On the theory side, analysis is performed in order to make sure that the absorption signals are not contaminated by multichannel coherence between two ionic states [211] and thus can be properly used to represent the measured ion population dynamics, an aspect that was not addressed in Refs. [46, 90]. Our work strengthens the quantitative foundation for the ATAS technique.

Our investigation on the subcycle SFI dynamics of Xe rigorously establishes a new feature of electron motion in strong optical fields: apart from the typical tunnel ionization steps, the observed SFI dynamics exhibit salient oscillations occurring at twice of the pump frequency. These oscillations were not seen in previous time-resolved SFI measurements on lighter atoms, neither in the attosecond streaking experiment on Ne [89], nor in the ATAS experiment on Kr [90]. Additionally, they cannot be explained by standard SFI theories [196, 216, 217], which predict a monotonic ion buildup process. This oscillatory electronic behavior during tunnel ionization suggests a missing component in the SFI picture, and its physical origin awaits further investigations.

Methodology. Due to the special nature of this combined experimental and theoretical study, the methodology will be explained in the upcoming subsection.

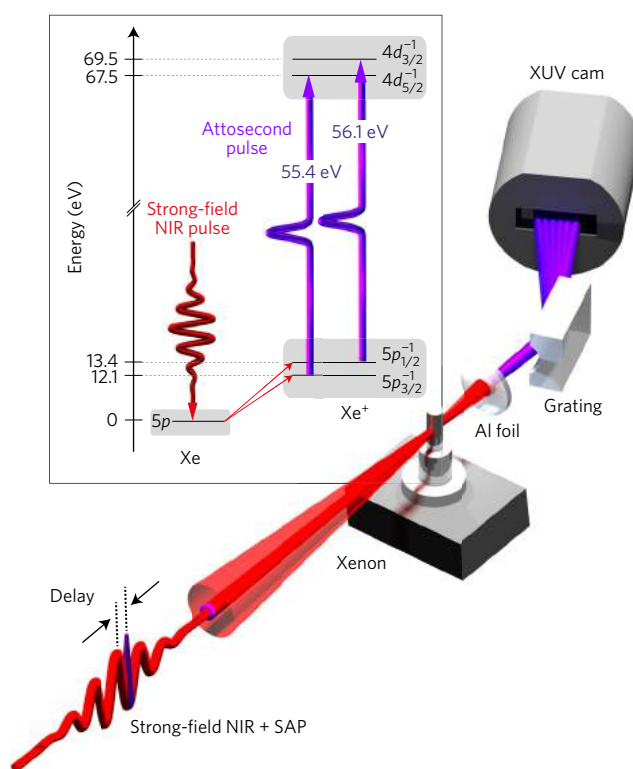


Figure 5.3. ATAS experimental scheme. An intense waveform-stabilized, few-cycle NIR laser pulse (red) induces SFI in Xe atoms, which creates hole populations in the spin-orbit-split states, $5p_{1/2}^{-1}$ and $5p_{3/2}^{-1}$ of the emerging ions. A time-delayed single attosecond pulse (SAP, purple) is used to probe the population in both of the states by promoting the valence holes into the $4d_{3/2}^{-1}$ and $4d_{5/2}^{-1}$ core states. The dynamics are recorded by measuring the transient changes in the spectrum of the single attosecond pulse by means of an XUV spectrometer. The figure is adapted from Ref. [60]. Copyright ©2017 Nature Publishing Group.

5.2.1 Concept of the experiment and the theoretical modeling

Our goal is to employ the ATAS technique with overlapping pump and probe pulses in order to track the sub-cycle and state-resolved ion creation dynamics of Xe during strong-field ionization. Here, let us first introduce the basic idea behind the pump-probe scheme, and then present some details about the experimental and theoretical approaches.

Concept of the experiment. The principle of the ATAS experimental scheme is presented in Fig. 5.3. A few-cycle, waveform-stabilized NIR pump pulse centered around 790 nm is focused into a cell filled with Xe gas. The interaction of the strong laser field with the Xe

atoms results in the ionization of Xe to the two valence spin-orbit-split states, $5p_{1/2}^{-1}$ and $5p_{3/2}^{-1}$. Here, each subscript denotes the quantum number of the total angular momentum (i.e. the sum of the orbital and spin angular momenta) of the hole. The peak intensity of the NIR pump is varied between 2.0×10^{14} and 3.2×10^{14} W/cm², corresponding to Keldysh parameters of $\gamma \approx 0.72$ and 0.57 , respectively. Although γ is only slightly smaller than one, previous studies have shown that ionization in this parameter range is dominated by the SFI mechanism [27, 217].

The probe pulse is a weak, single attosecond pulse with a central frequency in the XUV region. The probe induces one-photon transitions in Xe⁺ that give rise to characteristic lines in its absorption spectrum at 55.4 eV and 56.1 eV, corresponding to the two strongest hole transitions $5p_{3/2}^{-1} \rightarrow 4d_{5/2}^{-1}$ and $5p_{1/2}^{-1} \rightarrow 4d_{3/2}^{-1}$, respectively. At the intensities applied in this study, the third dipole-allowed transition corresponding to $5p_{3/2}^{-1} \rightarrow 4d_{3/2}^{-1}$ does not provide a sufficiently high signal-to-noise ratio to enable the observation of attosecond ionization dynamics.

The interaction of the strong NIR pump pulse with Xe atoms is captured by recording the transient absorption spectrum of the XUV probe, which is defined by the differential optical density, or $\Delta OD(E, \tau) = -\ln[I_{\text{on}}(E, \tau)/I_{\text{off}}(E, \tau)]$, as a function of the time delay τ between the NIR pump and the XUV probe. Here, I_{on} and I_{off} represent the XUV spectra with and without the NIR pump field. For given target parameters, ΔOD is directly proportional to the absorption cross section. Based on our physical intuition, the stronger a characteristic absorption line is, the higher the population is in a specific valence hole state at the instant of the probe step. Thus, it seems reasonable to assume that, by recording the strengths of the absorption lines as a function of the pump-probe delay, ATAS would allow one to map out the valence hole population dynamics during SFI.

More on the experimental method. Attosecond XUV pulses are generated by means of HHG in Ar. For the proper isolation of a single sub-200 as pulse, the recently developed technique of Polarization ASSisted Amplitude GatE (PASSAGE) is applied [215]. The attosecond pulse is spatially and temporally overlapped with an intense few-cycle NIR laser pulse in an interferometric scheme that allows the precise control of the delay between the two pulses with a long-term accuracy of 80 as r.m.s. A toroidal mirror is subsequently used to focus both pulses into a Xe-filled gas cell. The SFI induced by the NIR laser pulse is probed via absorption of the delayed attosecond pulse using an XUV photon spectrometer. The experimental apparatus is sketched in Fig. 5.4. For additional details and explanations please refer to the

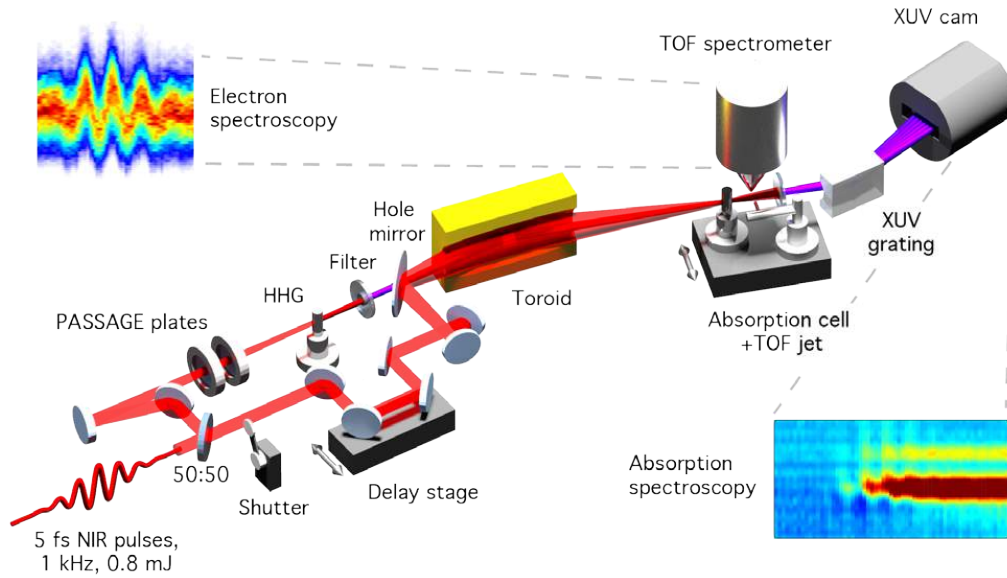


Figure 5.4. Illustration of the experimental apparatus. A few-cycle NIR pulse first hits a beamsplitter with a ratio of 50 : 50, thereby creating two equally strong laser pulses. The reflected part is used to generate an attosecond pulse via HHG using the PASSAGE technique. A hole mirror is then used to recombine the attosecond beam with the delay-adjustable NIR pulse originating from the transmission on the beamsplitter. The two spatially and temporally overlapped pulses are subsequently focused into either of two different types of targets to perform absorption spectroscopy (for ATAS measurements) or electron spectroscopy (for temporal characterization of the NIR and XUV pulses) with attosecond time resolution. To avoid overly confusing beampaths, the delay stabilization scheme is excluded from this schematic. The figure is reproduced from Ref. [60]. Copyright ©2017 Nature Publishing Group.

supplementary information accompanying the original publication [60].

Theoretical modeling. The theoretical modeling of the experiment is based on numerical solution of the N -electron TDSE using TDCIS under the experimental conditions. Here, the Hamiltonian responsible for the light-atom interaction is described in the length gauge in Eq. (2.24). In order to account for the split-orbit effects, a spin-orbit interaction term [28] is added to the HF Hamiltonian in Eq. (2.25) and is treated within the framework of the first-order perturbation theory [46, 57]. Because the radial dependence of the spin-orbit interaction scales with r^{-3} as $r \rightarrow \infty$, the correction is made only for the occupied orbitals and is neglected for the virtual orbitals. The new spin-orbit-coupled hole orbitals are linear combinations of the original hole orbitals without spin-orbit interaction, with the expansion coefficients given by the Clebsh-Gordan coefficients. For further details please refer to

Ref. [57].

For each pump-probe delay, the evolution of the TDCIS wave packet is calculated with an electric field profile containing the overlapping NIR pump and XUV probe. This explicitly takes into consideration the nonperturbative nature of the pump pulse. The simulation of the ATAS spectrum can be dissected into the following steps. First, the time-dependent ionic dipole moment is computed from the IDM [see Eq. (2.31)] via [46]

$$\langle z \rangle_{\text{ion}}(t) = \text{Tr}[\hat{z}\hat{\rho}^{\text{IDM}}(t)]. \quad (5.1)$$

Second, the atomic absorption cross section can be obtained by Fourier transforming the ionic dipole $\langle z \rangle_{\text{ion}}(t)$ and the electric field of the probe $E_{\text{probe}}(t)$ [46],

$$\sigma_a(\omega) = \frac{4\pi\omega}{c} \text{Im} \left[\frac{\langle z \rangle_{\text{ion}}(\omega)}{E_{\text{probe}}(\omega)} \right], \quad (5.2)$$

where c is the speed of light. The atomic cross section describes the absorption behavior of one single atom. To include the macroscopic propagation effect of the transmitted light traveling through an ensemble of atoms, in the third step, we assume that the gas sample is homogeneous such that the spectrum of the probe is damped according to the Beer-Lambert law,

$$|E_{\text{probe}}(L, \omega)|^2 = |E_{\text{probe}}(0, \omega)|^2 e^{-Ln_a\sigma_a(\omega)}, \quad (5.3)$$

where $E_{\text{probe}}(L, \omega)$ is the spectrum of the probe at the end of the medium with a length of L , and n_a is the atomic number density. The validity of the Beer-Lambert law in similar pump-probe scenarios has been demonstrated in [211, 218]. Finally, the measured cross section at the detector is given by [46]

$$\sigma_m(\omega) = -\frac{1}{Ln_a} \ln \left[e^{-n_a L \sigma_a(\omega)} * G_{\delta E}(\omega) \right], \quad (5.4)$$

where $G_{\delta E}(\omega)$ is the area-normalized Gaussian with a width of δE , and $*$ symbolizes the frequency convolution operator.

5.2.2 ATAS spectrograms

The experimental ATAS spectrogram for an NIR intensity of 3.2×10^{14} W/cm² is shown in Fig. 5.5. The data contain rich spectroscopic features for both of the spin-orbit ionization

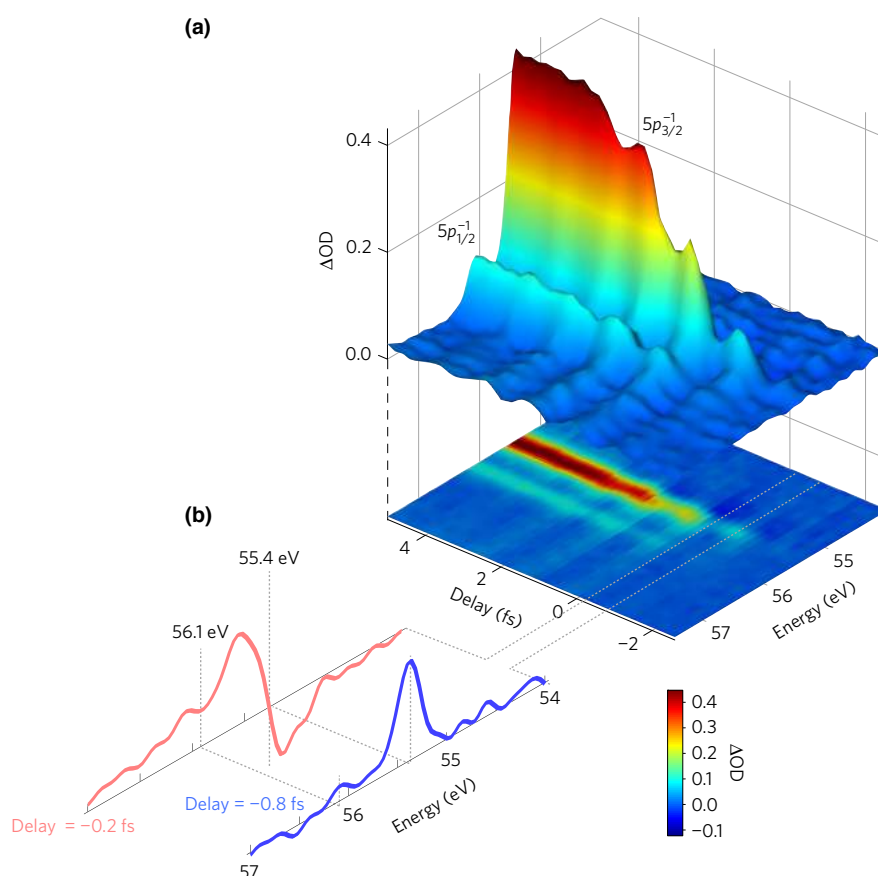


Figure 5.5. Experimental ATAS spectrogram. **(a)** The spectrum measured as a function of the delay between the few-cycle NIR pump and the isolated attosecond XUV probe for an NIR intensity of 3.2×10^{14} W/cm². The upper panel shows a surface representation underlining the observation of half-cycle oscillations in the spectral-line amplitudes, whereas the projection depicted in the lower panel emphasizes changes in the spectral lineshapes. **(b)** Snapshots of the spectrum at two different delays between which the lineshapes change most drastically. The figure is adapted from Ref. [60]. Copyright ©2017 Nature Publishing Group.

channels imprinted by the underlying strong-field dynamics. Most importantly, the attosecond temporal resolution gives access to the natural timescale of the electron dynamics dictated by the strong laser field. In the following, we discuss two attributes of the absorption lines.

Amplitudes of the absorption lines. First, let us take a look at the amplitudes of the absorption lines as a function of the delay in Fig. 5.5(a). As can be observed, each spectral-line amplitude, which is naïvely expected to be proportional to the population in each valence hole orbital, shows a characteristic stepwise growing behavior. This provides strong evidence for the tunneling nature of the measured ion-creation process for both of the spin-orbit states $5p_{3/2}^{-1}$ and $5p_{1/2}^{-1}$. As expected from various SFI models [88, 196, 216, 217], tunneling mainly follows the oscillating NIR laser field in a nonlinear fashion. The tunneling rate is very sensitive to the instantaneous value of the electric field: it is essentially zero around the nodes of the electric field, and reaches a maximum at the extrema of the electric field. This gives rise to the tunnel ionization steps, with a plateau structure whenever the electric field sweeps through zero.

Surprisingly, in addition to the above feature, which has already been seen in the previous time-resolved SFI experiments [89, 90] (see Fig. 5.2), the amplitudes of the two absorption lines observed here also exhibit pronounced oscillations that occur with a periodicity of 1.2 fs, which coincides with twice the NIR laser frequency, $2\omega_L$. This strong deviation from the typical plateau structure will be discussed in Sec. 5.3, after we verify that they are a genuine feature of the SFI dynamics instead of an artifact of the ATAS technique.

Shapes of the absorption lines. Now let us examine the shapes of the absorption lines in the measured spectrogram in Fig. 5.5(a). They show strong, dynamical deformations, especially when the delay is about zero or negative. To better visualize the subcycle lineshape evolutions, two snapshots of the spectrum are illustrated in Fig. 5.5(b). Remarkably, the major absorption line, which is centered at 55.4 eV and is due to the transition $5p_{3/2}^{-1} \rightarrow 4d_{5/2}^{-1}$, bears a Lorentzian profile at $\tau = -0.8$ fs, whereas it switches to a Fano profile at $\tau = -0.2$ fs.

Such ultrafast lineshape modifications have been observed in the ATAS experiment on Kr [90], and its physical origin has been explained in Ref. [46] using an oscillating (ionic) dipole model as follows. For this particular spectral line, the coherent superposition of the $5p_{3/2}^{-1}$ and $4d_{5/2}^{-1}$ states of Xe^+ created by the XUV probe kick-starts an oscillating ionic dipole that decays with some characteristic lifetime because of the Auger decay of the $4d_{5/2}^{-1}$ hole

($\tau_{\text{Auger}} \approx 6$ fs [118]). The dynamics of this dipole dictates the absorption spectrum of the XUV probe [see Eq. (5.2)]. Provided that the dipole subsequently undergoes field-free evolution, this decay will lead to a characteristic Lorentzian absorption profile [211]. However, when the NIR and XUV pulses temporally overlap—as is the case in the experiment—the NIR pulse can still modify the oscillating dipole before it damps out, leading to a phase shift in the dipole and giving rise to an asymmetric, Fano absorption profile. It is found that the coupling between the NIR pump and the ground state of the neutral atoms is the primary source of the post-probe modulation of the ionic dipole [46]. On the positive side, one could say that this mechanism offers a way to control lineshapes on the attosecond time scale; on the negative side, these pump-induced lineshape deformations are a manifestation of the inherent limitation of ATAS in the presence of overlapping pump and probe pulses.

5.2.3 Reconstruction of the effective SFI dynamics

As explained in 5.2.1, the experimental quantities that can be most intuitively related to the ion populations are the strengths of the transient absorption lines. Nevertheless, owing to the NIR-induced lineshape variations, such population dynamics cannot be extracted directly from a simple lineout analysis. In this subsection, we introduce the fitting model used for our data analysis, examine the physical meanings of the fitting parameters of interest, and then present the effective SFI dynamics retrieved from the ATAS spectrograms.

Oscillating dipole fitting model. In order to extract the delay-dependent valence-hole population dynamics from our pump-probe spectrograms in the presence of lineshape deformations, we adopt a fitting procedure based on the oscillating dipole model. The physical picture of this model has already been described in 5.2.2. Here, we focus on explaining how this model can be empirically used to capture the observed spectral features.

The oscillating dipole model was first proposed by Pabst et al. [46], and has been successfully applied to the analysis of the ATAS experiment conducted by Wirth et al. [90]. It models the atomic absorption cross section σ_{dip} as a function of the XUV photon energy ω at a delay τ by the following expression

$$\sigma_{\text{dip}}(\omega, \tau) = \frac{4\pi\omega}{c} \sum_T z_T(\tau) \frac{\Gamma_T/2 \cos[\phi_T(\tau)] + (\omega - \omega_T) \sin[\phi_T(\tau)]}{(\omega - \omega_T)^2 + \Gamma_T^2/4}. \quad (5.5)$$

In above, each absorption line T sits at an energy position of ω_T and has a width of Γ_T , which is the inverse of the Auger lifetime of the core-hole-excited state. For each T , there

are two delay-dependent fitting parameters: $\phi_T(\tau)$ and $z_T(\tau)$; they are used to approximately describe the entire dipole dynamics after the probing process. The parameter ϕ_T is the effective dipole phase. It is designed to encapsulate the (pump-induced) lineshape deformation, which is the main focus of Ref. [46]. In this work, we concentrate on the other fitting parameter z_T . It is the effective dipole transition strength after removing the lineshape modulation effects. Under one condition as will soon be clarified, z_T can be interpreted as the effective valence-hole population in the experiment up to a channel-dependent scaling constant. More specifically, $z_T(\tau) = |d_T|^2 \rho_T^{\text{eff}}(\tau)$, with d_T being the dipole transition matrix element between the specific $5p^{-1}$ and $4d^{-1}$ along the laser polarization axis.

The hole populations retrieved from the ATAS absorption lines using the above procedure are termed *effective hole populations*. They are the physical quantities that best represent the ion populations appearing in a pump-probe measurement. The effective hole populations $\rho_T^{\text{eff}}(\tau)$ are to be distinguished from the *instantaneous hole populations* $\rho_T^{\text{inst}}(\tau)$. The latter are the actual ion populations at the instant when the probe pulse arrives and are determined by the instantaneous IDM. Just like the case for ϕ_T , z_T and thus ρ_T^{eff} may be sensitive to what happens to the ion after the probe step and, hence, may be different from ρ_T^{inst} . If the pump were to be immediately turned off right after the probe step, ρ_T^{eff} would be the same as ρ_T^{inst} .

As a final note, to account for the finite spectral resolution at the XUV spectrometer, the experimental datasets are fitted to Eq. (5.5) convolved with a Gaussian function with a width of 200 meV. The convolution of a complex Lorentzian and a Gaussian yields an analytic expression involving a complex error function, or the Faddeeva function [219], and slightly broadens the absorption lines. The same fitting procedure is used for both the experimental and simulated ATAS data.

Effects of multichannel coherence on the effective hole dynamics. Strictly speaking, the above interpretation of the effective dipole transition strengths $z_T(\tau)$ as the effective ion populations $\rho_T^{\text{eff}}(\tau)$ is reasonable under one condition—that there is no quantum coherence between $5p_{1/2}^{-1}$ and $5p_{3/2}^{-1}$ in the ionic system.

As shown by the analytical theory for ATAS with nonoverlapping pump and probe pulses [211], such a coherent superposition of the ionic states can make an additional contribution to the absorption line corresponding to the transition $5p_{1/2}^{-1} \rightarrow 4d_{3/2}^{-1}$ when probing the ion dynamics after the SFI process. That is, the strength of this line is decided not only by the targeted $5p_{1/2}^{-1}$ population (a diagonal term in the IDM), but also by the unwanted coherence between $5p_{1/2}^{-1}$ and $5p_{3/2}^{-1}$ (an off-diagonal term in the IDM). Consequently, in order to

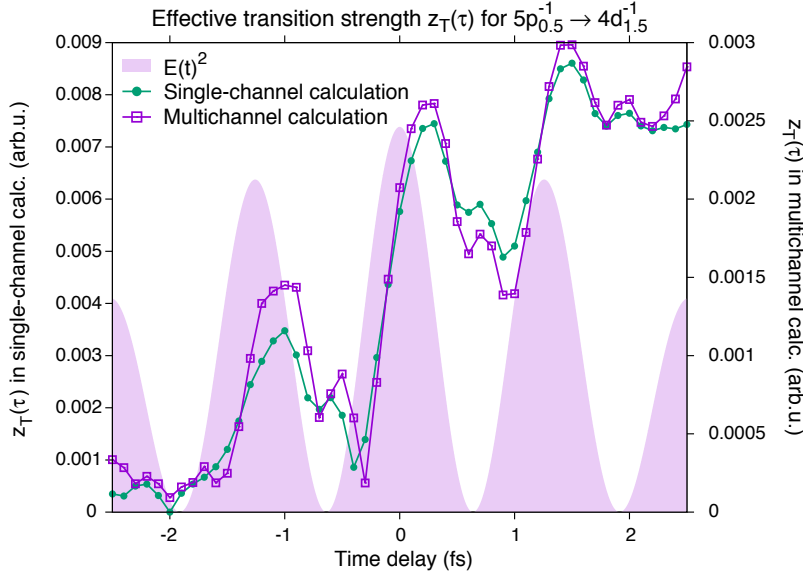


Figure 5.6. Comparison of the calculated transition strength $z_T(\tau)$ for the $5p_{1/2}$ channel in the simplified single-channel model and that in the full multichannel model. The values of $z_T(\tau)$ are shown in arbitrary units (arb. u.). The ATAS spectrograms, from which the $z_T(\tau)$ are extracted, are computed using the TDCIS theory. The NIR pump has a peak intensity of 1.5×10^{14} W/cm², and its instantaneous intensity is indicated by the shaded area. The figure is reproduced from Ref. [60]. Copyright ©2017 Nature Publishing Group.

meaningfully assign the effective transition strength of the spectral line $5p_{1/2}^{-1} \rightarrow 4d_{3/2}^{-1}$ to the effective $5p_{1/2}^{-1}$ population, the multichannel coherence between $5p_{1/2}^{-1}$ and $5p_{3/2}^{-1}$ must have a negligible impact on the retrieved $z_T(\tau)$. As for the other absorption line corresponding to the transition $5p_{3/2}^{-1} \rightarrow 4d_{5/2}^{-1}$, because it is not affected by any coherence term [211], the effective transition strength can be directly used to represent the effective $5p_{3/2}^{-1}$ population.^c

While the influences of multichannel coherence are infeasible to evaluate in experiment, they can be easily tested in theory. Numerically, we can switch off multichannel coherence by simply performing a single-(valence-)channel calculation in the TDCIS theory. In this simplified model, the few-cycle NIR is only allowed to generate a $5p_{1/2}^{-1}$ hole and is forbidden to form a $5p_{3/2}^{-1}$ hole, so the off-diagonal IDM matrix element $\rho_{5p_{1/2}^{-1}, 5p_{3/2}^{-1}}^{\text{IDM}}$ is automatically zero. The comparison between the effective transition strength for the $5p_{1/2}$ channel in the simplified single-channel model and that in the full multichannel model is shown in Fig. 5.6. The

^cNote that multichannel coherence can also contribute to the absorption line corresponding to the transition $5p_{3/2}^{-1} \rightarrow 4d_{3/2}^{-1}$ [211], whose ionization dynamics is beyond the scope of the current study due to the low signal-to-noise ratio in the experimental and stimulated ATAS spectrograms.

transition strength in each case is obtained by first calculating the ATAS spectrogram explicitly with both the pump and probe pulses and then fitting the spectrogram to the convolved oscillating dipole model using the same procedure for analyzing the experimental data. The NIR peak intensity here is 1.5×10^{14} W/cm². The effective transition strengths predicted by the two models clearly exhibit the same dynamics (up to a scaling constant). Particularly, the half-cycle oscillations occur at the same time delays. The only difference between the two is the absolute magnitude of $z_T(\tau)$. The $z_T(\tau)$ in the single-channel calculation has a larger magnitude, because the $5p_{1/2}$ channel in this case does not need to compete with the $5p_{3/2}$ channel to depopulate the neutral Xe ground state [see the TDCIS equation of motion in Eq. (2.30a)].

Figure 5.6 provides evidence that multichannel coherence has a negligible impact on $z_T(\tau)$ for the $5p_{1/2}$ channel when ATAS is used to probe the ion dynamics in the course of SFI. As a result, all the temporal structures of $z_T(\tau)$ retrieved from an ATAS spectrogram can be entirely attributed to the dynamics of $\rho_T^{\text{eff}}(\tau)$. To put it differently, the effective dipole strengths $z_T(\tau)$ can be meaningfully associated with the effective hole populations $\rho_T^{\text{eff}}(\tau)$ for both $5p_{1/2}^{-1}$ and $5p_{3/2}^{-1}$ in our analysis.

Reconstructed effective SFI dynamics. We have chosen a quantity—the effective dipole transition strengths—that can be used to best represent the effective hole populations appearing in our ATAS experiment. The effects of lineshape deformations are properly taken into account by employing the oscillating dipole model [see Eq. (5.5)], and the possibility of multichannel coherence to contaminate the dipole strengths are ruled out by our numerical calculations (see Fig. 5.6). We point out that the latter aspect was not addressed in Refs. [46, 90] and is an original insight provided by this work.

Figure 5.7(a) presents the effective hole populations reconstructed from the experimental ATAS data; they are proportional to the fitting parameters, the effective dipole strengths, via $\rho_T^{\text{eff}}(\tau) = z_T(\tau)/|d_T|^2$. Even after considering the above two factors, the effective ion populations for both of the valence-hole states $5p_{1/2}^{-1}$ and $5p_{3/2}^{-1}$ still exhibit strong oscillations occurring at the $2\omega_L$ frequency. Clearly, the oscillations are an innate feature of the effective hole dynamics rather than an artificial product of our data-analysis scheme. Furthermore, another two key features are established. First, the oscillations are relatively stronger for the lower-intensity case, and become comparatively weaker for the higher-intensity case. Second, phase delays are observed experimentally between the hole dynamics of the two spin-orbit channels: the oscillation maxima in one channel are shifted in reference to those

in the other. At the lower intensity, the phase delays are negligible and the populations are almost in phase. However, at the higher intensity, the $5p_{3/2}^{-1}$ channel is clearly delayed with respect to the $5p_{1/2}^{-1}$ channel by approximately 200 as.

To better understand the mechanisms underlying the experimental observations, the effective hole populations under the experimental conditions are calculated using the TDCIS theory and are displayed in Fig 5.7(b). The numerically reconstructed effective hole dynamics well reproduce all the important features seen in the experimental data, including the existence of prominent half-cycle oscillations superimposed on a step-wise growing background, the dependency of the oscillation amplitudes on the pump intensity, the phase delays between the two channels, and the correlation of the delays with the pump intensity. The good quantitative agreement between our theoretical and experimental results demonstrates that the TDCIS approach is well suited for predicting the SFI dynamics as observed in the measurement.

5.2.4 Comparison between the effective and the instantaneous SFI dynamics

After validating the TDCIS theory, it is now utilized to answer the main question posed at the beginning of this section: to which extent can the ATAS technique be used to take *instantaneous* attosecond snapshots of the SFI dynamics?

The caveat. Since it is extremely important to keep this question in mind, we reiterate the caveat associated with the interpretation of the ATAS experiment and go back to the oscillating dipole picture for the last time. In this picture, ATAS measures a signal over the lifetime of the core-hole-excited state—a signal that is inherently nonlocal in time [210, 211]. During this time window, the intense NIR pump can still interact and change the ionic dipole after the probe step. The whole dynamics of the dipole—from the moment it is created by the probe until it damps out due to the Auger decay—are what gets recorded in the transient absorption spectrum. And all the complications arise because one wants to follow the ion creation processes during SFI and thus needs to employ a pair of pump and probe pulses overlapping in time. Such post-probe dynamics of the ionic system has been shown to impart a phase shift to the oscillating dipole, which leads to the aforementioned line deformations [46, 90]. Hence, it is highly nontrivial to assess whether or not this mechanism can also modify the effective dipole strengths and accordingly cause the effective hole populations to deviate from the instantaneous values at the exact arrival time of the probe pulse.

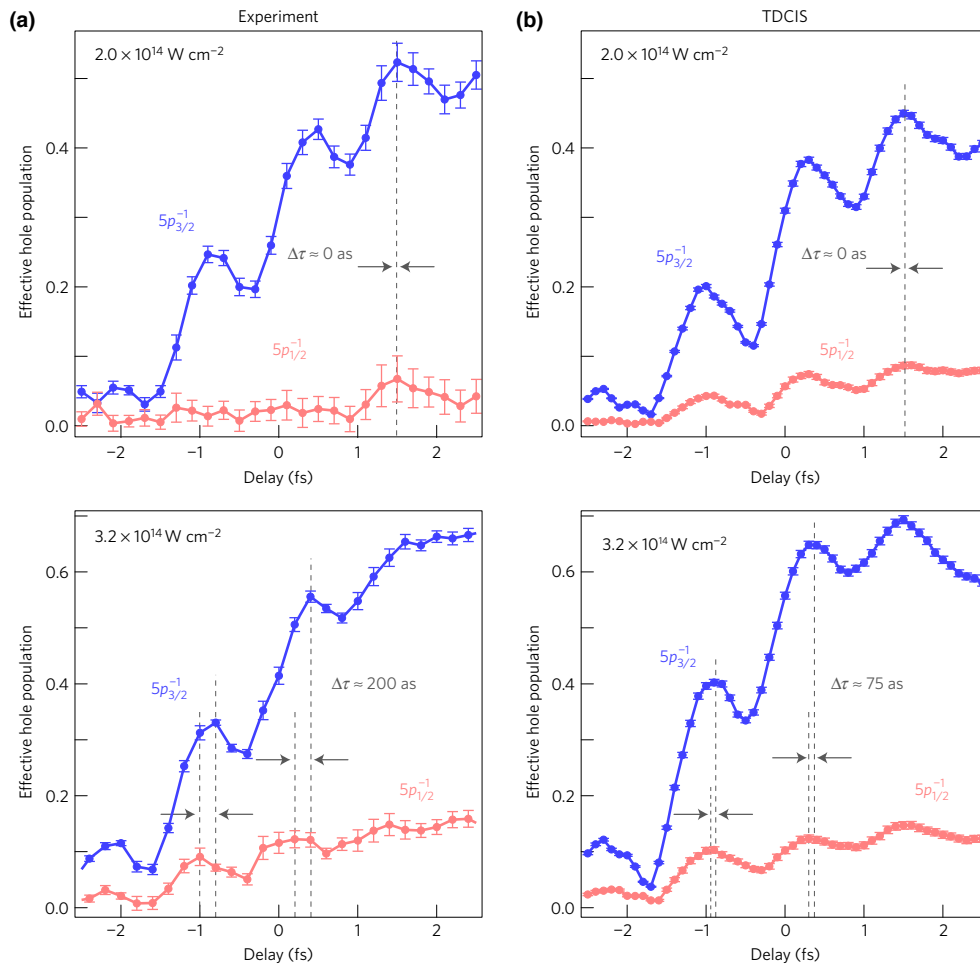


Figure 5.7. Reconstruction of the experimental and theoretical effective Xe^+ populations from the ATAS spectrograms. A fitting procedure based on the convolved oscillating dipole model is applied to the ATAS spectrograms, which allows for the retrieval of the effective ion populations in the $5p_{3/2}^{-1}$ (red) and $5p_{1/2}^{-1}$ (blue) states for (a) the experimental and (b) the theoretical data sets. For a more direct comparison between experimental and TDCIS data sets, the unknown offsets of the delay axes of the experimental data in (a) have been shifted by $+0.5$ fs and -1.2 fs for the NIR intensities of 2.0×10^{14} W/cm² and 3.2×10^{14} W/cm², respectively. The existence of the half-cycle oscillations and the relative phase delays between the two channels as well as the dependency of these two quantities on the intensity demonstrate the solid agreement between experiment and the TDCIS theory. For the evaluation of the relative phase delays, we consider only the positions of the oscillation maxima where the experimental SFI dynamics provide enough signal to noise and display noticeable oscillations. The error bars on the data represent the 95% confidence interval resulting from the fitting procedure. The figure is reproduced from Ref. [60]. Copyright ©2017 Nature Publishing Group.

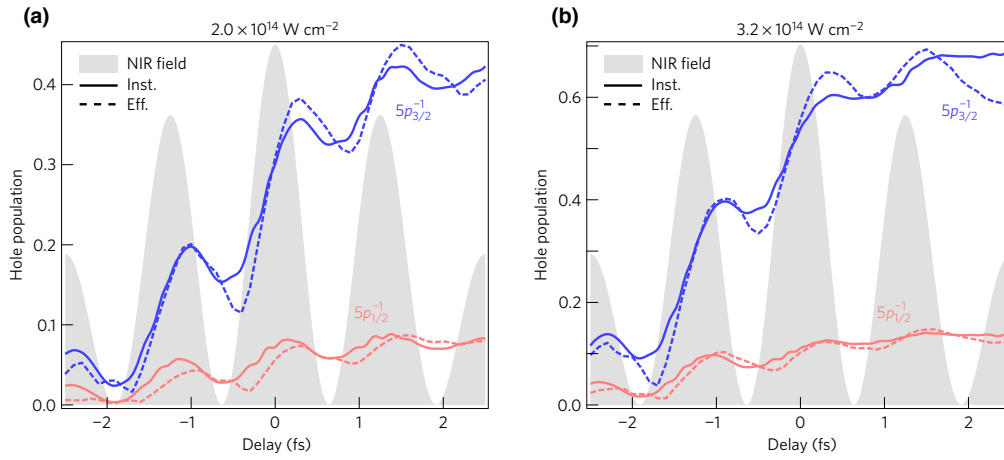


Figure 5.8. Comparison between the effective and the instantaneous populations dynamics. The relation between the dynamics of the effective (“Eff.”, dashed) and instantaneous (“Inst.”, solid) hole populations is assessed by using the TDCIS theory for NIR intensities of (a) $2.0 \times 10^{14} \text{ W/cm}^2$ and (b) $3.2 \times 10^{14} \text{ W/cm}^2$. In each panel, the profile of the instantaneous NIR intensity is indicated by a shaded area. The reasonable quantitative agreement demonstrates the ability of the ATAS technique to track real-time—that is, instantaneous—SFI dynamics. The figure is reproduced from Ref. [60]. Copyright ©2017 Nature Publishing Group.

Comparison between the effective and the instantaneous population dynamics. To answer the above question, we directly compare the aforeshown TDCIS effective hole dynamics to the TDCIS instantaneous hole dynamics for the $5p_{1/2}^{-1}$ and $5p_{3/2}^{-1}$ channels in Figs. 5.8(a) and (b) at the NIR intensities of $2.0 \times 10^{14} \text{ W/cm}^2$ and $3.2 \times 10^{14} \text{ W/cm}^2$, respectively. The instantaneous ion populations are calculated by solving the N -electron TDSE under the sole influence of the pump and are decided by the diagonal IDM matrix elements $\rho_{j,j}^{\text{IDM}}(t = \tau)$, $j = 1/2, 3/2$ in Eq. (2.31). The key features of the effective populations, including the existence of half-cycle oscillations and the depth of the oscillations, match quite well with those of the instantaneous populations. In addition, a phase delay is also consistently predicted between the spin-orbit states in the instantaneous dynamics.^d

^dThe Auger decay time introduces a small but intrinsic and system-dependent artifact of the ATAS technique when using overlapping pump and probe pulses. Since in our numerical experiments we can artificially tune the Auger lifetime of a $4d$ hole (see Sec. 2.3), we can test how fast the core-hole–excited state needs to decay in order to eliminate the discrepancy between the effective and instantaneous hole dynamics. We find that the Auger lifetime has to go down from its experimental value of 6 fs to as short as 0.1 fs for the difference to diminish noticeably.

Combining the results shown in Figs. 5.7 and 5.8, the joint experimental and theoretical investigation concretely demonstrates that ATAS in the case of overlapping pump and probe pulses is able to map out, to a reasonably well quantitative degree, the essential features of the instantaneous strong-field valence-hole dynamics on the attosecond time scale and in a channel-resolved manner. We rigorously extend the conclusion drawn from the earlier ATAS experiment on Kr [46, 90] to Xe, in particular, by inspecting the impacts of multichannel coherence on the retrieved absorption-line strengths used to define the effective SFI dynamics.

Apart from the typical tunnel ionization steps, we observe a new feature in the SFI dynamics, the half-cycle oscillations, which cannot be explained by existing SFI theories and were not seen in the previous time-resolved SFI experiments on lighter Kr and Ne atoms, using either the attosecond streaking method [89] or the ATAS method [90]. Because these oscillations are present in both the effective and the instantaneous hole dynamics, they are an intrinsic property of the SFI dynamics, and are not an artifact of the ATAS technique owing to the post-probe, pump-induced ion dynamics. The physical interpretation of the oscillations (and the phase delays) is the story of the next section.

5.3 Reversible and irreversible electron dynamics in strong optical fields

Motivation. In Sec. 5.2, we have rigorously shown that the electron motion during strong-field ionization exhibits an unexpected feature: in addition to tunnel ionization steps, the hole populations display prominent oscillations at twice of the frequency of the NIR driver. The existence of the half-cycle oscillations is observed for both of the spin-orbit–split valence-hole states of Xe^+ and in both of the effective and instantaneous hole dynamics. Consequently, they represent an intrinsic feature of the electronic response in the tunneling regime instead of a pump-induced artifact of the ATAS technique. The next question to be investigated naturally follows: what is the physical mechanism that gives rise to such oscillatory electronic behavior during SFI?

Contributions of this thesis. In this section, with the aid of theory, we identify the physical origin of the half-cycle oscillations. We demonstrate that they correspond to temporary enhancement of the ion populations and are a direct signature of bound electron motion stemming from strong-field–induced polarization of the neutral Xe ground state. We estab-

lish that there are two opposite types of ultrafast electron dynamics triggered by an intense laser field: one corresponds to an irreversible, monotonic ion build-up process as predicted by widely used tunneling models; another one is associated with a reversible, periodic electron displacement due to transient ground-state polarization. Albeit well known in the weak-field regime, the role polarization had so far been largely unnoticed, both experimentally and theoretically, in the strong-field regime. The exposed dichotomy of electron motion in the presence of strong light-matter interaction can be viewed as two facets of the light-induced tunneling ground state. This points to a new complexity that needs to be incorporated into the standard tunneling picture: during SFI, what matters is not only the field-dressed tilted potential but also the field-dressed quantum state from which the electron tunnels.

Here, it is worthwhile to point out two key factors that enable the observation of the strong-field-driven bound electron dynamics in our study. By doing so, we clarify how our results may impact and bring opportunities for future ultrafast and strong-field research. First, the observation of polarization effects is made possible thanks to choice of our target system: the “fuzzy” atomic Xe. In comparison to lighter Ne and Kr atoms used in the previous time-resolved SFI experiments [89, 90], Xe atoms are characterized by a high (static) ground-state polarizability ($\alpha_0^{\text{Xe}} \approx 27$ a.u., which is to be compared with, e.g., $\alpha_0^{\text{Kr}} \approx 17$ a.u. [220, 221]). As the attosecond community is moving towards the study of systems beyond noble gases, it is anticipated that polarization will play an even more crucial role in understanding the strongly driven electronic behavior thereof, especially for spatially extended molecules and solids with a small bandgap.

Second, the probing of intense-field-polarized electron motion is greatly facilitated by the unique, relatively unexplored type of systems that the ATAS technique gives direct access to: the photoions. For the majority of experimental and theoretical SFI studies that focus exclusively on the properties of photoelectrons in the asymptotes [89, 196, 216, 217], such localized charge-density deformation would be more evasive, if not impossible, to be detected. As such, it may be expected that, by shifting the attention to the complementary ionic systems, new information will emerge and foster the construction of the full landscape of the SFI process.^e

^eJust like in the famous fable of “the Blind Men and the Elephant”, studying a different type of physical systems offers a different angle to reveal insights of a physical process. As another example, the investigation of neutral excited states in strong laser fields uncovers the mechanism of frustrated tunnel ionization in 2008 [222], more than forty years after Keldysh’s prediction of SFI.

Methodology. Since the quantitative capacity of the TDCIS theory has already been verified in Sec. 5.2, it is utilized to analyze the half-cycle oscillations accompanying the SFI dynamics of Xe in this section. Furthermore, because we have shown the close resemblance between instantaneous and effective hole dynamics, our analysis here is concentrated directly on the instantaneous dynamics driven by an NIR pulse.

To gain insight into the strong-field driven ion dynamics, two types of calculations are performed within the TDCIS framework. In both cases, the Hamiltonian is expressed in the length gauge (see 2.1.2) and is non-Hermitian due to the application of a CAP (see 3.2.2).

In the first type of calculations, the TDCIS full wave-packet calculations, the hole dynamics are obtained by explicitly solving the N -electron TDSE in Eq. (2.16) and computing (the diagonal elements of) the IDM in Eq. (2.31). Here, the CAP is used to avoid artificial reflections of the wave packet at the edges of the numerical grid (see Sec. 3.3).

In the second type of calculations, the TDCIS tunneling-rate calculations, the hole dynamics are acquired by solving the N -electron TISE in Eq. (2.17) at various instantaneous NIR intensities under the quasistatic approximation; the CIS Hamiltonian that is diagonalized depends implicitly on time through the electric field strength. Here, the CAP is used to calculate (the imaginary part of) the Siegert energy in Eq. (3.7) for the resonance state from which the electron tunnels out. This state can be found by looking for the instantaneous eigenstate with the largest wave-function overlap with the field-free ground state [56, 223]; the lifetime of this state gives us the tunneling rate. By interpolating the tunneling rates at different field strengths and then feeding them into a set of coupled rate equations

$$\dot{\rho}_0(t) = - \sum \gamma_{j,|m_j|}(t) \rho_0(t), \quad (5.6)$$

$$\dot{\rho}_{j,|m_j|}(t) = \gamma_{j,|m_j|}(t) \rho_0(t), \quad (5.7)$$

we get the hole dynamics attributable to the tunneling mechanism. In above, ρ_0 is the population of the neutral ground state, $\rho_{j,|m_j|}$ is the population of a specific spin-orbit valence-hole state, and $\gamma_{j,|m_j|}$ is the tunneling rate into each ionization channel with implicit time dependence via the field amplitude [56, 223].

5.3.1 Electronic correlation and long-range Coulomb effects on the SFI dynamics

Before starting to compare the two types of TDCIS hole dynamics, let us first make a detour. In this subsection, we study only the TDCIS full wave-packet dynamics for the two spin-orbit ionic states $5p_{3/2}^{-1}$ and $5p_{1/2}^{-1}$ of Xe^+ . We inspect how multielectron interaction and long-range

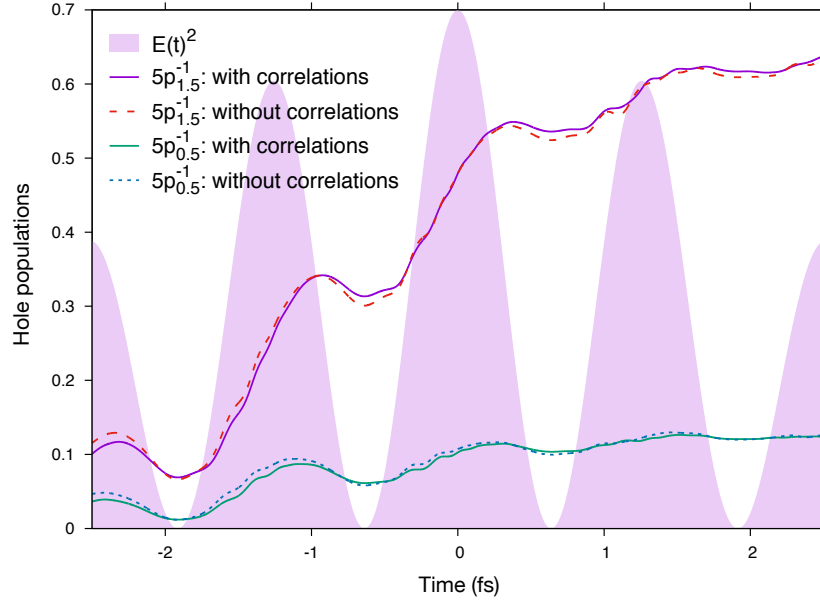


Figure 5.9. Comparison of the subcycle SFI dynamics for $5p_{3/2}^{-1}$ and $5p_{1/2}^{-1}$ of Xe^+ with (solid lines) and without (dashed and dotted lines) electronic correlation effects during a few-cycle SFI process. The results are based on the TDCIS full wave-packet calculations. The NIR pulse has a peak intensity of $2.8 \times 10^{14} \text{ W/cm}^2$, and its instantaneous intensity is indicated by the shaded area. The figure is adopted from Ref. [60]. Copyright ©2017 Nature Publishing Group.

Coulomb interaction—the two kinds of interactions that SFI theories frequently make strong approximations of—would affect the subcycle SFI hole dynamics. The purpose of this diversion is twofold. By evaluating the effects of these interactions in our numerical experiments, we aim to (1) get some hint on the nature of the half-cycle oscillations and (2) simplify the underlying physical picture and streamline our simulation and analysis procedures.

Effects of many-electron interaction on the subcycle SFI dynamics. The TDCIS theory embodies essential electronic correlation effects beyond the MF level. Hence, by turning on and off two-body electron-ion interaction, namely the interchannel-coupling part of the residual Coulomb interaction \hat{H}_1 (see 2.2.3), we are able to assess the importance of many-electron effects during the SFI process.

Figure 5.9 illustrates the subcycle SFI dynamics for $5p_{3/2}^{-1}$ and $5p_{1/2}^{-1}$ with and without multi-electron correlations in the TDCIS full wave-packet calculations. The few-cycle NIR pulse has a peak intensity of $I = 2.8 \times 10^{14} \text{ W/cm}^2$. The hole dynamics with and without two-body

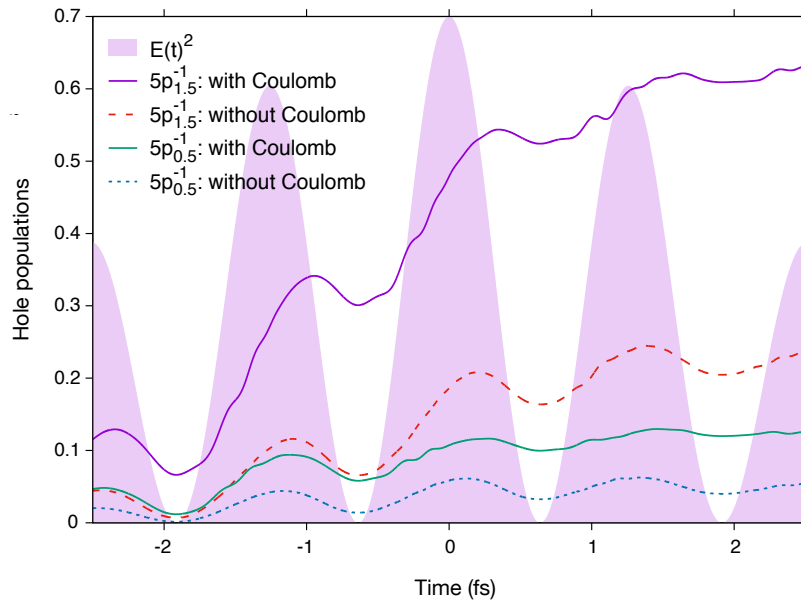


Figure 5.10. Comparison of the subcycle SFI dynamics for $5p_{3/2}^{-1}$ and $5p_{1/2}^{-1}$ of Xe^+ with (solid lines) and without (dashed and dotted lines) long-range Coulomb effects during a few-cycle SFI process. The results are based on the TDCIS full wave-packet calculations. For the results labeled “with Coulomb”, the excited electron sees an effective long-range potential produced by Xe^+ with a Coulomb tail; for those labeled “without Coulomb”, the electron sees a short-range potential generated by neutral Xe. The NIR pulse has a peak intensity of $2.8 \times 10^{14} \text{ W/cm}^2$, and its instantaneous intensity is indicated by the shaded area. The figure is adopted from Ref. [60]. Copyright ©2017 Nature Publishing Group.

interchannel couplings almost lie on top of each other. This demonstrates that many-electron interaction plays only a minor role in the overall subcycle SFI process and, hence, in explaining the half-cycle oscillations and the relative phase delays observed in Sec. 5.2. The results shown here confirm the validity of using a simplified one-particle–potential picture for the theoretical treatment of SFI, as done in the widely used single–active-electron approximation (SAE) (see Sec. 1.3). This aspect allows us to perform reduced one-channel calculations for the analyses that will be presented in the subsequent subsections.

Effects of long-range Coulomb interaction on the subcycle SFI dynamics. The above analysis shows that we can employ an effective one-particle potential to depict the electron–ion interaction during the SFI process. A question immediately follows as to how critical it is for the effective potential to have the correct long-range Coulomb behavior. In the

correlation-free SFI dynamics shown in Fig. 5.9, the excited electron experiences the intra-channel potential produced by Xe^+ with $-1/r$ dependence at large electron-ion distances. Here, we carry out another simulation, where one-body electron-ion interaction, namely the intrachannel-coupling part of \hat{H}_1 , is further switched off such that the residual Coulomb interaction is totally discarded. In this case, the photoelectron simply senses the short-range HF potential generated by neutral Xe (see 2.2.3).

Figure 5.10 shows the subcycle SFI dynamics for $5p_{3/2}^{-1}$ and $5p_{1/2}^{-1}$ with and without the effects of long-range Coulomb interaction in the TDCIS full wave-packet calculations. The NIR intensity is the same as used before, i.e., $I = 2.8 \times 10^{14} \text{ W/cm}^2$. Evidently, the long-range Coulomb tail has a vital impact on the subcycle SFI dynamics. In the absence of this correction, the final ion yields as well as the ionization steps for both of the channels are significantly underestimated. Also, the positions of the oscillation maxima in the population dynamics are highly sensitive to the long-range interaction. Without it, the absolute phase delays between the local maxima of the hole dynamics and those of the instantaneous NIR intensity are much smaller for each channel. As a result, the relative phase delays between the oscillation maxima of the two channels cannot be predicted accurately. These findings exemplify that neglecting the long-range ionic attraction for the photoelectron, as done in the popular SFA approximation (see Sec. 5.1), is inadequate for the quantitative description of the subcycle SFI dynamics, in accordance with the results of previous numerical studies [114, 224].^f Finally, we note that, with the short-range potential, the amplitudes of the half-cycle oscillations are much weaker before the appearance of noticeable tunnel ionization steps (i.e., at $t \lesssim -2 \text{ fs}$), an observation to be kept in mind.

5.3.2 Decomposition of the SFI dynamics

It is known that both quasistatic [88, 196, 216] and nonquasistatic [217] SFI theories predict ionization dynamics that grow monotonically in time. Hence, neither of these analytical models can account for the half-cycle oscillations observed in Sec. 5.2. In this subsection, in order to uncover the physical origin of the oscillations, we compare the strong-field dynamics of Xe predicted by the TDCIS full wave-packet model to those given by the (TD)CIS pure tunneling-rate model. Since we have shown that electronic correlations (see Fig. 5.9) and

^fIn the standard form of SFA [88, 197, 198], the ionized electron moves under the sole influence of the intense laser field. It is assumed that the light-matter interaction is so strong such that the electron-ion Coulomb interaction can be neglected. In a more technical language, the state of the photoelectron is described in terms of the Volkov wave functions, the eigenstates of an electron freely quivering in a radiation field [23].

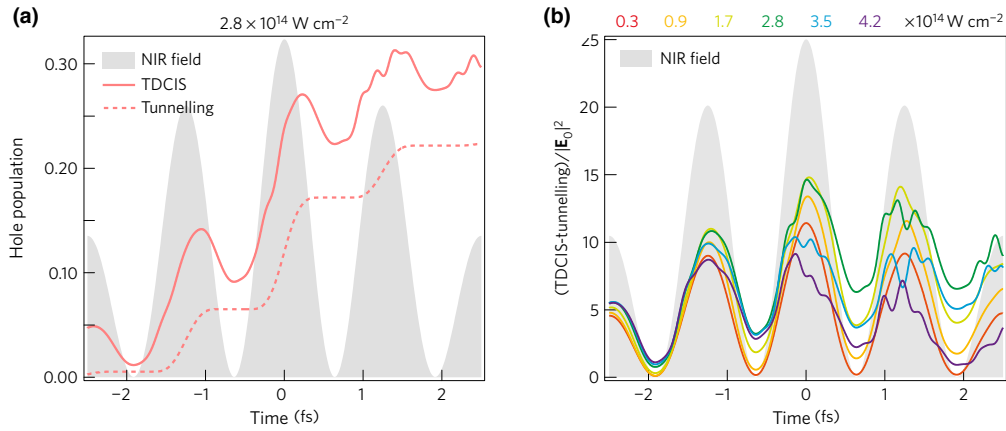


Figure 5.11. Decomposition of the strong-field ion dynamics. **(a)** To investigate the origin of the oscillatory feature, tunneling calculations are performed for the $5p_{1/2}^{-1}$ valence-hole state of Xe^+ at an NIR intensity of $2.8 \times 10^{14} \text{ W/cm}^2$. The results labeled “TDCIS” are based on TDCIS full wave-packet calculations; those labeled “Tunneling” are based on (TD)CIS tunneling-rate calculations. **(b)** Population differences between the full wave-packet calculations and the purely tunneling calculations for various intensities normalized by the corresponding peak intensity $|\mathbf{E}_0|^2$. The linear dependence of the discrepancy between the full and tunneling dynamics substantiates the interpretation of the oscillatory feature as a signature of reversible bound electron motion due to NIR-induced polarization of the Xe ground state. In each panel, the profile of the instantaneous NIR intensity is indicated by a shaded area. The figure is adopted from Ref. [60]. Copyright ©2017 Nature Publishing Group.

multichannel effects (see Fig. 5.6) do not have much influence on the temporal structures of the hole dynamics, we conduct one-channel calculations and focus only on the behavior of the $5p_{1/2}$ channel here.

Deconstruction of the SFI dynamics and origin of the half-cycle oscillations. Figure 5.11(a) presents the comparison of the $5p_{1/2}^{-1}$ population dynamics in the pure tunneling model and that in the full wave-packet model calculated at an NIR intensity of $2.8 \times 10^{14} \text{ W/cm}^2$. We observe that the half-cycle oscillations lie above the pure tunneling dynamics. Thus, they represent “overshoots” or temporary enhancement of the ion population, rather than “dips” or transient suppression of the ion population.

Following this observation, we use the tunneling dynamics as a baseline and subtract it from the full wave-packet dynamics. The resulting curve, which denotes the hole dynamics beyond the description of the tunneling model, is plotted in Fig. 5.11(b) (green line): it

exhibits $2\omega_L$ oscillations in coarse synchrony with the square of the electric field $|\mathbf{E}(t)|^2$, revealing another type of strong-field-driven electronic behavior that is uniquely distinct from tunnel ionization. By repeating the above analysis at various NIR intensities, the oscillations after the removal of each tunneling background are found to roughly follow the instantaneous profile of $|\mathbf{E}(t)|^2$ and scale nearly linearly with the peak field intensity $|\mathbf{E}_0|^2$ [see Fig. 5.11(b)]. This indicates that these oscillations originate from laser-induced polarization of the neutral ground state, which temporarily mixes the field-free ground state with excited configurations and creates a transient valence hole.

At this point, the results of our combined experimental-theoretical study shown in Sec. 5.2 and the numerical analyses shown in this section demonstrate that subcycle ion dynamics in the presence of a strong optical field are decided by an interplay of two different hole-generation mechanisms. On the one hand, tunnel ionization leads to typical ionization steps in the hole dynamics, which represent irreversible and monotonic growth of the ion population as the excited electron leaves to the asymptotes. On the other hand, ground-state polarization leads to half-cycle oscillations in the hole dynamics, which represent reversible and periodic formation of the ion population as the excited electron remains bound to the ion. Although the second pathway, polarization, is well understood in the weak-field $\gamma \gg 1$ regime, its significance had been frequently overlooked in the strong-field $\gamma \ll 1$ regime, both experimentally [199–201] and theoretically [88, 196, 216, 217]. This is perhaps because a majority of studies in the past are centered around photoelectron spectroscopy, a technique that focuses exclusively on the asymptotic photoelectron production and is not directly sensitive to the localized electronic behavior close to the ion. By contrast, both the asymptotic and localized electronic dynamics are manifested unambiguously by investigating the photoion production, as enabled by the ATAS technique.

Long-range Coulomb effects revisited. Having established the coexistence of the two strong-field-driven ion-formation pathways, let us now revisit the effects of long-range Coulomb interaction on the subcycle ion dynamics and explain the observations of our numerical results in Fig. 5.10.

The Coulomb effects enhance both the tunneling and the polarization hole-generation mechanisms. A long-range potential has a lower and thinner potential barrier when it is tilted by a laser field, and thus gives rise to a higher tunneling rate. This explains why the increments of the ionization steps and the final ion yields are larger in the presence of the Coulomb-tail correction in Fig. 5.10. Additionally, since a long-range potential accom-

modates more bound states than a short-range potential, its existence boosts the ground-state polarization process. This justifies why the amplitudes of the half-cycle oscillations are greater with the long-range ionic attraction before the tunneling mechanism starts to kick in (i.e., at $t \lesssim -2$ fs) in Fig. 5.10. The interpretations of these numerical observations reiterate the importance of using a long-range potential for the theoretical treatment of strongly driven subcycle electron dynamics [114].

Explanation of the phase delays. Here, we discuss how the relative contribution of the two ion-production pathways varies as a function of the NIR intensity, which can help to understand the phase delays observed in Sec. 5.2. Polarization mechanism starts to produce transient ions already at a very weak intensity and scales up linearly with the intensity. In comparison, tunnel ionization needs to overcome a minimum intensity onset to come into play and then scales up nonlinearly with the intensity. Therefore, there is a crossover of the dominating hole-creation mechanism from ground-state polarization to tunnel ionization. This explains why the half-cycle oscillations in the reconstructed hole dynamics in Fig. 5.7 appear more pronounced in the lower intensity case.

The two mechanisms and the crossover help to rationalize the appearance of the phase delays and their dependence on the ionization channel and the NIR intensity shown in Fig. 5.7. Given that the hole population dynamics are composed of two different types of signals, a trivial contribution dubbed apparent delay can already be identified as the phase delay that is created when the oscillatory signals due to polarization are added to two different tunneling backgrounds. As the ionization threshold for the $5p_{3/2}$ channel is lower [117], this channel has a higher tunneling rate (thus a steeper increment of ionization steps) and a more sensitive dependence on the intensity [23, 217]. Consequently, the oscillation maxima for $5p_{3/2}^{-1}$ are delayed in reference to those for $5p_{1/2}^{-1}$ and the relative delay becomes larger as the intensity goes up.

It is worthy to point out that the above explanation for the phase delays may be too naïve upon a closer examination. As can be seen from Fig. 5.11(b), even after removing the tunneling background, the reversible hole dynamics and $|\mathbf{E}(t)|^2$ are not entirely synchronized, meaning that there may be a phase delay of a nontrivial origin. There are several possible mechanisms that can contribute to this nontrivial delay. For example, this delay may arise as a result of the competition of the two hole-creation pathways, strong-field–induced nonlinear polarization [225], or, more interestingly, a slight breakdown of diabaticity in the strong-field regime [56].

Discussion of recent time-resolved experiments. With a better understanding of the sub-cycle features observed in SFI, it is now possible to place previous experiments concerning time-resolved strong-field ionization and excitation in the context of this work. In the pioneering experiment of Uiberacker et al. [89], tunnel ionization was observed by detecting the Ne^{2+} yield from shake-up states of Ne^+ that were populated by an attosecond XUV pulse. The authors observed “dips” in the tunnel ionization steps that, however, were smaller than the error bars and could not be explained within their tunneling model. We believe that the occurrence of the dips in Ref. [89] arises from a similar mechanism that accounts for the overshoots reported in our study: it is launched by strong NIR polarization of the Ne ground state, which indirectly modulates the shake-up process through electronic correlations. Later experiments observed strong-field excitation dynamics in solid-state fused silica and silicon. In fused silica, Schultze et al. [226] observed reversible $2\omega_L$ oscillations in synchrony with the electric field strength (in the absence of SFI); however, in silicon, Schultze et al. [227] found distinct excitation steps with a periodicity of $2\omega_L$. The qualitative difference between the two experiments can be attributed to the bandgap of the material. Fused silica has a rather large bandgap of 9 eV, resulting in a higher Keldysh parameter than the 3.2 eV bandgap of silicon. As a result, driving fused silica with a strong electric field gave rise to a polarization response between conduction and valence bands, while subjecting silicon to the same electric field strengths results in irreversible charge carrier excitation.

5.3.3 Visualization of wave-packet motion in the weak- and strong-field limits

We have identified two mechanisms—ground-state polarization and tunnel ionization—that govern subcycle ion-production processes separately in the weak- and strong-field limits and undergo a crossover in the intermediate region. The two mechanisms manifest themselves as two opposite types of temporal structures—the reversible and the irreversible—in the hole population dynamics. Since the existence of an ion is intimately connected with the existence of a deformed charge-density distribution away from the field-free ground-state distribution, in this subsection, we study the motion of the induced charge density of a Xe wave packet in the two limits in order to gain more intuition on the two mechanisms and their mixing process.

Calculation of wave-packet densities within TDCIS. Here, we present and explain the expression for calculating induced charge densities within the TDCIS full wave-packet scheme.

For an N -electron wave function $|\Psi(t)\rangle$, the charge density $n(\mathbf{x}, t)$ at a position \mathbf{x} and a time t is the one-particle density with a minus sign [109]

$$n(\mathbf{x}, t) = -\langle \Psi(t) | \hat{\Psi}^\dagger(\mathbf{x}) \hat{\Psi}(\mathbf{x}) | \Psi(t) \rangle. \quad (5.8)$$

In above, $\hat{\Psi}(\mathbf{x}) = \sum_p \hat{c}_p \phi_p(\mathbf{x})$ and $\hat{\Psi}^\dagger(\mathbf{x}) = \sum_p \hat{c}_p^\dagger \phi_p^\dagger(\mathbf{x})$ are the electron field operators in the second-quantization formalism; the index p in each summation represents any possible spinor orbital $\phi_p(\mathbf{x})$, and the electron annihilation and creation operators \hat{c}_p and \hat{c}_p^\dagger have already been introduced in 2.2.1. Plugging the TDCIS wave-function ansatz

$$|\Psi(t)\rangle = \alpha_0(t) |\Phi_0\rangle + \sum_{i,a} \alpha_i^a(t) |\Phi_i^a\rangle$$

given in Eq. (2.29) into Eq. (5.8), we immediately get

$$n(\mathbf{x}, t) = n_0(\mathbf{x}) + n_{\text{elec}}(\mathbf{x}, t) + n_{\text{hole}}(\mathbf{x}, t) + n_{\text{elec-hole}}(\mathbf{x}, t) \quad (5.9)$$

by partitioning the total charge density into the following four terms. The first term represents the ground-state charge density

$$n_0(\mathbf{x}) = -\sum_k \phi_k^\dagger(\mathbf{x}) \phi_k(\mathbf{x}), \quad (5.10)$$

which is always negative and sums over the densities of all the occupied orbitals $\phi_k(\mathbf{x})$ in the field-free MF ground state. The second term denotes the electron charge density

$$n_{\text{elec}}(\mathbf{x}, t) = -\sum_{i,a,b} \alpha_i^{a*}(t) \alpha_i^b(t) \phi_a^\dagger(\mathbf{x}) \phi_b(\mathbf{x}), \quad (5.11)$$

which is always negative; $\phi_a^\dagger(\mathbf{x})$ and $\phi_b(\mathbf{x})$ are virtual orbitals. The third term symbolizes the hole charge density

$$n_{\text{hole}}(\mathbf{x}, t) = +\sum_{i,j,a} \alpha_i^{a*}(t) \alpha_j^a(t) \phi_i^\dagger(\mathbf{x}) \phi_j(\mathbf{x}) \quad (5.12)$$

which is always positive; $\phi_i(\mathbf{x})$ and $\phi_j(\mathbf{x})$ are active occupied orbitals. Finally, the fourth term stands for the charge density due to the interference between the electron and the hole

$$n_{\text{elec-hole}}(\mathbf{x}, t) = -2 \text{Re} \left\{ \sum_{i,a} \alpha_i^{a*}(t) \alpha_0(t) \phi_a^\dagger(\mathbf{x}) \phi_i(\mathbf{x}) \right\}, \quad (5.13)$$

which can be both positive or negative and makes notable contribution to $n(\mathbf{x}, t)$ only when the excited electron stays close to the hole, i.e., when their orbitals overlap significantly.

Since $n_0(\mathbf{x})$ is a constant over time, it only serves as a static background density and can be subtracted from $n(\mathbf{x}, t)$. All the interesting dynamical information of the wave packet is then contained in the induced charge density in reference to the ground-state distribution given by

$$\Delta n(\mathbf{x}, t) = n_{\text{elec}}(\mathbf{x}, t) + n_{\text{hole}}(\mathbf{x}, t) + n_{\text{elec-hole}}(\mathbf{x}, t). \quad (5.14)$$

Snapshots of wave-packet motion in the two limits. Now we present the computed snapshots of the induced charge density of a Xe wave packet within a half NIR cycle in the weak- and strong-field limits. For better visualization, spin-orbit splitting is neglected here so that the angular part of a hole orbital is just a single spherical harmonic [57]. Without loss of generality, the calculations are performed for the $5p_{m_l=0}$ channel. The densities are plotted in 2D due to the cylindrical symmetry of the Hamiltonian about the polarization z axis.

The wave-packet movie in the weak-field limit during a half cycle $T/2$ is illustrated in Fig. 5.12(a); the NIR intensity used is 0.3×10^{14} W/cm². Here, the hole-creation mechanism is governed by reversible ground-state dressing, which temporarily separates the positive and negative charges within the Xe atom. As the electron always stays nearby the hole, the induced charge density is mainly decided by the interference term $n_{\text{elec-hole}}(\mathbf{x}, t)$ and displays compact and rich patterns. Close to the end of the half-cycle, the displaced electron cloud flows back and fills in the hole, such that the hole population is restored to zero. In this reversible process, the hole population oscillates in phase with the instantaneous NIR intensity profile.

The wave-packet motion in the strong-field limit is shown in Fig. 5.12(b); the NIR intensity used is 3.2×10^{14} W/cm². In this case, the hole-production mechanism is ruled by irreversible tunnel ionization. Starting from $-T/8$, the electric field quickly pulls the electron cloud away from the hole. The tunnel-ionized electron rapidly spreads out and disappears from the numerical box, leaving a permanent hole behind. As a result, features in the induced charge density primarily stem from the individual contributions of $n_{\text{elec}}(\mathbf{x}, t)$ and $n_{\text{hole}}(\mathbf{x}, t)$, while $n_{\text{elec-hole}}(\mathbf{x}, t)$ does not play much of a role. In this irreversible process, the hole population increases stepwise and monotonically during the NIR subcycle.

In between the two limits, the hole-generation process is a mixture of the reversible and irreversible mechanisms. In this intermediate region lie most of the strong-field experiments. Naturally, the hole population exhibits both oscillatory and monotonic characters.

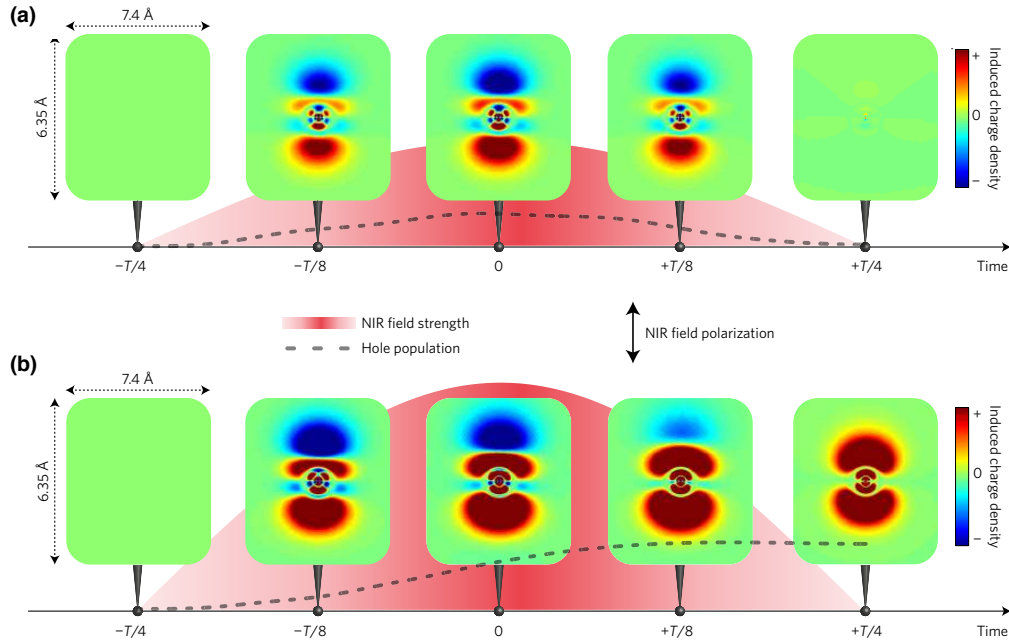


Figure 5.12. Time evolution of the light-induced charge density in Xe by an NIR laser field in different intensity limits. The induced charge density is defined as the charge density of the driven wave packet minus the charge density of the field-free ground state and is here depicted at five different instances in time within a half laser cycle $T/2$. **(a)** Evolution in the weak-field limit, at an intensity of $0.3 \times 10^{14} \text{ W/cm}^2$. Here, ground-state polarization leads to temporary separation of the positive and negative charges. After the half cycle, the electron cloud flows back and fills in the hole; i.e., this hole-creation pathway is reversible. **(b)** Evolution in the strong-field limit, at an intensity of $3.2 \times 10^{14} \text{ W/cm}^2$. Here, tunnel ionization results in irrecoverable loss of the negative charge. After the half cycle, part of the electron cloud disappears from the atom and permanently leaves a hole behind; i.e., this hole-creation pathway is irreversible. In each panel, the instantaneous NIR field strength is indicated by a shaded area, and the hole population dynamics is indicated by a dashed line. The figure is adopted from Ref. [60]. Copyright ©2017 Nature Publishing Group.

5.4 Summary

The key messages of this chapter are summarized as follows:

- ◇ In our joint experiment-theory study, we concretely corroborate the quantitative capability of the ATAS technique to follow key features of the real-time SFI dynamics of Xe in an ion-state- and subcycle-resolved manner (Sec. 5.2).
- ◇ We rigorously establish a new feature of ultrafast electron dynamics in strong optical fields: the observed hole population dynamics exhibit prominent half-cycle oscillations in addition to typical tunnel ionization steps. We show that the oscillatory feature is not a result of multichannel coherence, but an innate character of strong-field-driven electron dynamics.
- ◇ Our study shows that there is a small discrepancy between effective and instantaneous SFI dynamics. This stems from an intrinsic limitation of ATAS when it is used to probe electron dynamics during SFI, i.e., when the pump and the probe are required to overlap temporally. By assessing both the strength of the ATAS technique as well as the caveat coming along with it, our work lays a quantitative foundation for interpreting the information content of ATAS measurements.
- ◇ With the help of theory, we identify the origin of the observed half-cycle oscillations in the strongly driven ion dynamics of Xe. By comparing TDCIS full wave-packet calculations and (TD)CIS tunneling-rate CAP-based calculations, we show that these overshoots in the ion population dynamics come from strong-field-induced polarization of the field-free electronic ground state (Sec. 5.3).
- ◇ Our results reveal the existence of a dichotomy of electron motion in intense laser fields: one motion corresponds to an irreversible, monotonic ion build-up process resulting from tunnel ionization; another one is associated with a reversible, periodic electron displacement due to transient ground-state polarization. Although the latter aspect, polarization, is well understood in weak-field scenarios, its significance had been overlooked in the strong-field context.
- ◇ The coexistence of the two ion-creation pathways in intense laser fields, undetected in previous ultrafast experiments on lighter atoms, comes to sight not only as a consequence of the high polarizability of Xe, but also as a result of the unprecedented

sensitivity of ATAS to a less studied physical system—the photoions. The effects of ultrafast strong-field–induced polarization, or more generally, the effects of strong-field–dressed bound electronic structure, are expected to play an even more important part in comprehending the time-resolved electronic response of complex systems in the non-perturbative light-matter regime.

Chapter 6

Conclusion and outlook

From Chapter 1 to Chapter 5, we have come a long way. Now it is the time to step back and take a view of the big picture. In this chapter, we bring the present doctoral dissertation to a closure.

Section 6.1 summarizes the content of this thesis. Section 6.2 provides perspectives for future studies.

6.1 Conclusion

In the microcosm of electrons, dynamics typically unfolds on a time scale between 10 as and 10 fs. No mechanical or electronic device operates on such a time scale. Hence, the only way to probe into this otherwise intangible world is by watching how it interacts with light. Tremendous progress in generating coherent electromagnetic radiation, e.g., based on FELs, femtosecond lasers, HHG sources, has given us a wide range of new tools to communicate with electrons. This has brought about a new era of photoionization research, where electron motion can be triggered by highly nonlinear processes and can be measured with exquisite timing precision.

In this doctoral dissertation, we have explored a subset of the photoionization dynamics that can be observed or initiated using ultrashort and ultraintense light pulses. We have concentrated on the photoionization processes that involve electronic resonances decaying or evolving on the attosecond time scale. As a first step towards assessing the behavior of complex electronic systems, we have selected isolated Xe atoms as a prototype system, whose behavior can be analyzed relatively easily from both theoretical and experimental sides.

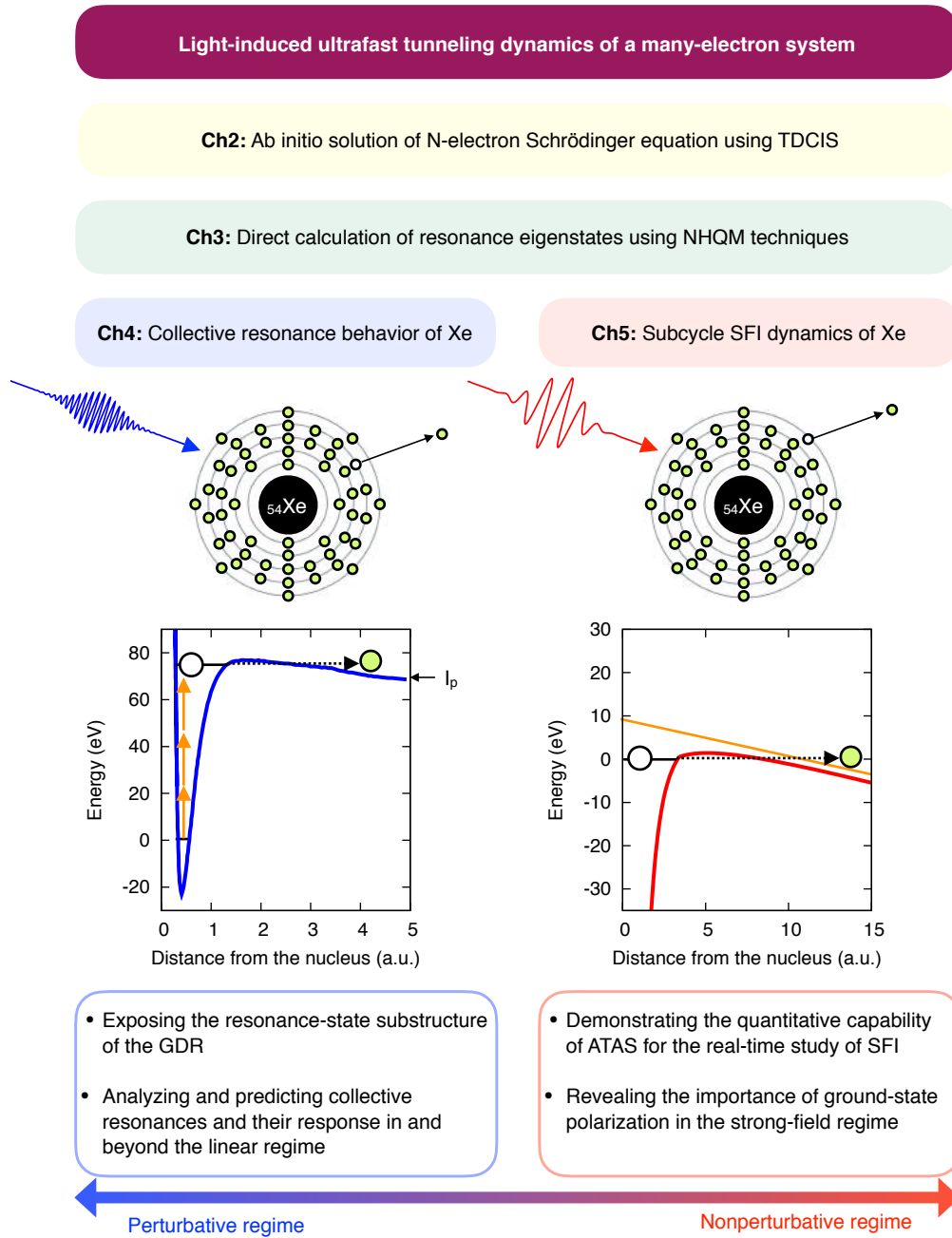


Figure 6.1. Review of the structure and the contributions of this doctoral dissertation.

In order to simulate photoionization dynamics of a multielectron atom over a broad light-pulse parameter space, the N -electron TDSE has been solved from first principles using the TDCIS approach (Chapter 2). TDCIS not only provides reasonable flexibility and quantitative capability, but also captures essential many-electron aspects of photoionization, namely the multichannel and interchannel-coupling effects. TDCIS, which I have co-developed during my doctoral study, currently stands as the most efficient wave-function–based electronic structure theory that can tackle the nonperturbative dynamics of Xe.

Resonance dynamics is included in the time evolution of a wave packet formed by a collection of continuum states. A simpler description of such dynamics has been introduced, where a resonance state can be uniquely identified as one single discrete, bound-state–like eigenstate of a transformed Hamiltonian (Chapter 3). Full information on the Siegert states can be obtained by numerical diagonalization of an instantaneous Hamiltonian subjected to SES or CAP. The combination of SES with TDCIS for the study of collective electronic resonances marks the first application of its kind.

Two applications of ultrafast resonance dynamics of Xe have been analyzed in the two regimes of light-matter coupling, respectively. Both the wave-packet and the eigenstate approaches have been used to gain complementary insights into the resonance processes. In below, we review the major contributions of each application.

Collective resonance behavior of Xe. In the first application, we have studied the collective resonance behavior during XUV, inner-shell, perturbative photoionization of Xe (Chapter 4).

- *Section 4.2:* While our understanding of the $4d$ GDR had so far been inferred from linear-response studies, we raised the unique question as to what are the fundamental resonance eigenmodes embedded in the spectral region of the GDR. By analyzing the GDR wave packet in the combined time-frequency domain, it came as a surprise that the GDR is in fact consist of two overlapping, short-lived dipole resonance states. This result was verified again by the SES calculation, which further attested the collective nature of both the sub-resonances. The first complete characterization of the GDR substructure was achieved and is consistent with the knee-type structure seen in the XUV two-photon ATI experiment [53].
- *Section 4.3:* We continued using the SES method to investigate all types of collective resonance states in the $4d$ subshell, and then connected them to their spectroscopic fingerprints. In the GDR case, we showed that linear spectroscopy—the main tool for

our understanding of the GDR over the past half-century—reveals only partial information of the GDR substructure due to quantum interferences. Going beyond the dipole modes, we proposed a two-color–three-photon scheme to probe the relatively long-lived, collective octupole resonance uncovered in our work. By beginning with the resonance-state electronic structure, our methodology offers a fresh way to interpret spectroscopic data of collective excitations in and beyond the linear regime.

Subcycle strong-field-ionization dynamics of Xe. In the second application, we have studied the subcycle dynamics of SFI during NIR, valence-shell, nonperturbative photoionization of Xe (Chapter 5).

- *Section 5.2:* In our joint experiment-theory collaboration, we utilized ATAS to follow ultrafast ion-formation dynamics in two spin-orbit-split $5p$ levels of Xe and extended previous studies to heavy elements. Our results demonstrated that ATAS is able to map out important features of SFI even when the pump and probe pulses overlap in time. One of such features was a prominent oscillatory behavior of the ion populations, which could not be explained by existing analytical SFI models. We pointed out that interpretation of detailed features of the reconstructed SFI dynamics shall be made with caution, because ATAS measures a nonlocal signal over the Auger lifetime of the core-hole-excited states.
- *Section 5.3:* After validating the TDCIS theory, it was employed to identify the mechanism behind the oscillating behavior of the SFI dynamics. By comparing the full wavepacket to the CAP-based tunneling-rate calculations, we illustrated that the oscillations represent transient enhancement of the ion populations and arise from NIR-induced polarization of the neutral ground state. Thanks to the high polarizability of Xe, we established the dichotomy of electron motion in strong optical fields: on the one hand, tunnel ionization monotonically builds up ions as time goes by; on the other hand, polarization periodically distorts the electron cloud without ionizing it. These two opposite types of motion signify two facets of the light-induced resonance state, both of which need to be included for a comprehensive picture of SFI.

6.2 Outlook

The results presented in this doctoral dissertation have raised a bevy of research questions and potential applications. In the following, we discuss: (1) what are the questions remaining to be studied for our benchmark system, atomic Xe, and (2) how to apply the insights extracted from Xe to a more general class of physical systems.

Collective resonance behavior: from Xe to complex systems. Here we list a few research opportunities derived from the results of Chapter 4.

- *Time-resolved measurement of the GDR substructure of Xe:* The two sub-resonances underlying the GDR are characterized by a different excitation energy as well as a different lifetime (see Table 4.3). This means that the two resonances release an electron into the continuum in a slightly different amount of time, differed by 15 as. Such a photoemission time delay is currently an active research topic in attosecond science and can be measured using the technique of attosecond streaking [19] or the technique of attosecond interferometry [87]. With a recently achieved experimental timing capability down to a few attoseconds [228], it may be well expected that experiments of this kind will offer a truly unique opportunity to decode the GDR substructure in real time. The pump-probe spectrogram of either technique [19, 87] can be directly computed using the existing XCID package [49].
- *Resonance-state approach for the collective excitations in complex systems:* The resonance-state approach enables one not only to fully characterize dipole to multipole collective resonances by diagonalizing once a nonhermitian Hamiltonian, but also to dissect absorption spectra in a state-by-state manner using the resulting eigenstates. A natural way to broaden the utility of this approach is to employ it to study the collective resonances of heavy elements close to Xe in the periodic table, such as I, Cs, La. Linear spectroscopic studies have already shown that atomic GDR exists in these elements and is preserved when these atoms aggregate into molecules and clusters [85, 86]. The collective behavior of these species has an added complexity in comparison to that of Xe: they are generally open-shell systems and display strong ground-state correlation. The theoretical treatment of such atoms requires an extension of XCID, whose current applicability is limited to closed-shell atoms, using, e.g., the extended CIS method [229]. Furthermore, in order to evaluate generalized cross sections as can be measured at

FEL facilities, formulas in analogy to Eq. (4.20) need to be derived by performing non-hermitian perturbation analysis to higher order. By doing so, one has a comprehensive theoretical toolkit to investigate the electronic response of open-shell systems under the intertwined effects of collectivity and nonlinearity, a nearly uncharted territory [84].

Subcycle strong-field-ionization dynamics: from Xe to complex systems. Now we list some research opportunities derived from the results of Chapter 5.

- *Nonlinear polarization and nonadiabatic effects during the SFI dynamics of Xe:* When Xe is driven by an intense femtosecond laser, both the reversible pathway (polarization) and the irreversible pathway (tunnel ionization) contribute to the electron dynamics. Several aspects of this result remain to be explored and can be analyzed immediately with the available XCID package.

First, one may ask what is the role of nonlinear polarization during SFI. Although we have shown that linear polarization is the main mechanism that causes the oscillations in the hole-population dynamics, it is very likely that, at such a high field strength, the effects of higher order polarization will come into play. In fact, such nonlinear response of bound electrons to intense optical fields has been observed using attosecond metrology for Kr, at a pump intensity lower than what we used in our study [225].

Second, one may ask if there are multiple tunneling states participating in the SFI dynamics. In our CAP-based tunneling-rate calculations, only one single field-induced tunneling resonance state, i.e., the field-dressed ground state, was included. Because the field strength changes dramatically inside each laser half-cycle, it is feasible that the system fails to adjust to the instantaneous time-dependent tilted potential: the state of the system becomes a superposition of several field-dressed eigenstates and its behavior is no longer purely adiabatic. Indeed, a previous TDCIS study has shown that, already for a two-electron He atom, the nonadiabatic effects kick in starting at a rather small value of the Keldysh parameter $\gamma \approx 0.17$ [56], i.e., in a supposedly deep adiabatic regime.

Clearly, the fundamental picture of SFI of multielectron atoms warrants further refinement.

- *Subcycle SFI dynamics of complex systems:* Tunnel ionization and polarization manifest two different aspects of the light-induced resonance state. This indicates that a new ingredient needs to be integrated into the standard picture of SFI [see Fig. 1.3(b)]:

it is no longer sufficient to speak only of the tilted potential; the quantum state from which the electron tunnels out matters. This points to a future research direction for the modeling of SFI in complex systems, where the investigation of nonperturbative light-matter interaction is just beginning and relies heavily on basic theoretical models to gauge the underlying processes. We propose that polarization, or dressing, of the ground state shall be included in the modeling of subcycle SFI dynamics; this aspect can be particularly important for systems such as extended molecules with dense energy spacing or dielectrics with a small band gap.

Whereas the field-free ground state is still widely used in standard SFI models, there are a few works already going towards this direction. For instance, Ref. [230] shows that the peak ionization rates of N_2 and O_2 as a function of the molecular orientation angle critically depend on if a dressed initial state is used in the molecular SFA. As another example, Ref. [231] finds that the quantitative description of the HHG spectra of CH_3F and CH_3Br requires one to use field-modified orbitals in the tunneling-rate calculations. Based on the evidence from Refs. [230, 231] as well as from our study, it is anticipated that the use of dressed electronic structure will substantially improve the predictive power of SFI models and, in this way, will help us to gain deeper insights into the strongly driven behavior of complex systems.

In summary, this thesis has allowed to reveal several new and unexpected aspects of a fundamental phenomenon, namely photoionization. There is no doubt that, in the near future, with further development in experimental capabilities and theoretical understanding, even more unforeseen and exciting surprises are waiting for us.

Bibliography

- [1] A. Einstein, *Ann. Phys.* **322**, 132 (1905).
- [2] H. Hall, *Rev. Mod. Phys.* **8**, 358 (1936).
- [3] U. Fano and J. W. Cooper, *Rev. Mod. Phys.* **40**, 441 (1968).
- [4] J. J. Rehr and R. C. Albers, *Rev. Mod. Phys.* **72**, 621 (2000).
- [5] L. Young, K. Ueda, M. Gühr, *et al.*, *J. Phys. B: At. Mol. Opt. Phys.* **51**, 032003 (2018).
- [6] T. Brabec and F. Krausz, *Rev. Mod. Phys.* **72**, 545 (2000).
- [7] J. Ullrich, A. Rudenko, and R. Moshhammer, *Annu. Rev. Phys. Chem.* **63**, 635 (2012).
- [8] M. Protopapas, C. H. Keitel, and P. L. Knight, *Rep. Prog. Phys.* **60**, 389 (1997).
- [9] E. A. Seddon, J. A. Clarke, D. J. Dunning, *et al.*, *Rep. Prog. Phys.* **80**, 115901 (2017).
- [10] L. Young, E. P. Kanter, B. Krässig, *et al.*, *Nature* **466**, 56 (2010).
- [11] B. Rudek, S.-K. Son, L. Foucar, *et al.*, *Nat. Photonics* **6**, 858 (2012).
- [12] K. Toyota, S.-K. Son, and R. Santra, *Phys. Rev. A* **95**, 043412 (2017).
- [13] T. Popmintchev, M.-C. Chen, D. Popmintchev, *et al.*, *Science* **336**, 1287 (2012).
- [14] T. Gaumnitz, A. Jain, Y. Pertot, M. Huppert, I. Jordan, F. Ardana-Lamas, and H. J. Wörner, *Opt. Express* **25**, 27506 (2017).
- [15] F. Krausz and M. Ivanov, *Rev. Mod. Phys.* **81**, 163 (2009).
- [16] F. Calegari, G. Sansone, S. Stagira, C. Vozzi, and M. Nisoli, *J. Phys. B: At. Mol. Opt. Phys.* **49**, 062001 (2016).
- [17] F. Calegari, D. Ayuso, A. Trabattoni, *et al.*, *Science* **346**, 336 (2014).
- [18] L. Cederbaum and J. Zobeley, *Chem. Phys. Lett.* **307**, 205 (1999).
- [19] M. Schultze, M. Fiess, N. Karpowicz, *et al.*, *Science* **328**, 1658 (2010).
- [20] A. L. Cavalieri, N. Müller, T. Uphues, *et al.*, *Nature* **449**, 1029 (2007).
- [21] I. Jordan, M. Huppert, S. Pabst, A. S. Kheifets, D. Baykusheva, and H. J. Wörner, *Phys. Rev. A* **95**, 013404 (2017).
- [22] V. S. Popov, *Phys-Usp* **47**, 855 (2004).
- [23] S. V. Popruzhenko, *J. Phys. B: At. Mol. Opt. Phys.* **47**, 204001 (2014).
- [24] P. Lambropoulos, *Adv. At. Mol. Phys.* **12**, 87 (1976).
- [25] G. G. Paulus, W. Nicklich, H. Xu, P. Lambropoulos, and H. Walther, *Phys. Rev. Lett.* **72**, 2851 (1994).

- [26] P. B. Corkum and F. Krausz, *Nat. Phys.* **3**, 381 (2007).
- [27] F. A. Ilkov, J. E. Decker, and S. L. Chin, *J. Phys. B: At. Mol. Opt. Phys.* **25**, 4005 (1992).
- [28] B. H. Bransden and C. J. Joachain, *Physics of Atoms and Molecules*, 2nd ed. (Prentice Hall, 2003).
- [29] A. F. Starace, in *Encycl. Phys.*, Vol. 31, edited by W. Mehlhorn (Springer-Verlag, Berlin, 1982) p. 1.
- [30] K. L. Ishikawa and T. Sato, *IEEE J. Sel. Top. Quantum Electron* **21**, 8700916 (2015).
- [31] D. Hochstuhl, C. M. Hinz, and M. Bonitz, *Eur. Phys. J. Spec. Top.* **223**, 177 (2014).
- [32] A. L’Huillier and G. Wendin, *Phys. Rev. A* **36**, 4747 (1987).
- [33] G. Wendin, *Phys. Lett. A* **37**, 445 (1971).
- [34] M. Y. Amusia, *Atomic Photoeffect* (Plenum, New York, 1990).
- [35] H. P. Kelly, in *Photoionization and Other Probes of Many-Electron Interactions*, edited by F. J. Wuilleumier (Plenum Press, 1975) p. 83.
- [36] G. Wendin, L. Jönsson, and A. L’Huillier, *J. Opt. Soc. Am. B* **4**, 833 (1987).
- [37] S.-K. Son and R. Santra, *Phys. Rev. A* **85**, 063415 (2012).
- [38] K. C. Kulander, *Phys. Rev. A* **36**, 2726 (1987).
- [39] H. G. Muller, *Phys. Rev. A* **60**, 1341 (1999).
- [40] J. Higuete, H. Ruf, N. Thiré, *et al.*, *Phys. Rev. A* **83**, 053401 (2011).
- [41] S. Pabst, *Eur. Phys. J. Spec. Top.* **221**, 1 (2013).
- [42] S. Pabst and R. Santra, in *Comput. Strong-f. Quantum Dyn. Intense Light. Interact.*, edited by D. Bauer (De Gruyter, 2017) Chap. 6.
- [43] N. Rohringer, A. Gordon, and R. Santra, *Phys. Rev. A* **74**, 043420 (2006).
- [44] L. Greenman, P. J. Ho, S. Pabst, E. Kamarchik, D. A. Mazziotti, and R. Santra, *Phys. Rev. A* **82**, 023406 (2010).
- [45] S. Pabst, L. Greenman, D. A. Mazziotti, and R. Santra, *Phys. Rev. A* **85**, 023411 (2012).
- [46] S. Pabst, A. Sytcheva, A. Moulet, A. Wirth, E. Goulielmakis, and R. Santra, *Phys. Rev. A* **86**, 063411 (2012).
- [47] A. Karamatskou, S. Pabst, Y.-J. Chen, and R. Santra, *Phys. Rev. A* **89**, 033415 (2014).
- [48] S. Pabst, A. Sytcheva, O. Geffert, and R. Santra, *Phys. Rev. A* **94**, 033421 (2016).
- [49] S. Pabst, L. Greenman, A. Karamatskou, Y.-J. Chen, A. Sytcheva, O. Geffert, and R. Santra, *XCID—The Configuration-Interaction Dynamics Package*, 1220th ed. (CFEL, DESY, Hamburg, 2014).
- [50] S. Pabst, L. Greenman, P. J. Ho, D. A. Mazziotti, and R. Santra, *Phys. Rev. Lett.* **106**, 053003 (2011).
- [51] D. Krebs, S. Pabst, and R. Santra, *Am. J. Phys.* **82**, 113 (2014).
- [52] Y.-J. Chen, S. Pabst, A. Karamatskou, and R. Santra, *Phys. Rev. A* **91**, 032503 (2015).
- [53] T. Mazza, A. Karamatskou, M. Ilchen, *et al.*, *Nat. Commun.* **6**, 6799 (2015).
- [54] M. Tilley, A. Karamatskou, and R. Santra, *J. Phys. B: At. Mol. Opt. Phys.* **48**, 124001 (2015).
- [55] A. Karamatskou and R. Santra, *Phys. Rev. A* **95**, 013415 (2016).

- [56] A. Karamatskou, S. Pabst, and R. Santra, *Phys. Rev. A* **87**, 043422 (2013).
- [57] S. Pabst and R. Santra, *J. Phys. B: At. Mol. Opt. Phys.* **47**, 124026 (2014).
- [58] S. Pabst and R. Santra, *Phys. Rev. Lett.* **111**, 233005 (2013).
- [59] D. Faccialà, S. Pabst, B. D. Bruner, *et al.*, *Phys. Rev. Lett.* **117**, 093902 (2016).
- [60] M. Sabbar, H. Timmers, Y.-J. Chen, *et al.*, *Nat. Phys.* **13**, 472 (2017).
- [61] T. Sato and K. L. Ishikawa, *Phys. Rev. A* **88**, 023402 (2013).
- [62] T. Sato and K. L. Ishikawa, *Phys. Rev. A* **91**, 023417 (2015).
- [63] H. Miyagi and L. B. Madsen, *Phys. Rev. A* **87**, 062511 (2013).
- [64] M. S. Pindzola, D. C. Griffin, and C. Bottcher, *Phys. Rev. Lett.* **66**, 2305 (1991).
- [65] P. G. Burke and V. M. Burke, *J. Phys. B: At. Mol. Opt. Phys.* **30**, L383 (1997).
- [66] X. Guan, O. Zatsarinny, K. Bartschat, B. I. Schneider, J. Feist, and C. J. Noble, *Phys. Rev. A* **76**, 053411 (2007).
- [67] L. Torlina, M. Ivanov, Z. B. Walters, and O. Smirnova, *Phys. Rev. A* **86**, 043409 (2012).
- [68] G. H. Booth, A. Grüneis, G. Kresse, and A. Alavi, *Nature* **493**, 365 (2012).
- [69] C. Lévêque and L. B. Madsen, *New J. Phys.* **19**, 043007 (2017).
- [70] X.-M. Tong and S.-I. Chu, *Phys. Rev. A* **57**, 452 (1998).
- [71] F. Lackner, I. Březinová, T. Sato, K. L. Ishikawa, and J. Burgdörfer, *Phys. Rev. A* **91**, 023412 (2015).
- [72] M. Brics and D. Bauer, *Phys. Rev. A* **88**, 052514 (2013).
- [73] Y. Orimo, T. Sato, A. Scrinzi, and K. L. Ishikawa, *Phys. Rev. A* **97**, 023423 (2018).
- [74] H. Miyagi and L. B. Madsen, *Phys. Rev. A* **89**, 063416 (2014).
- [75] M. A. Lysaght, P. G. Burke, and H. W. van der Hart, *Phys. Rev. Lett.* **101**, 253001 (2008).
- [76] A. D. Shiner, B. E. Schmidt, C. Trallero-Herrero, *et al.*, *Nat. Phys.* **7**, 464 (2011).
- [77] N. Moiseyev, *Non-Hermitian Quantum Mechanics* (Cambridge University Press, New York, 2011).
- [78] S. Klaiman and I. Gilary, in *Advances in Quantum Chemistry*, Vol. 63 (Academic Press, 2012) p. 1.
- [79] J. R. Taylor, *Scattering Theory: The Quantum Theory of Nonrelativistic Collisions* (John Wiley & Sons, 1972).
- [80] R. Santra and L. S. Cederbaum, *Phys. Rep.* **368**, 1 (2002).
- [81] S.-K. Son, R. Thiele, Z. Jurek, B. Ziaja, and R. Santra, *Phys. Rev. X* **4**, 031004 (2014).
- [82] D. L. Ederer, *Phys. Rev. Lett.* **13**, 760 (1964).
- [83] A. P. Lukirskii, I. A. Brytov, and T. M. Zimkina, *Opt. Spectrosc.* **17**, 234 (1964).
- [84] M. Y. Amusia and J. P. Connerade, *Rep. Prog. Phys.* **63**, 41 (2000).
- [85] C. Bréchnac and J. P. Connerade, *J. Phys. B: At. Mol. Opt. Phys.* **27**, 3795 (1994).

- [86] J. P. Connerade, J. M. Esteve, and R. C. Karnatak, eds., *Giant Resonances in Atoms, Molecules, and Solids* (Plenum, New York, 1987).
- [87] M. Huppert, I. Jordan, D. Baykusheva, A. von Conta, and H. J. Wörner, *Phys. Rev. Lett.* **117**, 093001 (2016).
- [88] L. V. Keldysh, *Sov. Phys. JETP* **20**, 1307 (1965).
- [89] M. Uiberacker, T. Uphues, M. Schultze, et al., *Nature* **446**, 627 (2007).
- [90] A. Wirth, M. T. Hassan, I. Grguraš, et al., *Science* **334**, 195 (2011).
- [91] Y.-J. Chen, S. Pabst, and R. Santra, *J. Phys. Commun.* **2**, 045024 (2018).
- [92] D. P. Craig and T. Thirunamachandran, *Molecular Quantum Electrodynamics: An Introduction to Radiation-Molecule Interactions* (Dover, 1998).
- [93] J. J. Sakurai, *Modern Quantum Mechanics*, rev. ed., edited by S. F. Tuan (Addison-Wesley, 1994).
- [94] M. Maggiore, *A Modern Introduction to Quantum Field Theory* (Oxford University Press, 2005).
- [95] A. Das, *Lectures on Quantum Field Theory* (World Scientific, 2008).
- [96] J. D. Jackson, *Classical Electrodynamics*, 3rd ed. (Wiley, 1999).
- [97] F. S. Levin, *An Introduction to Quantum Theory* (Cambridge University Press, 2002).
- [98] J. D. Jackson, *Am. J. Phys.* **70**, 917 (2002).
- [99] C. Cohen-Tannoudji, J. Dupont-Roc, and G. Grynberg, *Atom-Photon Interactions: Basic Processes and Applications* (Wiley, 1992).
- [100] M. O. Scully and M. S. Zubairy, *Quantum Optics* (Cambridge University Press, 1997).
- [101] P. J. Mohr, D. B. Newell, and B. N. Taylor, *The 2014 CODATA Recommended Values of the Fundamental Physical Constants*, 7th ed. (National Institute of Standards and Technology, 2016).
- [102] J. E. Sansonetti, W. C. Martin, and S. L. Young, *Handbook of Basic Atomic Spectroscopic Data*, 1st ed. (National Institute of Standards and Technology, 2013).
- [103] M. B. Gaarde, J. L. Tate, and K. J. Schafer, *J. Phys. B: At. Mol. Opt. Phys.* **41**, 132001 (2008).
- [104] A. C. Thompson, ed., *X-Ray Data Booklet*, 3rd ed. (Lawrence Berkeley National Laboratory, 2009).
- [105] H. R. Reiss, in *Lect. Ultrafast Intense Laser Sci.*, edited by K. Yamanouchi (Springer, 2010) Chap. 2.
- [106] A. D. Bandrauk, F. Fillion-Gourdeau, and E. Lorin, *J. Phys. B: At. Mol. Opt. Phys.* **46**, 153001 (2013).
- [107] D. Krebs, *Atomic Photoabsorption Spectroscopy Using Time-Dependent Configuration-Interaction Singles*, Bachelor Thesis, University of Hamburg (2013).
- [108] R. E. Bellman, *Adaptive Control Processes: A Guided Tour* (Princeton University Press, 1961).
- [109] A. Szabo and N. S. Ostlund, *Modern Quantum Chemistry: Introduction to Advanced Electronic Structure Theory* (Dover, Mineola, New York, 1996).
- [110] I. N. Levine, *Quantum Chemistry*, 7th ed. (Pearson, 2014).
- [111] F. H. M. Faisal, *Theory of Multiphoton Processes* (Plenum Press, 1987).

- [112] T. Sato, T. Teramura, and K. Ishikawa, *Appl. Sci.* **8**, 433 (2018).
- [113] K. Blum, *Density Matrix Theory and Applications*, Springer Series on Atomic, Optical, and Plasma Physics, Vol. 64 (Springer Berlin Heidelberg, Berlin, Heidelberg, 2012).
- [114] O. Smirnova, M. Spanner, and M. Ivanov, *J. Phys. B: At. Mol. Opt. Phys.* **39**, S307 (2006).
- [115] T. F. Gallagher, *Rydberg Atoms* (Cambridge University Press, 2005).
- [116] W. Y. Liang, *Phys. Edu.* **5**, 226 (1970).
- [117] A. Kramida, Y. Ralchenko, J. Reader, and NIST ASD Team, *NIST Atomic Spectra Database*, 5th ed. (National Institute of Standards and Technology, Gaithersburg, Maryland, 2014).
- [118] M. Jurvansuu, A. Kivimäki, and S. Aksela, *Phys. Rev. A* **64**, 012502 (2001).
- [119] N. Rosen and P. M. Morse, *Phys. Rev.* **42**, 210 (1932).
- [120] D. J. Tannor, *Introduction to Quantum Mechanics: A Time-Dependent Perspective* (University Science Books, Sausalito, Calif, 2007).
- [121] N. Moiseyev, *Phys. Rep.* **302**, 212 (1998).
- [122] A. J. F. Siegert, *Phys. Rev.* **56**, 750 (1939).
- [123] N. Hatano, K. Sasada, H. Nakamura, and T. Petrosky, *Prog. Theor. Phys.* **119**, 187 (2008).
- [124] R. Santra, J. M. Shainline, and C. H. Greene, *Phys. Rev. A* **71**, 032703 (2005).
- [125] O. I. Tolstikhin, V. N. Ostrovsky, and H. Nakamura, *Phys. Rev. Lett.* **79**, 2026 (1997).
- [126] W. P. Reinhardt, *Annu. Rev. Phys. Chem.* **33**, 223 (1982).
- [127] Y. K. Ho, *Phys. Rep.* **99**, 1 (1983).
- [128] J. N. L. Connor and A. D. Smith, *J. Chem. Phys.* **78**, 6161 (1983).
- [129] E. Balslev and J. M. Combes, *Commun. Math. Phys.* **22**, 280 (1971).
- [130] B. Simon, *Commun. Math. Phys.* **27**, 1 (1972).
- [131] B. Simon, *Phys. Lett. A* **71**, 211 (1979).
- [132] N. Rom, E. Engdahl, and N. Moiseyev, *J. Chem. Phys.* **93**, 3413 (1990).
- [133] N. Moiseyev, *J. Phys. B: At. Mol. Opt. Phys.* **31**, 1431 (1998).
- [134] H. O. Karlsson, *J. Chem. Phys.* **109**, 9366 (1998).
- [135] J. Muga, J. Palao, B. Navarro, and I. Egusquiza, *Phys. Rep.* **395**, 357 (2004).
- [136] U. V. Riss and H.-D. Meyer, *J. Phys. B: At. Mol. Opt. Phys.* **26**, 4503 (1993).
- [137] U. V. Riss and H.-D. Meyer, *J. Phys. B: At. Mol. Opt. Phys.* **28**, 1475 (1995).
- [138] U. V. Riss and H.-D. Meyer, *J. Chem. Phys.* **105**, 1409 (1996).
- [139] U. V. Riss and H.-D. Meyer, *J. Phys. B: At. Mol. Opt. Phys.* **31**, 2279 (1998).
- [140] W. H. Press, S. A. Teukolsky, W. T. Vetterling, and B. P. Flannery, *Numerical Recipes: The Art of Scientific Computing*, 3rd ed. (Cambridge University Press, Cambridge, UK ; New York, 2007).
- [141] J. W. Cooper, *Phys. Rev. Lett.* **13**, 762 (1964).
- [142] F. Bloch, *Z. Phys.* **81**, 363 (1933).
- [143] R. Latter, *Phys. Rev.* **99**, 510 (1955).
- [144] M. Y. Amusia, N. A. Cherepkov, and S. I. Shetel, *Phys. Lett. A* **24**, 541 (1967).

- [145] W. Brandt, L. Eder, and S. Lundqvist, *J. Quant. Spectrosc. Radiat. Transf.* **7**, 185 (1967).
- [146] A. F. Starace, *Phys. Rev. A* **2**, 118 (1970).
- [147] G. Wendin, *J. Phys. B: At. Mol. Opt. Phys.* **6**, 42 (1973).
- [148] A. Zangwill and P. Soven, *Phys. Rev. A* **21**, 1561 (1980).
- [149] Z. Altun, M. Kutzner, and H. P. Kelly, *Phys. Rev. A* **37**, 4671 (1988).
- [150] R. Haensel, G. Keitel, P. Schreiber, and C. Kunz, *Phys. Rev.* **188**, 1375 (1969).
- [151] J. B. West and J. Morton, *Data Nucl. Data Tables* **22**, 103 (1978).
- [152] U. Becker, D. Szostak, H. G. Kerkhoff, *et al.*, *Phys. Rev. A* **39**, 3902 (1989).
- [153] J. A. R. Samson and W. C. Stolte, *J. Electron Spectros. Relat. Phenom.* **123**, 265 (2002).
- [154] M. Richter, M. Y. Amusia, S. V. Bobashev, *et al.*, *Phys. Rev. Lett.* **102**, 163002 (2009).
- [155] V. Richardson, J. T. Costello, D. Cubaynes, *et al.*, *Phys. Rev. Lett.* **105**, 013001 (2010).
- [156] N. Gerken, S. Klumpp, A. A. Sorokin, *et al.*, *Phys. Rev. Lett.* **112**, 213002 (2014).
- [157] M. Y. Amusia, *Atomic Photoeffect* (Plenum Press, New York, 1990).
- [158] Ž. Crljen and G. Wendin, *Phys. Rev. A* **35**, 1571 (1987).
- [159] S. Lundqvist and G. Mukhopadhyay, *Phys. Scr.* **21**, 503 (1980).
- [160] M. Y. Amusia, N. A. Cherepkov, R. K. Janev, and D. Živanović, *J. Phys. B: At. Mol. Opt. Phys.* **7**, 1435 (1974).
- [161] B. Povh, K. Rith, C. Scholz, F. Zetsche, and W. Rodejohann, *Particles and Nuclei: An Introduction to the Physical Concepts* (Springer-Verlag, Berlin, 1995).
- [162] B. Boashash, ed., *Time-Frequency Signal Analysis and Processing: A Comprehensive Reference* (Elsevier, Oxford, 2003).
- [163] P. Antoine, B. Piraux, and A. Maquet, *Phys. Rev. A* **51**, R1750 (1995).
- [164] R. Schinke, *Photodissociation Dynamics* (Cambridge University Press, New York, 1993).
- [165] S. K. Gray, *J. Chem. Phys.* **96**, 6543 (1992).
- [166] A. Isele, C. Meier, V. Engel, N. Fahrner, and C. Schlier, *J. Chem. Phys.* **101**, 5919 (1994).
- [167] N. Moiseyev and C. Corcoran, *Phys. Rev. A* **20**, 814 (1979).
- [168] A. Scrinzi and B. Piraux, *Phys. Rev. A* **58**, 1310 (1998).
- [169] D. A. Telnov and S.-I. Chu, *Phys. Rev. A* **66**, 043417 (2002).
- [170] C. W. McCurdy, D. A. Horner, and T. N. Rescigno, *Phys. Rev. A* **65**, 042714 (2002).
- [171] X.-B. Bian and A. D. Bandrauk, *Phys. Rev. A* **83**, 023414 (2011).
- [172] P. Lablanquie, S. Sheinerman, F. Penent, *et al.*, *J. Phys. B: At. Mol. Opt. Phys.* **35**, 3265 (2002).
- [173] X.-M. Tong and S.-I. Chu, *Phys. Rev. A* **61**, 021802(R) (2000).
- [174] D. Gabor, *J. Inst. Electr. Eng.* **93**, 429 (1946).
- [175] C. C. Chirilă, I. Dreissigacker, E. V. van der Zwan, and M. Lein, *Phys. Rev. A* **81**, 033412 (2010).

- [176] X. M. Tong and N. Toshima, *Phys. Rev. A* **81**, 063403 (2010).
- [177] J. L. Krause, K. J. Schafer, and K. C. Kulander, *Phys. Rev. A* **45**, 4998 (1992).
- [178] A. Kaldun, C. Ott, A. Blättermann, *et al.*, *Phys. Rev. Lett.* **112**, 103001 (2014).
- [179] E. P. Power, A. M. March, F. Catoire, E. Sistrunk, K. Krushelnick, P. Agostini, and L. F. DiMauro, *Nat. Photonics* **4**, 352 (2010).
- [180] D. C. Sorensen, R. B. Lehoucq, C. Yang, and K. Maschhoff, *ARPACK—ARnoldi PACKage*, 2nd ed. (Rice University, Houston, Texas, 1996).
- [181] O. E. Alon and N. Moiseyev, *Phys. Rev. A* **46**, 3807 (1992).
- [182] F. Herman and S. Skillman, *Atomic Structure Calculations* (Prentice-Hall, Englewood Cliffs, New Jersey, 1963).
- [183] P. A. Christiansen, Y. S. Lee, and K. S. Pitzer, *J. Chem. Phys.* **71**, 4445 (1979).
- [184] L.-W. Pi and A. F. Starace, *Phys. Rev. A* **82**, 053414 (2010).
- [185] K. C. Kulander, *Phys. Rev. A* **38**, 778 (1988).
- [186] K. J. Schafer, B. Yang, L. F. DiMauro, and K. C. Kulander, *Phys. Rev. Lett.* **70**, 1599 (1993).
- [187] N. H. March, W. H. Young, and S. Sampanthar, *The Many-Body Problem in Quantum Mechanics* (Dover, Mineola, New York, 1995).
- [188] H. A. Bethe and E. E. Salpeter, *Quantum Mechanics of One- and Two-Electron Atoms*, dover ed. (Dover, 2008).
- [189] N. A. Cherepkov and S. K. Semenov, *J. Phys. B: At. Mol. Opt. Phys.* **34**, L495 (2001).
- [190] L.-W. Pi and A. F. Starace, *Phys. Rev. A* **90**, 023403 (2014).
- [191] J. Feldhaus, *J. Phys. B: At. Mol. Opt. Phys.* **43**, 194002 (2010).
- [192] E. Allaria, C. Callegari, D. Cocco, W. M. Fawley, M. Kiskinova, C. Masciovecchio, and F. Parmigiani, *New J. Phys.* **12**, 075002 (2010).
- [193] T. Sekikawa, A. Kosuge, T. Kanai, and S. Watanabe, *Nature* **432**, 605 (2004).
- [194] C. Buth and R. Santra, *Phys. Rev. A* **75**, 033412 (2007).
- [195] T. N. Rescigno and V. McKoy, *Phys. Rev. A* **12**, 522 (1975).
- [196] M. V. Ammosov, N. B. Delone, and V. P. Krainov, *Sov. Phys. JETP* **64**, 1191 (1986).
- [197] F. H. M. Faisal, *J. Phys. B: At. Mol. Opt. Phys.* **6**, L89 (1973).
- [198] H. R. Reiss, *Phys. Rev. A* **22**, 1786 (1980).
- [199] S. L. Chin, F. Yergeau, and P. Lavigne, *J. Phys. B: At. Mol. Opt. Phys.* **18**, L213 (1985).
- [200] S. Augst, D. D. Meyerhofer, D. Strickland, and S. L. Chint, *J. Opt. Soc. Am. B* **8**, 858 (1991).
- [201] P. Monot, T. Auguste, L. A. Lompré, G. Mainfray, and C. Manus, *J. Opt. Soc. Am. B* **9**, 1579 (1992).
- [202] M. Drescher, M. Hentschel, R. Kienberger, *et al.*, *Nature* **419**, 803 (2002).
- [203] K. Klünder, J. M. Dahlström, M. Gisselbrecht, *et al.*, *Phys. Rev. Lett.* **106**, 143002 (2011).
- [204] M. Sabbar, S. Heuser, R. Boge, *et al.*, *Phys. Rev. Lett.* **115**, 133001 (2015).
- [205] S. Neppl, R. Ernstorfer, E. M. Bothschafter, *et al.*, *Phys. Rev. Lett.* **109**, 087401 (2012).

- [206] E. Goulielmakis, Z.-H. Loh, A. Wirth, *et al.*, *Nature* **466**, 739 (2010).
- [207] H. Wang, M. Chini, S. Chen, *et al.*, *Phys. Rev. Lett.* **105**, 143002 (2010).
- [208] M. Holler, F. Schapper, L. Gallmann, and U. Keller, *Phys. Rev. Lett.* **106**, 123601 (2011).
- [209] C. Ott, A. Kaldun, P. Raith, *et al.*, *Science* **340**, 716 (2013).
- [210] S. R. Leone, C. W. McCurdy, J. Burgdörfer, *et al.*, *Nat. Photonics* **8**, 162 (2014).
- [211] R. Santra, V. S. Yakovlev, T. Pfeifer, and Z.-H. Loh, *Phys. Rev. A* **83**, 033405 (2011).
- [212] W. T. Pollard and R. A. Mathies, *Annu. Rev. Phys. Chem.* **43**, 497 (1992).
- [213] R. Berera, R. van Grondelle, and J. T. M. Kennis, *Photosynth. Res.* **101**, 105 (2009).
- [214] M. V. Lebedev, O. V. Misochko, T. Dekorsy, and N. Georgiev, *Sov. Phys. JETP* **100**, 272 (2005).
- [215] H. Timmers, M. Sabbar, J. Hellwagner, Y. Kobayashi, D. M. Neumark, and S. R. Leone, *Optica* **3**, 707 (2016).
- [216] A. M. Perelomov, V. S. Popov, and M. V. Terent'ev, *Sov. Phys. JETP* **23**, 924 (1966).
- [217] G. L. Yudin and M. Y. Ivanov, *Phys. Rev. A* **64**, 013409 (2001).
- [218] M. B. Gaarde, C. Buth, J. L. Tate, and K. J. Schafer, *Phys. Rev. A* **83**, 013419 (2011).
- [219] S. Schippers, *J. Quant. Spectrosc. Radiat. Transf.* **219**, 33 (2018).
- [220] A. Dalgarno and A. E. Kingston, *Proc. R. Soc. Math. Phys. Eng. Sci.* **259**, 424 (1960).
- [221] P. W. Langhoff and M. Karplus, *J. Opt. Soc. Am.* **59**, 863 (1969).
- [222] T. Nubbemeyer, K. Gorling, A. Saenz, U. Eichmann, and W. Sandner, *Phys. Rev. Lett.* **101**, 233001 (2008).
- [223] R. Santra, R. W. Dunford, and L. Young, *Phys. Rev. A* **74**, 043403 (2006).
- [224] D. Dimitrovski and L. B. Madsen, *Phys. Rev. A* **78**, 043424 (2008).
- [225] M. T. Hassan, T. T. Luu, A. Moulet, *et al.*, *Nature* **530**, 66 (2016).
- [226] M. Schultze, E. M. Bothschafter, A. Sommer, *et al.*, *Nature* **493**, 75 (2013).
- [227] M. Schultze, K. Ramasesha, C. D. Pemmaraju, *et al.*, *Science* **346**, 1348 (2014).
- [228] M. Ossiander, F. Siegrist, V. Shirvanyan, *et al.*, *Nat. Phys.* **13**, 280 (2017).
- [229] D. Maurice and M. Head-Gordon, *J. Phys. Chem.* **100**, 6131 (1996).
- [230] D. B. Milošević, G. G. Paulus, D. Bauer, and W. Becker, *J. Phys. B: At. Mol. Opt. Phys.* **39**, R203 (2006).
- [231] P. M. Kraus, O. I. Tolstikhin, D. Baykusheva, *et al.*, *Nat. Commun.* **6**, 7039 (2015).

